LUND UNIVERSITY

Excited state dynamics in low-dimensional perovskite nanocrystals

Lin, Weihua

2022

Link to publication

Citation for published version (APA):
Lin, W. (2022). *Excited state dynamics in low-dimensional perovskite nanocrystals*. Chemical Physics, Lund University.

Total number of authors:
1

General rights
Unless other specific re-use rights are stated the following general rights apply:
Copyright and moral rights for the publications made accessible in the public portal are retained by the authors and/or other copyright owners and it is a condition of accessing publications that users recognise and abide by the legal requirements associated with these rights.
• Users may download and print one copy of any publication from the public portal for the purpose of private study or research.
• You may not further distribute the material or use it for any profit-making activity or commercial gain
• You may freely distribute the URL identifying the publication in the public portal

Read more about Creative commons licenses: https://creativecommons.org/licenses/

Take down policy
If you believe that this document breaches copyright please contact us providing details, and we will remove access to the work immediately and investigate your claim.

LUND UNIVERSITY

PO Box 117
221 00 Lund
+46 46-222 00 00

Excited state dynamics in low-dimensional perovskite nanocrystals

WEIHUA LIN
CHEMICAL PHYSICS | FACULTY OF SCIENCE | LUND UNIVERSITY

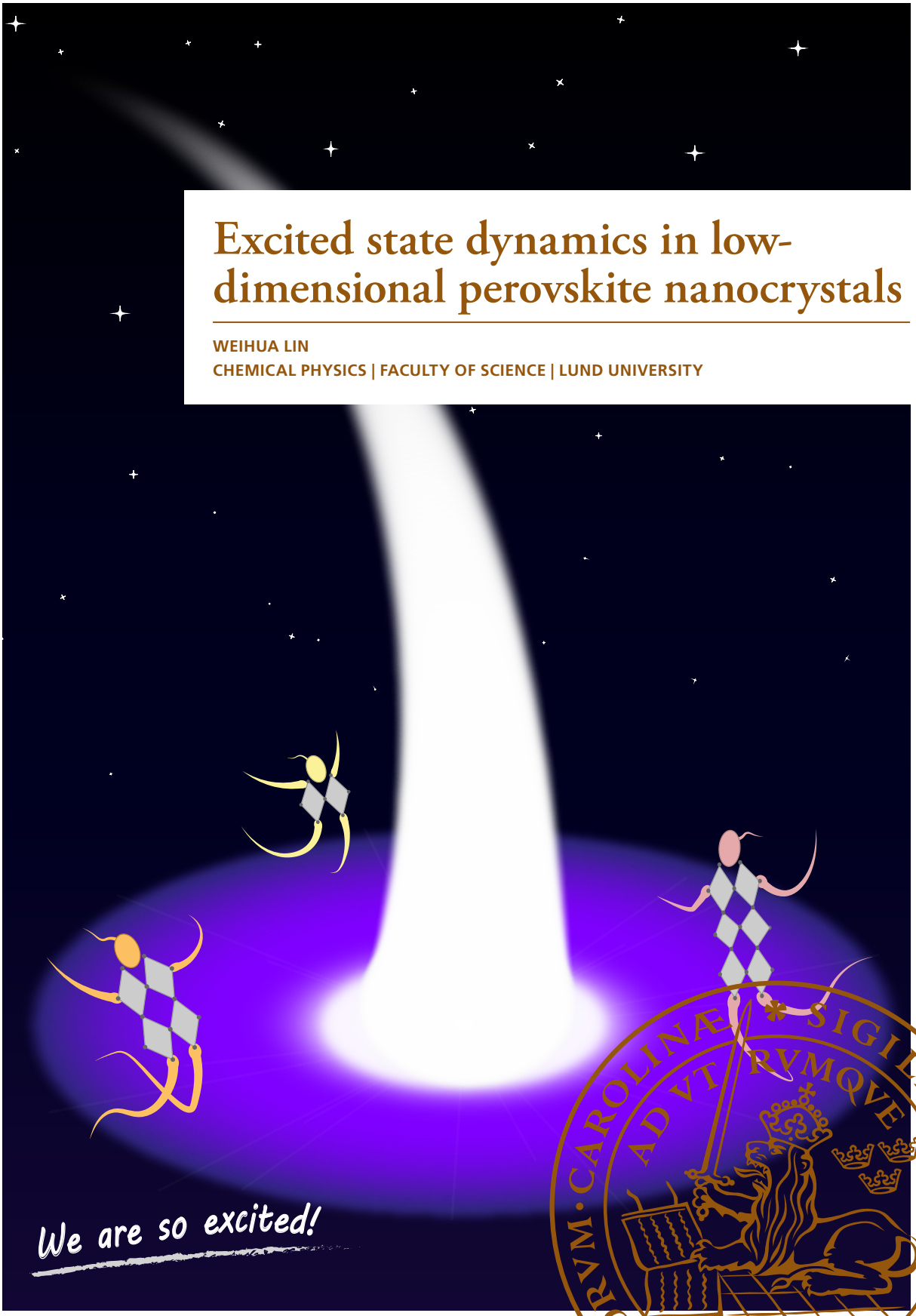

Excited state dynamics in low-dimensional perovskite nanocrystals

Excited state dynamics in low-dimensional perovskite nanocrystals

Weihua Lin

LUND
UNIVERSITY

DOCTORAL DISSERTATION
Doctoral dissertation for the degree of Doctor of Philosophy (Ph.D.) at the Faculty of Science at Lund University to be publicly defended on 29 November 2022 at 9.15 am. in Lecture Hall A of Kemicentrum, Department of Chemistry, Naturvetarvägen 16, 22362 Lund

Faculty opponent
Dr. Matthew C. Beard
National Renewable Energy Laboratory, United States

Organization LUND UNIVERSITY Division of Chemical Physics Department of Chemistry P. O. BOX 124, SE-22100 Lund, Sweden	**Document name** Doctoral Dissertation **Date of issue** 29th November 2022
Author(s) Weihua Lin	Sponsoring organization

Title and subtitle
Excited state dynamics in low-dimensional perovskite nanocrystals

Abstract

Two-dimensional (2D) perovskites have emerged as promising building blocks for optoelectronic applications. To fabricate high-performance devices, the relation between the material structures and their function in terms of excited state and charge carrier dynamics need to be well understood.

In this thesis, we investigate photophysics of 2D lead halide perovskite with different compositions to reveal the relation between lattice distortion and electronic properties. Firstly, we found that the threshold of the Goldschmidt tolerance factor is relaxed and thereby the range of possible composition for forming stable 2D perovskite is extended compared to 3D perovskite. In addition, lattice distortion is greater when containing large cations inside octahedral cages and the formed 2D perovskite has a larger band gap and higher trap state density. The link between lattice distortion and modification of electronic structure shows a potential approach to designing and developing high-performance PV materials. To further evaluate the influence of local lattice distortion on the electronic properties of 2D perovskite, we analyze fluorescence signals from different facets of samples with different spacers. We found that free carriers dominate in the in-plane facet (IF) while self-trapped excitons (STE) are the main emitters from the facet perpendicular to the 2D layer (PF). The strain accumulated along the 2D layers leads to enhanced carrier-phonon coupling and facilitates STE formation in PF, while in IF the separated flexible spacers contribute to releasing the strain accumulation. To directly characterize the electronic structure at different areas of a 2D perovskite single crystal, electrons emitted from Pb 5d and I 4d core levels are mapped at the edge and the bulk areas by using X-ray photoemission electron microscopy. The observed asymmetric shifts of the emission spectra of 2D perovskite indicate different degrees of lattice distortion at the edge and the bulk areas since the internal strain accumulation is released at the edge area. The different shift in Pb 5d core level emission between edge and bulk areas at 2D perovskites with different layer thickness confirms the contribution of spacers in releasing accumulated strain.

In addition, we investigated the ultrafast hot carrier (HC) relaxation dynamics in 2D perovskite single crystals by employing transient absorption (TA) spectroscopy and time-resolved two-photon photoemission (TR-2PPE) spectroscopy. With TR-2PPE, the distribution of hot electrons and their dynamics in the conduction band can be directly visualized. The different cooling rates of HC observed in the two techniques reflect the spatial sensitivity of relaxation dynamics across the 2D perovskite single crystal. We believe the comprehensive study on HC relaxation in 2D perovskite provides an effective approach to compare the potential of different materials in hot carrier solar cell (HCSC) applications and can extend thermoelectric applications based on 2D perovskites. We also investigated the influence of transition metal doping on electronic and phononic features of three-dimensional perovskite by studying the HC relaxation processes in Mn2+-doped and undoped CsPbI3 nanocrystals (NCs). The Mn2+ doping leads to the enlarged phononic gap between longitudinal optical (LO) – acoustic phonons, enhanced carrier-LO phonon coupling strength, and additional Mn orbitals within the original bands of the undoped sample, which are beneficial for establishing a hot quasi-equilibrium to recycle the energy from HC relaxation to reheat cold carriers. The results present a methodology to optimize HC dynamics by element doping and are meaningful for guiding the future development of HCSC applications.

Keywords Two-dimensional perovskite, Ultrafast spectroscopy, Single crystal, Nanocrystals, Hot carrier cooling

Classification system and/or index terms (if any)

Supplementary bibliographical information	**Language** English
ISSN and key title	**ISBN** Printed version: 978-91-7422-916-5 Digital version: 978-91-7422-917-2

Recipient's notes	**Number of pages** 74	Price
	Security classification	

I, the undersigned, being the copyright owner of the abstract of the above-mentioned dissertation, hereby grant to all reference sources permission to publish and disseminate the abstract of the above-mentioned dissertation.

Signature  Date 19th October 2022

Excited state dynamics in low-dimensional perovskite nanocrystals

Weihua Lin

LUND
UNIVERSITY

Coverphoto by Juanzi Shi and Weihua Lin

Copyright pp i-74 © Weihua Lin
Paper 1 © 2022 The Authors.

Paper 2 © 2020 American Chemical Society.

Paper 3 © 2021 The Authors, licensed under CC-BY 4.0. Published by American Chemical Society.

Paper 4 © 2022 The Authors, licensed under CC-BY 3.0. Published by Royal Society of Chemistry.

Paper 5 © 2022 The Authors.

Faculty of Science
Department of Chemistry

ISBN
978-91-7422-916-5 (Print)
978-91-7422-917-2 (Digital)

Printed in Sweden by Media-Tryck, Lund University
Lund 2022

Media-Tryck is a Nordic Swan Ecolabel certified provider of printed material. Read more about our environmental work at www.mediatryck.lu.se
MADE IN SWEDEN

Table of Contents

Abstract

Two-dimensional (2D) perovskites have emerged as promising building blocks for optoelectronic applications. To fabricate high-performance devices, the relation between the material structures and their function in terms of excited state and charge carrier dynamics need to be well understood.

In this thesis, we investigated photophysics of 2D lead halide perovskite with different compositions to reveal the relation between lattice distortion and electronic properties. Firstly, we found that the threshold of the Goldschmidt tolerance factor is relaxed and thereby the range of possible composition for forming stable 2D perovskite is extended compared to 3D perovskite. In addition, lattice distortion is greater when containing large cations inside octahedral cages and the formed 2D perovskite has a larger band gap and higher trap state density. The link between lattice distortion and modification of electronic structure shows a potential approach to designing and developing high-performance PV materials. To further evaluate the influence of local lattice distortion on the electronic properties of 2D perovskite, we analyzed fluorescence signals from different facets of samples with different spacers. We found that free carriers dominate in the in-plane facet (IF) while self-trapped excitons (STE) are the main emitters from the facet perpendicular to the 2D layer (PF). The strain accumulated along the 2D layers leads to enhanced carrier-phonon coupling and facilitates STE formation in PF, while in IF the separated flexible spacers contribute to releasing the strain accumulation. To directly characterize the electronic structure at different areas of a 2D perovskite single crystal, electrons emitted from Pb 5*d* and I 4*d* core levels are mapped at the edge and the bulk areas by using X-ray photoemission electron microscopy. The observed asymmetric shifts of the emission spectra of 2D perovskite indicate different degrees of lattice distortion at the edge and the bulk areas since the internal strain accumulation is released at the edge area. The different shift in Pb 5*d* core level emission between edge and bulk areas at 2D perovskites with different layer thickness confirms the contribution of spacers in releasing accumulated strain.

In addition, we investigated the ultrafast hot carrier (HC) relaxation dynamics in 2D perovskite single crystals by employing transient absorption (TA) spectroscopy and time-resolved two-photon photoemission (TR-2PPE) spectroscopy. With TR-2PPE, the distribution of hot electrons and their dynamics in the conduction band can be directly visualized. The different cooling rates of HC observed in the two techniques reflect the spatial sensitivity of relaxation dynamics across the 2D perovskite single

crystal. We believe the comprehensive study on HC relaxation in 2D perovskite provides an effective approach to compare the potential of different materials in hot carrier solar cell (HCSC) applications and can extend thermoelectric applications based on 2D perovskites. We also investigated the influence of transition metal doping on electronic and phononic features of three-dimensional perovskite by studying the HC relaxation processes in Mn^{2+}-doped and undoped $CsPbI_3$ nanocrystals (NCs). The Mn^{2+} doping leads to the enlarged phononic gap between longitudinal optical (LO) -acoustic phonons, enhanced carrier-LO phonon coupling strength, and additional Mn orbitals within the original bands of the undoped sample, which are beneficial for establishing a hot quasi-equilibrium to recycle the energy from HC relaxation to reheat cold carriers. The results present a methodology to optimize HC dynamics by element doping and are meaningful for guiding the future development of HCSC applications.

Popular Science Summary

For a more sustainable future, we need to switch to renewable energy sources, and utilizing solar energy is a promising and realistic long-term solution. The record for power conversion efficiency of solar cells has grown steadily in the past whilst with insufficient speed. Alternative solar technologies which can radically boost the device performance are desired in the field, with refreshing strategies for harvesting and storing solar energy. Many new solar technologies are proposed for exceeding the Shockley-Queisser limit, such as multiple exciton generation, singlet exciton fission and hot carrier (HC, carriers with excess energy) injection. The latter is closely related to hot carrier solar cells (HCSC), whose fundamental idea is to recycle the energy from HC relaxation before heat dissipation. A key to fabricating high-quality HCSC devices is finding a suitable absorber material.

Metal halide perovskite is an up-rising star in solar cell applications, and it has many outstanding photophysics properties but suffers from poor stability towards moisture. By inserting the long-chain organic spacing cations in the structure, the two-dimensional perovskite can be formed with significantly improved stability. The hydrophobic spacers work like an umbrella preventing the penetration of water into the octahedral layers (unit cell of 3D perovskite). In addition, because the spacers are soft and flexible, the octahedral cage in 2D perovskite can contain larger or smaller cations (A-site cation), in comparison to the limited available A-site cations with fixed sizes to be chosen when forming stable 3D perovskite. We found that the too large A-site cations result in greater lattice distortion and lead to changes in the electronic properties of the material. We also found that flexible spacers contribute to compensating the strain accumulated in rigid octahedral layers. We prepared bulky single crystals of 2D perovskite with different spacers to further 'zoom in' to the spacer effects. The millimeter-scale samples enable us to measure photoluminescence (PL) signals from the surface of each targeted facet. The strain is accumulated along the octahedral layer and released to the edge, so that the degree of lattice distortion at the edge and bulk areas are different which will result in different interactions with the lattice. By comparing PL spectra from the facets parallel and perpendicular to the octahedral layer, we conclude that different charge carrier species dominate in the two facets and confirm that local structural distortion can modify the electronic structure of 2D perovskite. We also vary the thickness of octahedral layers in one unit cell of 2D perovskite, where one unit cell equals *n*-layers of octahedral layer sandwiched by spacing cations. But this time instead of

measuring the photophysics of sample and speculating the change in electronic structure, we directly map the electrons emitted from core levels of Pb and I atoms at different areas of single crystals. The results indicate that when each 2D unit only contains one or two octahedral layers, the contribution of spacers in compensating the accumulated strain is more efficient than when in the case with three octahedral layers. In conclusion, we conduct a series of investigations on 2D perovskite with different compositions and at different areas at single crystals to reveal the relation between structural distortion and electronic structure in 2D perovskite.

In addition, we use ultrafast spectroscopies to investigate the HC relaxation in 2D perovskite. The two techniques we used are transient absorption (TA) spectroscopy and time-resolved two-photon photoemission (TR-2PPE) spectroscopy. TA spectroscopy has been widely used in investigating 3D perovskite, but the standard analysis method is sometimes problematic. TR-2PPE spectroscopy, on the other hand, has many experimental demands but can provide direct visualization of hot electron distribution. By comparing the results obtained from these two techniques, we can reveal the different HC cooling dynamics across the 2D perovskite single crystal, which is beneficial for thermoelectric applications based on 2D perovskites in the future. In addition, we also investigated the effect of transition metal doping on the properties of 3D perovskite nanocrystals (1 nm = 10^{-9} m). The difference in HC relaxation rates observed in doped and undoped samples points out what we can expect from doping methodology on the path towards HCSCs.

Acknowledgement

After recalling the experience of the past four years, I feel very grateful and lucky that I come to Lund for my Ph.D. study. Although sometimes it feels like time has been stolen by the epidemic, I still have seen a lot of beautiful scenery in my life journey.

The Chapter Lund of the journey started with the first meeting with my supervisor Tõnu Pullerits in Beijing, when I was still doing the master project at the University of Science and Technology Beijing (USTB). Thank you for meeting with me and providing the opportunity for me to study abroad. I vaguely remember that during the meeting I was not able to talk in English fluently, but I am quite certain that I enjoyed the scientific discussion and the chat with you. I still can picture that day - you were drawing on a whiteboard to explain the physics to me, while I was sitting on the sofa trying to figure out what words you just said. During the four years of upgrading – next to the whiteboard in your office, I have learned a great many things from you and keep realizing there is more I can learn from you than I imagined.

I arrived in Lund on a Friday morning in September 2018 and met my co-supervisor Kaibo Zheng during Division Fika. The kind and friendly chat with Kaibo made me almost forget the discomfort caused by jet lag and felt excited about exploring Europe. Thank you for providing extensive help in scientific projects and tips about living in Lund, as well as including me in many group activities in Denmark. The first meeting with my mentor Eva Åkesson happened in December 2021, and we started arranging meetings every month afterward. Thank you for your patience and caring - listening to my problems and providing valuable suggestions every time, especially when I start writing the thesis and planning the defence. I have enjoyed each meeting and the relaxing atmosphere.

Thanks to all the people who have helped me during the past four years. Yang and Li, my ‘chef’ friend and gaming pal, thanks for all the joy you have brought in the first two years. Hope we can meet again soon and have fun like old times. Chen, Fan, Jingyuan and Xianshao, thanks for the company, helping me in my endless loop of moving-in and moving-out, and inviting me to various delightful activities. Qi, thanks for helping me settle down in Lund when I arrived and for all the life tips. Sol, thank you for all the happy hours we spent together in theme parks and for showing me around Copenhagen. Mingli and Jie, thank you for all the help with projects and valuable discussions. Zehan and Yue, thank you for helping in the

division kitchen and inviting me to your place. Thanks to my ‘tofu box’ mates, Albin, Edoardo A. and Linnea for all the fun times in our office and for inviting me to many other activities. Thanks to Alireza, Pavel and Torbjorn for the extensive help in the Millennia lab. Thanks to all members of Tõnu’s group, Zhengjun, Yanmei, Junsheng and Anurag for all the valuable group meetings and discussions. Thanks to all members of Kaibo’s group at the Technical University of Denmark (DTU), Qian and Qinying. Thanks to Shraddha, Romain, Chuanshuai, Yong, Sudipta, Lintang, Yen and Edoardo D. for all the delightful chatting in the division. Thanks to Donatas, Ivan, Arkady, Ebbe, Per and Jens for help and discussions in the course and seminars. Thanks to Maria for all the helpful emails during defence planning. I would like to also thank Sophie, Yuran, and all collaborators for helping with projects and extensive discussions.

Thanks to all the friends who have been helping in proofreading.

Juanzi, thank you for all the caring and support in work and in life, especially for giving me a push when I am unmotivated on writing the thesis. Looking forward to having more adventures with you.

My greatest thanks to my family, my parents, grandparents, aunts, uncles, cousins, niece and nephew. Your love teaches me how to embrace love and gives me the bravery to start new journey. A lot has happened at home since my last return, and it would be impossible for me to persevere in my Ph.D. study without your comfort and encouragement. I sincerely hope the reunion can happen soon in the future.

祝愿大家：身康体健，小得盈满。

List of Publications

This doctoral thesis is based on the following papers, which will be referred to in the text by their Roman numerals.

I. Combining Two-Photon Photoemission and Transient Absorption Spectroscopy to Resolve Hot Carrier Cooling in 2D Perovskite Single Crystals: the Effect of Surface Layer
W. Lin[⊥], M. Liang[⊥], Y. Niu, Z. Chen, M. Cherasse, J. Meng, X. Zou, Q. Zhao, H. Geng, E. Papalazarou, M. Marsi, L. Perfetti, S. E. Canton, K. Zheng, T. Pullerits.
Accepted by *J. Mater. Chem. C*. (2022).

I developed a procedure for preparing 2D perovskite flakes, suitable for optical measurments and carried out transient absorption studies of the flakes. With help of co-authors we performed time-resolved two-photon photoemission spectroscopy and low-energy electron diffraction measurements. I analysed the data and discussed interpretation of the results with KZ and TP. I wrote the first version of the manuscript and participated in finalizing it.

II. Electronic Structure and Trap States of Two-Dimensional Ruddlesden–Popper Perovskites with the Relaxed Goldschmidt Tolerance Factor
M. Liang[⊥], W. Lin[⊥], Z. Lan, J. Meng, Q. Zhao, X. Zou, I. E. Castelli, T. Pullerits, S. E. Canton, K. Zheng.
ACS Appl. Electron. Mater. **2020,** *2* (5), 1402-1412.

I carried out the optical measurements and performed the related analysis together with ML. I participated in the discussions and wrote parts of the article related to the Raman measurements.

III. Free Carriers versus Self-Trapped Excitons at Different Facets of Ruddlesden–Popper Two-Dimensional Lead Halide Perovskite Single Crystals
M. Liang, W. Lin, Q. Zhao, X. Zou, Z. Lan, J. Meng, Q. Shi, I. E. Castelli, S. E. Canton, T. Pullerits, K. Zheng.
J. Phys. Chem. Lett. **2021,** *12* (20), 4965-4971.

I performed optical measurements and related analyses together with ML.

IV. Optimizing the quasi-equilibrium state of hot carriers in all-inorganic lead halide perovskite nanocrystals through Mn doping: fundamental dynamics and device perspectives
J. Meng, Z. Lan, W. Lin, M. Liang, X. Zou, Q. Zhao, H. Geng, I. E. Castelli, S. E. Canton, T. Pullerits, K. Zheng.
Chem. Sci. **2022,** *13* (6), 1734-1745.

I performed transient absorption measurements and participated in the related discussions about the data interpretation.

V. Spatially Resolved Local Electronic Properties of Two-Dimensional Lead Halide Perovskite Single Crystals Studied by X-ray Photoemission Electron Microscopy
M. Liang[⊥], W. Lin[⊥], Q. Zhao, L. Zhu, B. Sarpi, A. Zakharov, T. Pullerits, Y. Niu, S. E. Canton, K. Zheng
Manuscript. (2022).

I performed the measurements together with ML under the supervision of the beamline scientist YN. I participate in the discussions and manuscript writing.

Publications not included in this thesis:

VI. Revisiting the structure and the carrier-dynamics of lead-free bismuth perovskite nanocrystals processed by a modified hot injection method
H. Geng, Z. Huang, H. Geng, S. Liu, M. A. Naumova, R. Salvia, S. Chen, J. Wei, L. Zhang, X. Zou, W. Lin, X. Cai, M. Yuan, Z. Hu, K. Zheng, X. Shen, R. Yu, S. E. Canton, X. Fu.
Manuscript. (2022).

VII. N-doping of nonfullerene bulk-heterojunction organic solar cells strengthens photogeneration and exciton dissociation
J. Xie, W. Lin, G. C. Bazan, T. Pullerits, K. Zheng, Z. Liang.
J. Mater. Chem. A **2022**, DOI: 10.1039/d2ta05078a.

VIII. Inorganic ligands-mediated hole attraction and surface structural reorganization in InP/ZnS QD photocatalysts studied via ultrafast visible and midinfrared spectroscopies
Y. Liu, Y. Zhou, M. Abdellah, W. Lin, J. Meng, Q. Zhao, S. Yu, Z. Xie, Q. Pan, F. Zhang, T. Pullerits, K. Zheng.
Sci. China Mater. **2022,** *65* (9), 2529–2539.

IX. Ultrafast charge transfer dynamics in 2D covalent organic frameworks/Re-complex hybrid photocatalyst
Q. Pan, M. Abdellah, Y. Cao, W. Lin, Y. Liu, J. Meng, Q. Zhou, Q. Zhao, X. Yan, Z. Li, H. Cui, H. Cao, W. Fang, D. A. Tanner, M. Abdel-Hafiez, Y. Zhou, T. Pullerits, S. E. Canton, H. Xu, K. Zheng.
Nat. Commun. **2022,** *13*, 845.

X. Charge Carrier Diffusion Dynamics in Multisized Quaternary Alkylammonium-Capped $CsPbBr_3$ Perovskite Nanocrystal Solids
S. Gutiérrez Álvarez, W. Lin, M. Abdellah, J. Meng, K. Žídek, T. Pullerits, K. Zheng.
ACS Appl. Mater. Interfaces **2021,** *13* (37), 44742-44750.

XI. The piezotronic effect on carrier recombination processes in InGaN/GaN multiple quantum wells microwire
X. Zou, J. Dong, K. Zhang, W. Lin, M. Guo, W. Zhang, X. Wang.
Nano Energy **2021,** *87*, 106145.

XII. Manipulating crystallization dynamics through chelating molecules for bright perovskite emitters
Y. Zou, P. Teng, W. Xu, G. Zheng, W. Lin, J. Yin, L. Kobera, S. Abbrent, X. Li, J. A. Steele, E. Solano, M. B. J. Roeffaers, J. Li, L. Cai, C. Kuang, I. G. Scheblykin, J. Brus, K. Zheng, Y. Yang, O. F. Mohammed, O. M. Bakr, T. Pullerits, S. Bai, B. Sun, F. Gao.
Nat. Commun. **2021,** *12*, 4831.

XIII. Ultrafast Spectroelectrochemistry Reveals Photoinduced Carrier Dynamics in Positively Charged CdSe Nanocrystals
A. Honarfar, P. Chabera, W. Lin, J. Meng, H. Mourad, G. Pankratova, L. Gorton, K. Zheng, T. Pullerits.
J. Phys. Chem. C **2021,** *125* (26), 14332-14337.

XIV. Graphitic Carbon Nitride/CdSe Quantum Dot/Iron Carbonyl Cluster Composite for Enhanced Photocatalytic Hydrogen Evolution
C. Li, X. Zou, W. Lin, H. Mourad, J. Meng, Y. Liu, M. Abdellah, M. Guo, K. Zheng, E. Nordlander.
ACS Appl. Nano Mater. **2021,** *4* (6), 6280-6289.

XV. Mixed halide perovskites for spectrally stable and high-efficiency blue light-emitting diodes
M. Karlsson, Z. Yi, S. Reichert, X. Luo, W. Lin, Z. Zhang, C. Bao, R. Zhang, S. Bai, G. Zheng, P. Teng, L. Duan, Y. Lu, K. Zheng, T. Pullerits, C. Deibel, W. Xu, R. Friend, F. Gao.
Nat. Commun. **2021,** *12*, 361.

XVI. Manganese doped eco-friendly $CuInSe_2$ colloidal quantum dots for boosting near-infrared photodetection performance
R. Guo, J. Meng, W. Lin, A. Liu, T. Pullerits, K. Zheng, J. Tian.
Chem. Eng. J. **2021,** *403*, 126452.

XVII. Photoexcitation Dynamics in Electrochemically Charged CdSe Quantum Dots: From Hot Carrier Cooling to Auger Recombination of Negative Trions
A. Honarfar, H. Mourad, W. Lin, A. Polukeev, A. Rahaman, M. Abdellah, P. Chábera, G. Pankratova, L. Gorton, K. Zheng, T. Pullerits.
ACS Appl. Energy Mater. **2020,** *3* (12), 12525-12531.

XVIII. Exploring the light-induced dynamics in solvated metallogrid complexes with femtosecond pulses across the electromagnetic spectrum
M. A. Naumova, A. Kalinko, J. W. L. Wong, S. Alvarez Gutierrez, J. Meng, M. Liang, M. Abdellah, H. Geng, W. Lin, K. Kubicek, M. Biednov, F. Lima, A. Galler, P. Zalden, S. Checchia, P.-A. Mante, J. Zimara, D. Schwarzer, S. Demeshko, V. Murzin, D. Gosztola, M. Jarenmark, J. Zhang, M. Bauer, M. L. Lawson Daku, D. Khakhulin, W. Gawelda, C. Bressler, F. Meyer, K. Zheng, S. E. Canton.
J. Chem. Phys. **2020,** *152* (21), 214301.

XIX. Mechanistic Investigation into Dynamic Function of Third Component Incorporated in Ternary Near-Infrared Nonfullerene Organic Solar Cells
Z. Wang, J. Ji, W. Lin, Y. Yao, K. Zheng, Z. Liang.
Adv. Funct. Mater. **2020,** *30* (31), 2001564.

XX. Modulating Charge-Carrier Dynamics in Mn-Doped All-Inorganic Halide Perovskite Quantum Dots through the Doping-Induced Deep Trap States
J. Meng, Z. Lan, M. Abdellah, B. Yang, S. Mossin, M. Liang, M. Naumova, Q. Shi, S. L. Gutierrez Alvarez, Y. Liu, W. Lin, I. E. Castelli, S. E. Canton, T. Pullerits, K. Zheng.
J. Phys. Chem. Lett. **2020,** *11* (9), 3705-3711.

XXI. Electron Transfer Mediated by Iron Carbonyl Clusters Enhance Light-Driven Hydrogen Evolution in Water by Quantum Dots
C. Li, A. Rahaman, W. Lin, H. Mourad, J. Meng, A. Honarfar, M. Abdellah, M. Guo, M. G. Richmond, K. Zheng, E. Nordlander.
ChemSusChem **2020,** *13* (12), 3252-3260.

XXII. Revealing Hot and Long-Lived Metastable Spin States in the Photoinduced Switching of Solvated Metallogrid Complexes with Femtosecond Optical and X-ray Spectroscopies
M. A. Naumova, A. Kalinko, J. W. L. Wong, M. Abdellah, H. Geng, E. Domenichini, J. Meng, S. A. Gutierrez, P.-A. Mante, W. Lin, P. Zalden, A. Galler, F. Lima, K. Kubicek, M. Biednov, A. Britz, S. Checchia, V. Kabanova, M. Wulff, J. Zimara, D. Schwarzer, S. Demeshko, V. Murzin, D. Gosztola, M. Jarenmark, J. Zhang, M. Bauer, M. L. Lawson Daku, W. Gawelda, D. Khakhulin, C. Bressler, F. Meyer, K. Zheng, S. E. Canton.
J. Phys. Chem. Lett. **2020,** *11* (6), 2133-2141.

XXIII. Defect State Assisted Z-scheme Charge Recombination in $Bi_2O_2CO_3$/Graphene Quantum Dot Composites For Photocatalytic Oxidation of NO
Y. Liu, Y. Zhou, S. Yu, Z. Xie, Y. Chen, K. Zheng, S. Mossin, W. Lin, J. Meng, T. Pullerits, K. Zheng.
ACS Appl. Nano **2020,** *3* (1), 772-781.

Abbreviations

2D	two-dimensional
BBO	beta barium borate
CB	conduction band
CBM	conduction band minimum
DFT	density functional theory
DJ	Dion–Jacobson
DOS	density of state
EA	electron affinity
EF	Fermi level
ESA	excited-state absorption
ESC	energy selective contact
FE	free exciton
FWHM	full width at half maximum
GSB	ground-state bleach
HC	hot carrier
HCSC	hot carrier solar cell
IE	ionization energy
IRF	instrument response function
KE	kinetic energy
LA	longitudinal acoustic
LEED	low-energy electron diffraction
LES	low-energy edge states
LO	longitudinal optical
LR	long-range

MHP	metal halide perovskite
MQW	multiple quantum well
NCs	nanocrystals
PCE	power conversion efficiency
PeLED	perovskite light-emitting diodes
PL	photoluminescence
PSC	perovskite solar cell
PV	photovoltaic
QY	quantum yield
RP	Ruddlesden–Popper
SE	stimulated emission
SPAD	single photon avalanche diode
SQ	Shockley-Queisser
SR	short-range
STE	self-trapped excitons
TA	transient absorption
TCSPC	time-correlated single photon counting
tr-ARPES	time-resolved angle-resolved photoelectron spectroscopy
tr-2PPE	time-resolved two-photon photoemission
TRPL	time-resolved photoluminescence
VAC	vacuum level
VB	valence band
VBM	valence band maximum
WF	work function
XANES	X-ray absorption near edge spectroscopy
XAS	X-ray absorption spectroscopy
XPEEM	X-ray photoemission electron microscopy
XPS	X-ray photoelectron spectroscopy
XRD	X-ray diffraction

1 Introduction

1.1 Solar Cell

Due to climate change and increasing demand for energy, the green, low-carbon, diversified and sustainable energy sources have attracted much attention. Techniques for acquiring renewable energy such as hydroelectricity, biomass, geothermal, wind and solar energy have been developed over decades. Because of the enormous amount of available sunlight, a photovoltaic (PV) device, that can directly convert solar energy into electricity, has wide developmental and applied prospects.[1-4] Generally PVs can be divided into multijunction cells, single-junction gallium arsenide solar cells, crystalline silicon solar cells, thin film solar cells and new-generation solar cells. The latter include perovskite-based solar cells, polymer-based solar cells, quantum dot solar cells and dye-sensitized solar cells. To compare the different solar cell devices, power conversion efficiency (PCE) is often used as a critical characteristic. PCE has been steadily improved through the efforts of researchers. The development of PVs is shown in **Figure 1.1**. Nowadays, the PCE of multijunction cells can reach as high as 47.1%, but commercial use of such cells is so far limited due to their high manufacturing complexity and cost. Therefore, new-generation PV technologies are emerging targeting cheap alternatives and simple fabrication methods.

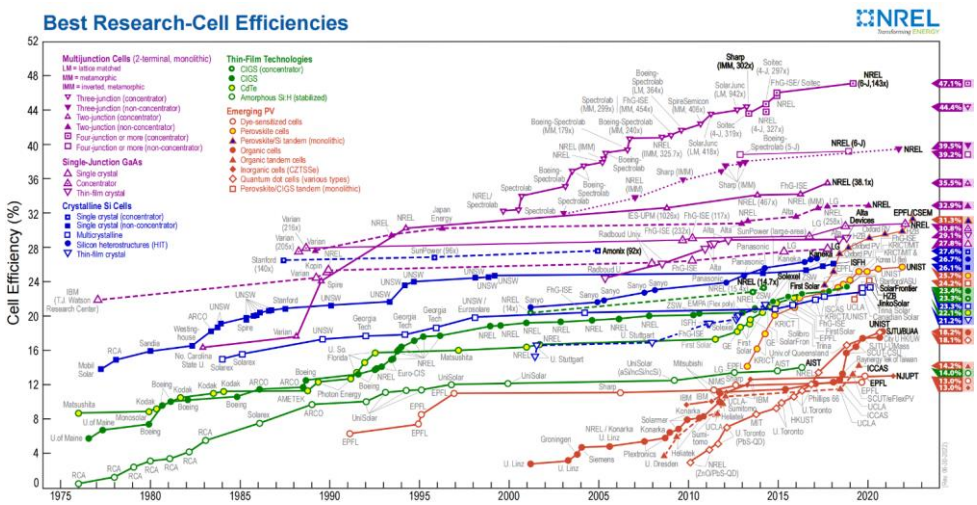

Figure 1.1 *Power conversion efficiencies for photovoltaic technologies since 1976. This plot is courtesy of the National Renewable Energy Laboratory, Golden, CO.*

Based on Shockley-Queisser (SQ) theory,[5] the maximum efficiency that a single junction cell with ~1.3 eV bandgap under AM1.5 illumination can reach is theoretically predicted as 33%. To overcome the SQ limit, several strategies are investigated to minimize the fundamental loss channels. For example carrier multiplication[6-7] where extra carriers are generated to enhance photocurrent, and hot carrier extraction[8-9] where the lost energy is recycled to lift photovoltage. The latter idea is the fundamental principle of hot carrier solar cells (HCSCs).[10-12] The structure of HCSC is simplified as a hot carrier absorber material sandwiched by two energy selective contacts (ESC), as shown in **Figure 1.2a**. The energy diagram of HCSC is shown as **Figure 1.2b**. The idea of HCSC was proposed by Ross and Nozik in 1982,[13] where the photogenerated carriers are extracted via ESCs before their excess energy is mostly lost. A great portion of absorbed energy might be wasted as heat (25%) as shown in **Figure 1.2c**. The PCE of HCSC can be pushed above 50%, which is much exceeding the SQ limit. This has drawn the wide attention of researchers who are trying to understand the intrinsic mechanisms of suitable materials for developing HCSC.

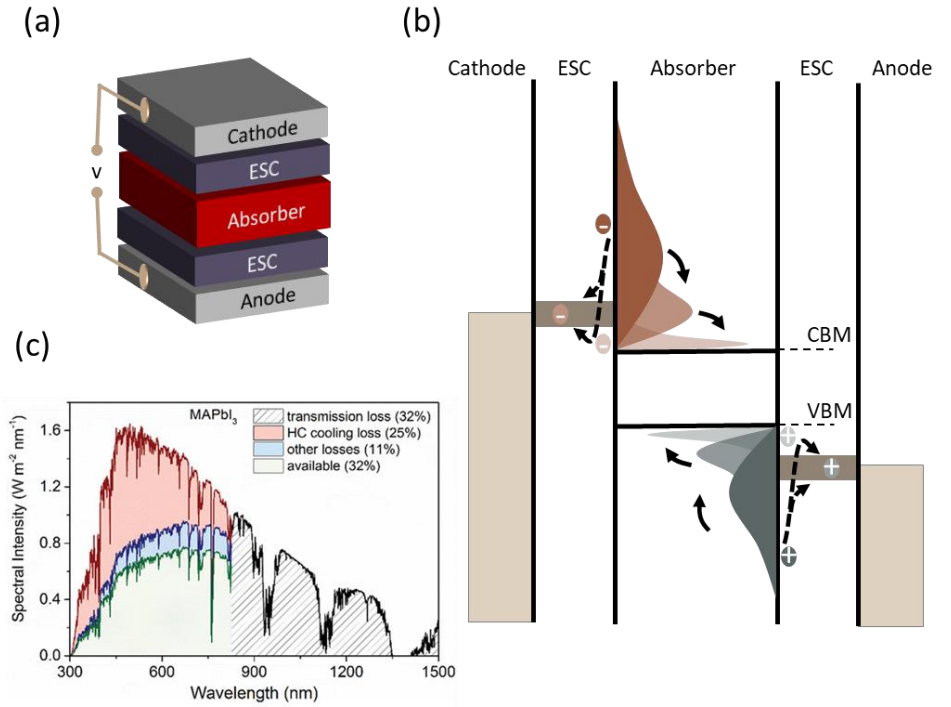

Figure 1.2 *Principle of hot carrier solar cell (HCSC). (a) Schematic diagram of HCSC device, where ESC represents energy selective contact. (b) Energy schematic of HCSC, where conduction band minimum CBM and valence band maximum VBM are marked. The extraction energy of ESC needs to be suitably narrow, so that the HC can reheat cold carriers for improving device efficiency. (c) Illustration of losses in a single junction perovskite solar cell over the solar spectrum. Figure was adapted from Ref 12 with permission. The fundamental idea of HCSC lies in recycling the energy wasted in HC cooling and pushing the power conversion efficiency of the device above the Shockley-Qussier limit.*

1.2 Metal Halide Perovskite

In 1839, the calcium titanate ($CaTiO_3$) mineral was discovered by Gustav Rose and was named as perovskite in honor of mineralogist Lev Perovski.[14] Later the usage of name was extended to describe compounds with the same type of crystal structure. Inorganic lead halide perovskite was synthesized by Wells in 1893,[15] and organic-inorganic hybrid perovskite was first reported by Weber in 1978.[16] In the last decade metal halide perovskite (MHP) has become an up-rising star in the optoelectronic device field, including perovskite solar cells,[3, 17-18] light-emitting diodes,[19-20] lasers and photodetectors[21]. The perovskite-based PV devices have been developed over years, such as perovskite solar cells (PSCs) with PCE of more than 25% as shown

in **Figure 1.1**, and metal halide perovskite light-emitting diodes (PeLEDs) with boosted external quantum efficiency above 20%.[22] The simple and low-cost solution process in perovskite preparation enables its potential of substituting for presently commercial photovoltaic technologies.[23] In recent years, perovskite also has received wide attention as a suitable absorber material for HCSC devices.

1.2.1 Three-Dimensional Perovskite

The chemical formula of MHPs can be described as ABX_3, where anion X is a halogen (e.g. Cl^-, Br^-, I^-), the A is a monovalent cation (e.g. MA = $CH_3NH_3^+$, FA = $CH(NH_2)_2^+$, Cs^+, Rb^+) and B is a divalent metal cation (e.g. Pb^{2+}, Sn^{2+}). The crystal structure of perovskite can be viewed as A cation centered in the corner-shared $(BX_6)^{4-}$ octahedra cage, as shown in **Figure 1.3a**. For different A-site cations, the MHPs can be classified as organic-inorganic hybrid perovskites or inorganic perovskites. If the ions are too small or too big, the crystal structure is unstable. The empirical Goldschmidt's tolerance factor (t) and octahedral factor (μ) are widely used to predict the formation and stability of perovskite structure.[24]

$$t = \frac{r_A + r_X}{\sqrt{2}(r_B + r_X)}\,, \tag{1.1}$$

$$\mu = \frac{r_B}{r_X}\,, \tag{1.2}$$

where r_A, r_B and r_X are the ionic radii for A, B and X ions in ABX_3 perovskite, respectively. For $APbI_3$ perovskite, the range of tolerance factor is generally between 0.8 and 1.0, and octahedral factor is larger than 0.41.[25] The tolerance factors of MHPs with different A cations are listed in **Figure 1.3b**, which charts the systems with a too low or two high tolerance factors that are not able to form a stable perovskite structure.[26-27] In addition, different perovskites have diverse phase transition temperatures.[28-29] The influence of phase transition needs to be carefully considered when analyzing charge carrier dynamics since it can alter the electronic band structure significantly.[30-31] For the archetypal hybrid perovskite $MAPbI_3$, the transitions from cubic phase to tetragonal phase to orthorhombic phase occur at 330 K and 160 K, respectively.[32]

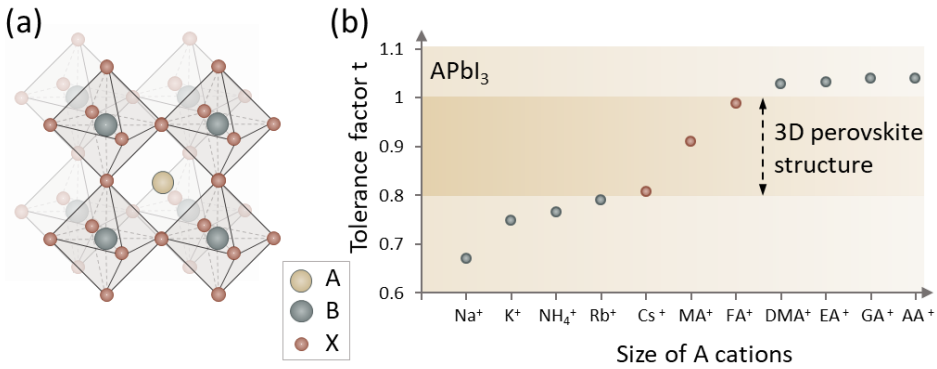

Figure 1.3 *Structure of metal halide perovskite (MHP). (a) Crystal structure of MHPs with formula as ABX_3. (b) Tolerance factors of MHPs with different A cations, where the B cation is Pb^{2+} and halogen X is I^-, and range of tolerance factor is between 0.8 and 1.0 for forming stable three-dimensional (3D) perovskite structure.*

The performance of perovskite in solar cell applications is approaching the best inorganic PV materials, due to its effective light absorption, narrow and tunable emission bandwidth, balanced charge carrier transport, slow charge carrier recombination rate, high photoluminescence quantum yield, etc.[33-38] Its high-quality properties are unexpected for a material produced from solution process at low temperature and the functional material properties are preserved with mitigated impact from crystalline defects – thus labeled as defect tolerant material.[39] The band structure of perovskite gives a hint about the reasons for its defect tolerance and unique optoelectronic properties.

As shown in **Figure 1.4**, the conduction band minimum (CBM) and valence band maximum (VBM) originate from antibonding orbitals of lead and halide atoms, arising from hybridization as Pb(6p)-I(5p) and Pb(6s)-I(5p), respectively. Even though the bottom of conduction band (CB) does not match the optimal bonding character for defect tolerance, the strong spin-orbit coupling effect in perovskite leads to the beneficial band broadening and shifts the CBM to be below Pb(6p) atomic orbital and increase the possibility of defects forming intra-CB states.[40] It is also found that defects in perovskite can appear as shallow traps (near the band edge), which are not detrimental to device performance compared with deep trap states.[41] In addition, the direct bandgap (silicon has indirect bandgap) and high transition probability between edges of CB and valence band (VB) (about two orders of magnitude higher than GaAs) enable the application of ultrathin perovskite film as an efficient absorber layer.[42] There are other outstanding properties of perovskite correlating to its electronic structure, such as electrically-benign grain boundaries, long and balanced charge carrier diffusion length and slow carrier recombination.[43]

The high-quality optoelectronic properties, composition-tunability, inexpensive and simple solution processing method qualify perovskite as a superior material for solar cell applications. It encourages researchers to further explore and develop perovskite solar cells.

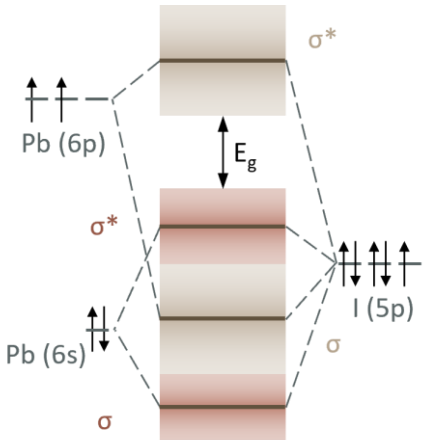

Figure 1.4 *Schematic representation of bonding and band structure of $APbI_3$ perovskite. σ represents the bonding and σ* represents the antibonding of orbitals.*

1.2.2 Two-Dimensional Perovskite

Perovskite solar cells have been developed unprecedentedly in the past decade, but many challenges still remain, especially the poor thermal and moisture stability.[44] To improve the long-term stability, many studies are conducted on optimizing perovskite absorbers and device fabrication.[45-47] Among all, inserting large organic spacing cations in between inorganic slabs can greatly improve the device stability when subjected to light, heat and humidity.[48] The resulting perovskites have a self-assembled multiple-quantum-well (MQW) structure and are named as two-dimensional (2D) perovskite, or quasi-2D perovskite, within which the inorganic sheets and organic spacer are alternatingly arranged in one direction. The MQW structure makes 2D perovskite an interesting material for various optoelectronic applications.[49-50] 2D perovskites with Ruddlesden–Popper (RP) phases and Dion–Jacobson (DJ) phases are commonly reported.[51-52] The difference between these two phases is that the RP phase contains two monocationic spacers while DJ phase contains only one dication spacer in one unit cell.[53] The general formula of 2D RP perovskite is $(A')_2A_{n-1}B_nX_{3n+1}$, where A' is the monovalent organic spacer (e.g., n-butylamine (BA^+), phenylethlammonium (PEA^+)), A is the cation inside the octahedra cage (e.g., methylammonium (MA^+)), B is the metal cation (e.g. Pb^{2+}), X is a halogen (e.g. I^-) and the *n*-value represents the number of octahedral layers (**Figure 1.5**).

Since the first report of 2D perovskite solar cell with PCE of 4.73%,[54] the efficiency was significantly improved over years to above 21%.[55] Apart from using pure-2D perovskite as absorber material, the profound potential lies in mixing perovskites with different *n*-values (including 3D perovskite as $n = \infty$) as a favorable 'energy funnel/cascade' structure.[56] The bandgap of 2D perovskite can be adjusted by varying the thickness of inorganic sublattice and the photoexcitations can be funneled into the lowest-bandgap emitter in the device. [57] In addition, the selection of composition for stable structure is extended compared to 3D perovskite, because the Goldschmidt tolerance factor requirement is relaxed in 2D perovskites due to the flexible structure, meaning that the large cations can be contained in the octahedra cage with lattice distorted.[58]

All in all, the natural MQW structure, tunability of optical and electronic properties, flexible structure and enhanced stability make 2D perovskite an attractive candidate for exploring photoelectronic applications and further developing perovskite solar cell devices.[56]

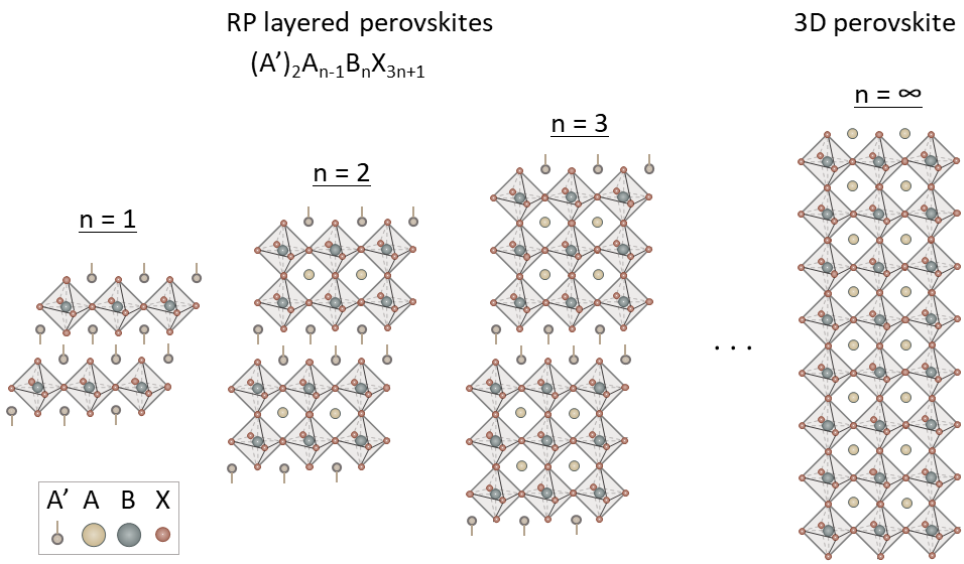

Figure 1.5 *Crystal structure of two-dimensional Ruddlesden-Popper (RP) perovskite and three-dimensional perovskite. A' is the long-chain organic spacers, A is the cation in the octahedral cage, B is the metal cation, X is the halide anion and n represents the number of octahedral layers in one unit cell.*

1.3 Hot Carrier Relaxation

As mentioned before, HCSC is a promising concept to exceed SQ limit and within which the selection of absorber material is a critical part to fabricate high-quality HCSC. Materials with high absorption coefficient, long carrier diffusion length and slow charge carrier recombination are generally preferred for PV applications. A special requirement for absorber material in HCSC application is that its HC lifetime should be sufficiently long for recycling the energy before heat dissipation. The potential of various materials being decent candidates have been investigated over years.[59] Illustration of HC cooling in HCSC is shown in **Figure 1.2b**. To improve the PCE, the rate of HC cooling needs to be slower than carrier separation and transportation for increasing photovoltage,[60-61] or the rate of impact ionization (i.e. inverse Auger effect) for increasing photocurrent.[62-63] In most conventional semiconductors, the lifetime of hot carriers is limited in sub-ps timescale, but lead halide perovskite might be an exception according to current reports.[64-65] To address the potential of perovskite and related mechanisms, fundamental processes involved in HC relaxation will be first introduced.

1.3.1 General Pathway of Hot Carrier Cooling

After the absorption of a photon with energy higher than the band gap, an electron is generated in the conduction band and leaves behind a hole in the valence band. The energy difference between the excitation and band gap is named as excess energy, which will be distributed to electron and hole as:[66]

$$\Delta E_e = \left(h\upsilon - E_g\right)[1 + m_e^*/m_h^*]^{-1}\,, \tag{1.3}$$

$$\Delta E_h = \left(h\upsilon - E_g\right) - \Delta E_e\,, \tag{1.4}$$

where the m_e^* and m_h^* are the effective masses of electrons and holes, ΔE_e is the energy difference between the initial excited level of photogenerated electron and CBM, and ΔE_h is the energy difference between the initial excited level of photogenerated hole and VBM. The excess energy of system shows as the kinetic energy of charge carriers. When the photon energy is significantly greater than the band gap, the carriers populate far from the band edge and are at non-equilibrium status. The charge carriers with excess energy will lose energy via various scattering processes and eventually equilibrate with environmental (lattice) temperature.

- *Dephasing*

After the photoexcitation with an ultrashort laser pulse, there will be a regime where the oscillations of free e-h pairs are in phase before the first collision happens (mainly involve either another carrier or a phonon), considering the carrier recombination happens in a very late timescale. The coherent behavior is lost at an

extremely fast rate and the decay rate can be described by dephasing time. The four-wave mixing measurement can be conducted for observing the ultrafast coherence decay. Based on many measurements on samples with different morphology or temperature, the upper limit of the coherence timescale of 3D perovskite can be put as within 20 fs at room temperature.[67-68]

- *Carrier-carrier scattering*

Hot carriers will exchange energy among themselves after photoexcitation, which will not cause the loss of total system energy but affect the HC relaxation indirectly. In addition, the strong carrier-carrier scattering can limit the carrier mobility under high excitation densities. The process in which charge carriers exchange the energy towards forming a thermal distribution, is labeled as carrier thermalization in the ultrafast field, even though in other fields it can be used to represent the overall cooling of HC in semiconductors. With the help of two-dimensional electronic spectroscopy with high energy resolution, the initial carrier distribution can be visualized and the scattering rates which lead to the HC re-distribution can be obtained.[69] The results show that the carrier thermalization rate in perovskite depends on the excess energy and density of carriers, unlike GaAs, indicating the dominant mechanism being the carrier-carrier scattering (< 100 fs under moderate excitation intensity). The carrier thermalization is faster in perovskite than GaAs under similar excitation conditions, which could be due to the weak Coulomb screening effect in perovskite.[70-71] The previous description is based on pulse laser excitation. The situation will be different under continuous excitation, for example standard sunlight illumination. If the carrier lifetime is long enough or the HC extraction is designed inefficiently, the cold population of carriers in the bottom of conduction band will cause the rapid loss of excess energy of HC and will play a significant role in defining the timescale of carrier thermalization.[69]
After elastic carrier-carrier scattering, the energetic carriers thermalize to a quasi-equilibrium state which can be characterized by Fermi-Dirac distribution. It can be approximated as a Boltzmann distribution because carriers locate in the high energy regime (excess energy >> quasi-Fermi energy E_f). At this status, the Boltzmann distribution of carriers can be determined by the system temperature (separately assign the electron and hole temperature). The carriers with excess energy of at least kT, meaning that their initial carrier temperatures are above the lattice temperature, are labeled as '*hot'* carriers.

- *Carrier-phonon scattering and phonon decay*

After carrier-carrier scattering, carriers with elevated temperatures will further lose energy by equilibrating to lattice via carrier-phonon scattering, where the excess energy of carriers is transferred to phonons. Phonons are quasiparticles with discrete energy $\hbar\omega$, used to represent modes of vibrations in the elastic and periodic arrangement of atoms in the semiconductors.[72] The phonons are labeled as *acoustic*

when neighboring atoms move collectively towards one direction with relative position unchanged, whereas they are *optical* phonons, when the atoms undergo relative change in their positions. In addition, based on the displacement direction being parallel or perpendicular to wave-vector *k*, phonons can be classified into *longitudinal* and *transverse*. The schematic of longitudinal optical (LO) phonon and longitudinal acoustic (LA) phonon are shown in **Figure 1.6**.

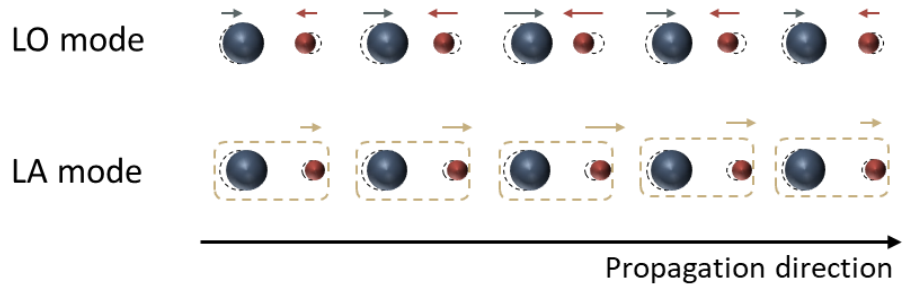

Figure 1.6 *Schematic of longitudinal optical (LO) phonon and longitudinal acoustic (LA) phonon. In optical mode, the atoms of the unit cell oscillate in respect of each other, while in acoustic mode, the unit cells oscillate with respect to each other. Longitudinal waves mean that the vibration of the lattice is parallel to the wave propagation.*

In general, there are different ways that lattice vibration can affect the charge carrier motions, such as Fröhlich interaction with LO phonons, deformation potential interaction with optical and acoustic phonons, and piezoelectric interaction with acoustic phonons.[73] In polar semiconductors, Fröhlich interaction which is the Coulomb interaction between carriers and longitudinal electric field from LO phonons, is generally agreed for governing the HC relaxation in the early cooling stage.[74-75] This intra-band HC cooling results in the emission of LO phonons, and the energy and momentum are conserved during the cooling processes in the combination of electron and emitted phonons. The carriers interact with the macroscopic electric field arising from the out-of-phase displacement of oppositely charge atoms (LO phonon mode) via Coulomb interaction. The interactions between free carriers and phonons cover only a small wave-vector range, $k \approxeq 0$. Following, the emitted zone-center optical photons can re-heat the free electrons or further decay to counterpropagating acoustic phonons due to lattice anharmonicity via Klemens,[76] Ridley,[77-78] Vallée-Bogani,[79] and other channels.[80-81] The routes of LO phonon decay are shown in **Figure 1.7**. The decision of mechanisms is based on a relatively simple (symmetric) crystal structure and thus the decrease in the symmetry will increase the complexity of decay routes.

Among all decay routes, Klemens decay is the most efficient channel in polar semiconductors.[82] During Klemens decay, an optical phonon with k_0 decays into two acoustic phonons, which must fulfill momentum and energy conservation as $k_0 = k_1 + k_2$ and $\hbar\omega_O(k_0) = \hbar\omega_A(k_1) + \hbar\omega_A(k_2)$. Therefore, the zone-center LO phonon will decay into two acoustic phonons half of its energy, as well as equal and opposite

momenta. Klemens decay can be hindered significantly if the phononic band gap is greater than twice the highest energy of acoustic phonon.[59]
In the next cooling stage, the energy is released as heat through acoustic phonon and eventually the lattice equilibrates to the environment temperature. Meanwhile, it is not significant in polar semiconductors that HC will cool down via acoustic phonon emission, since the acoustic phonons have rather small energies for the k-vectors of interest. In addition, energy loss through heat dissipation from the LO phonon to environment is considered negligible due to its negligible group velocity (low thermal conductivity).[83]

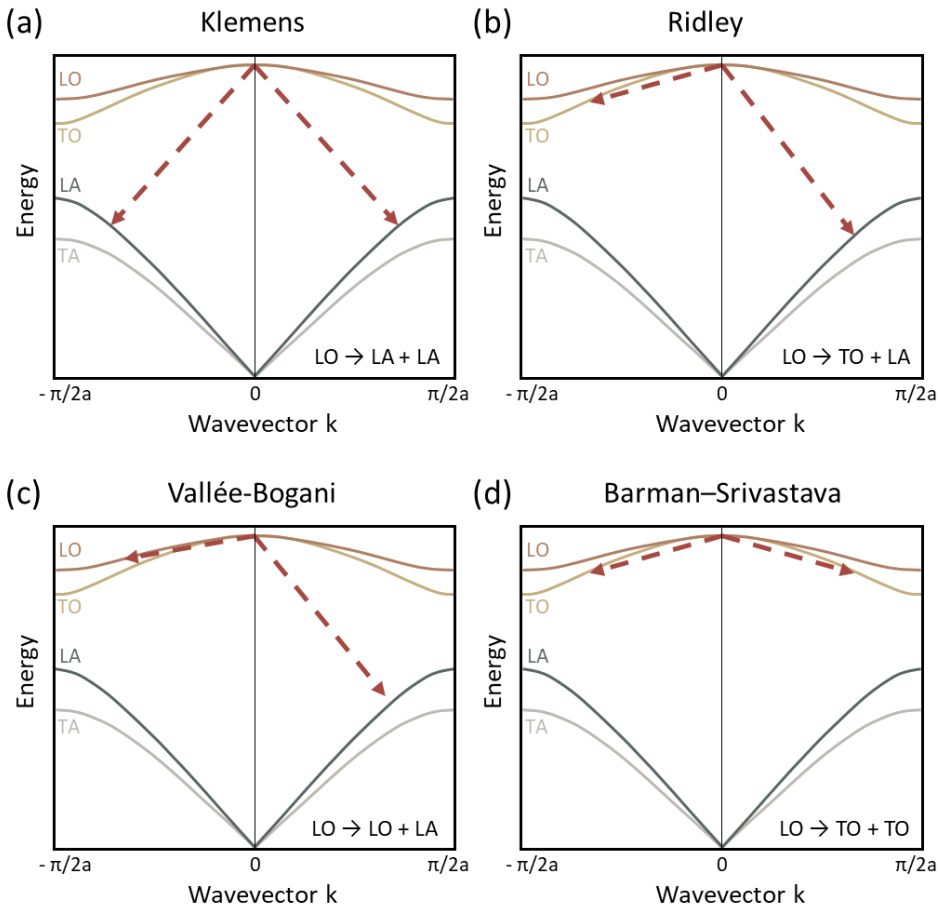

Figure 1.7 *Phonon decay routes from zone-centre LO phonons to phonons with smaller energies, where Klemens decay is the most efficient channel in polar semiconductors.*

- *Carrier recombination*

The electrons and holes will recombine, radiatively or non-radiatively, and the system can reach a complete relaxation situation with the carrier population same as before photoexcitation. The photons generated by direct recombination can be re-absorbed by ground state transitions and are beneficial for retarding HC cooling. But the photons from this process will not be included in the discussion of photoexcitation since they are usually near the band edge and have a longer absorption length than the photons which initially created electron-hole pairs.[84] In addition, the carrier recombination will not be included in the discussion of HC relaxation since its timescale is much later than the carrier cooling processes discussed above and the carriers close to the band edge might not have enough energy to be beneficial for improving the efficiency of HCSC.

1.3.2 Mechanisms for Slowing Down Hot Carrier Relaxation

In general, there are two pronounced HC cooling stages presented in investigations on lead halide perovskite after dephasing and carrier thermalization.[12, 85] In the first stage, the HC loses energy via Fröhlich interaction in a sub-picosecond to few ps regime, which mainly occurs between carriers and lead-halide bonds.[86-87] The second stage lies on the several tens of picoseconds to nanosecond scale, where the phonon decay from LO phonon to acoustic phonon plays a role, as well as the further heat dissipation from acoustic phonon to the environment. The timescales for typical photoexcited status are marked in **Figure 1.8**. Noteworthy, the timescale of different regions will overlap and can be significantly affected by the material composition, applied techniques and experimental parameters.

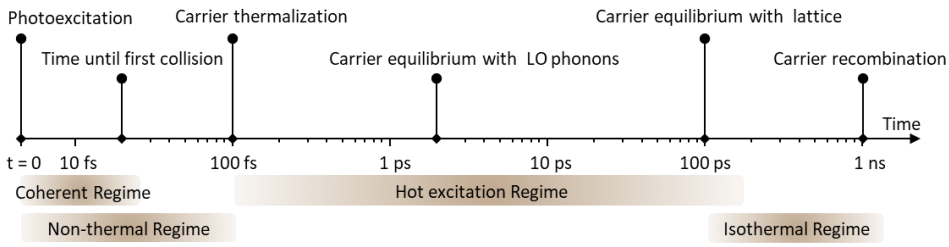

Figure 1.8 *Timescale of four temporally-overlapping HC relaxation regimes in perovskite with typical status marked.*

There are some effects that can significantly affect the HC lifetime in perovskite, including the screening effect, hot phonon bottleneck and Auger heating effect. The screening effect, e.g. polaron formation, can be observed at low fluence with carrier density as around 10^{17} cm^{-3}.[64] The HC cooling can be significantly slowed down by a few orders of magnitude with carrier density being above 5×10^{17} cm^{-3} due to hot phonon bottleneck,[88] which is different compared to the case in GaAs (an order of

magnitude lower in critical carrier density with three orders of magnitude longer HC lifetime in perovskite).[88] At high carrier density (> 10^{19} cm^{-3}),[89] the Auger heating effect is found to prolong HC lifetime significantly in the later timescale with the average carrier temperature close to lattice temperature.

- *Hot phonon bottleneck*

Under strong excitation, it is observed that the carrier cooling rate is reduced due to a non-equilibrium population of phonon bath, and the HC lifetime is significantly prolonged.[85] The effect is named as 'hot phonon bottleneck'. Noteworthy, it is different from the phonon bottleneck effect that was expected in QDs due to the discrete electronic band feature originated from the strong quantum confinement.[90]

Phonon bottleneck: When the inter-level energy gap is substantially higher than the energy of LO phonons,[91] the intra-band electronic transitions require multiple phonon emissions and the carriers are compelled to remain at excited levels with slow relaxation.[92] However, the ultrafast spectroscopic measurements and theoretical calculation show that the lifetime of hot electrons in various types of QDs is in sub-ps to few ps range.[93-97] The multiple phonon emission pathway is bypassed by interstate transitions that require only one emitted phonon followed by a cascade of single phonon intrastate transitions.[92, 98-100] Among possible mechanisms, the most prominent is the Auger-type energy transfer where the excessive energy of a hot electron is transferred to the hole and cools rapidly due to its larger effective mass and smaller energy-level spacing.[95-96] On the other hand, when fabricating the HCSC device, the discrete density of state (DOS) might be a problem for efficient light absorption over a broad spectral range.[101] All in all, the potential of QDs in HCSC application and suppressing Auger-like relaxation are still under investigation.

Hot phonon bottleneck, on the other hand, is confirmed as a comprehensive effect that leads to the prolonged lifetime of HC under high excitation intensity, as shown in **Figure 1.9a**. Under strong external perturbations (e.g., laser excitation), the system will be driven out of equilibrium, and form a non-equilibrium hot phonon population if the main HC relaxation process is via phonon emission. In reverse, it is also possible for the phonon disturbances to feed back to the carrier system, as phonon reabsorption. The energy of the system is not necessarily removed by the phonon emission if the possibility of phonon reabsorption by the carriers is high enough. The hot phonon bottleneck effect has been observed in other polar semiconductors such as GaAs and CdSe.[102] It is found that the hot phonon bottleneck effect has a dependence on carrier density (involve e-ph scattering rate) and environmental temperature relating to the ph-ph scattering rate (decreased at low temperature) due to the lower phonon occupancy.[89, 103] The possibility of phonon reabsorption increases with increasing carrier density, and therefore the hot phonon bottleneck effect is expected to be more significant in high excitation density measurements. Generally hot carrier relaxation kinetic has two cooling stages under moderate or high excitation fluence due to the hot phonon bottleneck

effect, as shown in **Figure 1.9b**, with initial carrier temperature in the later stage being higher under high excitation fluence.

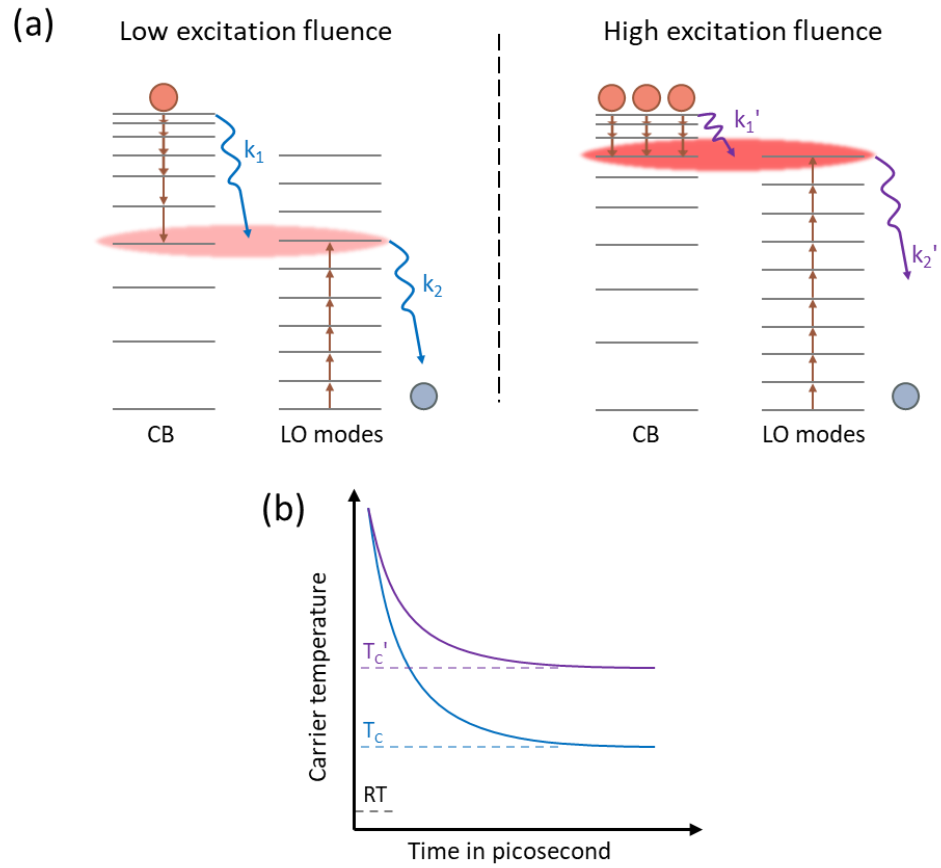

Figure 1.9 *Schematic for hot phonon bottleneck. (a) Illustration of equilibrium between carriers and LO phonons under low and high excitation fluence. CB represents conduction band, k_1 and k_1' represent rate constant of estabilishing carrier-LO phonon equilibrium, and k_2 and k_2' represent HC relaxation after in the later stage until reaching environmental temperature, under low and high excitation fluence respectively. (b) Hot carrier cooling dynamics under low (blue line) and high excitation fluence (purple line). Two cooling stages are generally observed due to the hot phonon bottleneck effect and the initial carrier temperature of the later stage is higher under high excitaiotn fluence compared to under low excitation fluence ($T_c' > T_c$).*

In perovskite, the LO phonons are emitted via carrier-phonon scattering and warmed up by abundant HC. When the energy flow from HC to LO phonons is equal to the phonon reabsorption (backward flow), the population of hot LO phonons hinders the HC relaxation at an elevated carrier temperature like a bottleneck in sub-picosecond. Since the equilibrium between HC and hot LO phonons is reached, the

further cooling rate is corresponding to the phonon decay, which will be in the timescale of few picoseconds. The bottleneck observation in this stage, for example the slow-down of HC relaxation under high excitation intensity, means the carrier density can affect the phonon decay or the heat dissipation to environment, and is also included in the discussion of hot phonon bottleneck effect in some previous references.[88, 104] One possible scenario is that HC relaxation is slowed down because of the partial heating of acoustic phonons,[105] possibly results from the inefficient thermal conductivity of sample.[85]

- *Factors influencing hot phonon bottleneck*

The previously mentioned suppressed LO phonon decay is a possible influencing factor.[89] In this case, the LO phonon emission rate is faster than the phonon decay rate from LO phonon to acoustic phonons, and further leads to the accumulation of non-equilibrium hot LO phonon which can reheat the cooled carriers.[106] Hence, materials whose phonon decay can be hindered would be expected to exhibit a more significant hot phonon bottleneck effect and slowed HC cooling rate.[107] As discussed above, the Klemens decay channel (LO → 2LA) can be suppressed if the phononic band gap is twice greater than the energy of acoustic phonons, which is fulfilled in the perovskites. Take organic-inorganic lead halide perovskite $MAPbI_3$ as an example for calculation, the energy of LO phonon is around 8 meV and of LA phonon is around 2.5 meV.[89] In addition, in the room-temperature 2D electronic spectra analysis, the existence of beating signal corresponding to a coherent optical phonon with long dephasing time suggests the strong coupling between this optical phonon(s) to the electron transition, but weak interaction with other phonon modes.[108]

Another possible scenario is that the non-equilibrium accumulation of LO phonons is enhanced due to the acoustic-optical phonon up-conversion.[85] A-site organic cation plays a significant role in this possible channel, providing low-energy optical phonons that have a wide band overlap and strong thermal coupling with acoustic phonons. Based on the discovery of the "hybrid phonon" modes due to the existence of organic cation, acoustic phonon can be facilitated to up-convert optical phonon before dissipating the local lattice heat to the surroundings, and the HC relaxation can be slowed down.[85] However, this mechanism is argued by the investigation on coherent phonon oscillations,[108] which indicates the contribution of this mechanism to the HC lifetime can only happen in the timescale greater than 10 ps.

Nanostructuring, for example multiple-quantum-well (MQW) structure, can also be beneficial to enhancing the hot phonon bottleneck effect.[10] The phononic bandgap between LO phonons and acoustic phonons might be opened up because the LO phonons might be reflected by the barrier[109-110] or the minigaps in frequency spectrum are formed preferably [111-112].

- *Auger heating*

At high carrier density above 10^{19} cm^{-3}, the HC cooling lifetime in perovskite has been reported to be significantly prolonged up to several hundreds of picoseconds.[89] The credit has been given to Auger heating (non-radiative Auger recombination), where the released energy (≈ bandgap Eg) from electron-hole recombination is transferred to another carrier. The effect is more significant with high carrier density due to the more efficient carrier-carrier scattering.[89] In addition, Auger heating is expected to be more observable in the material with a smaller band gap or with nanostructure due to the quantum confinement effect.[89, 113] Illustration of Auger heating is shown in **Figure 1.10**, in comparison with Auger-type energy transfer where the total energy of the e-h pair is unchanged.

Under low excitation fluence, in the investigations of conventional inorganic semiconductor nanocrystals (NCs), the hot carrier cooling is fast in smaller NCs which is assigned to Auger-type energy transfer, e.g. the excess energy of the hot electron is transferred to heat the cooled hole.[114] However, perovskite NCs have an opposite trend in size-dependence of HC relaxation rate under low pump fluence, as well as the HC lifetime is significantly prolonged compared to conventional NCs.[104] This phenomenon indicates that the Auger-type energy transfer is suppressed in perovskite NCs (intrinsic phonon bottleneck), possibly due to the smaller carrier effective mass, symmetric energy dispersion and other factors.[42]

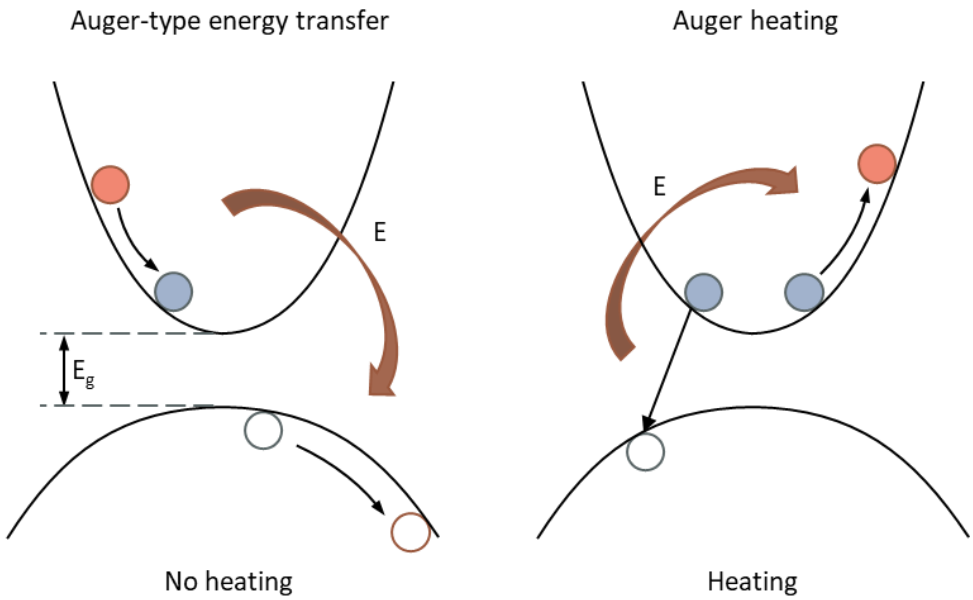

Figure 1.10 *Illustration of Auger-typer energy transfer and Auger heating (Auger recombination). Bandgap E_g is marked.*

- *Polaron formation*

As mentioned before, the influence of the screening effect on HC relaxation is negligible compared to the hot phonon bottleneck effect at moderate or high carrier density. Therefore, the contribution of free carrier screening effect is generally observed at low carrier density (< 10^{17} cm^{-3}), such as polaron formation due to the deformation of PbX_3^- inorganic framework and indirect modulation from organic cation.[115-116]

The genesis of polaron is often ascribed to a paper published by Landau in 1933 for considering the charge carrier moving slowly through an ionic solid.[117] The general use of the term 'polaron' refers to the charge carrier and the altered atomic motions induced by it, as shown in **Figure 1.11a**. It can be divided into strong-coupling polaron and weak-coupling polaron by whether the electronic carriers are self-trapped or not (considered as a perturbation in the weak-coupling approach). In the class of strong-coupling polaron, it can be further divided into large polaron and small polaron by whether the spatial extent of its polarization cloud can extend over several sites or be confined to a single site. In addition, large and small polarons have different transport behavior and temperature dependency of mobility due to the different interaction ranges of carrier-phonon coupling.[118-119] With rising temperature, the mobility of large polaron will decrease and the mobility of small polaron will increase.[118-119] In general, a charge carrier in a deformable lattice induces an attractive potential well, where the carrier can be momentarily trapped. Depending on the strength and type of electron-lattice coupling, the time scale and spatial localization of lattice deformation can vary in a wide range.

Two essential driving forces need to be considered for polaron formation: long-range Coulomb potential (V^{LR}) associated with an ionic displacement polarization, and short-range deformation potential (V^{SR}) related to the carrier-induced strain.[120] If the former is the only important interaction, the charge carrier can remain 'free' and can travel in the lattice dressed with a phonon cloud. If the latter mechanism dominates, the deformation potential induced by the change in local bonding (e.g., lattice distortion induced due to the existence of carrier), the carrier will be strongly localized within one unit cell. The Coulomb potential can be given as

$$V^{LR}(\boldsymbol{r}) = -\left[\frac{1}{\varepsilon_r(\infty)} - \frac{1}{\varepsilon_r(0)}\right]\frac{e^2}{|\boldsymbol{r}|\varepsilon_0}\,, \tag{1.5}$$

where **r** is the vector between an electron and an ionic site. In the case of perovskite, with the large difference between static and optical dielectric constants $\varepsilon_r(0) \gg \varepsilon_r(\infty)$,[121] the Coulomb potential might play an important role in hybrid perovskite for forming large polaron.

Polaron formation is proposed as a possible reason for slow carrier recombination and modest carrier mobility in perovskite, since the two oppositely charged polarons need to remove their "protective shield" for recombination.[64] As an outcome, the interaction between carriers, or with defects or LO phonons, is screened with weakened scattering strength. Many researchers suggest the 'large polaron' is

formed in hybrid perovskite,[74, 116] as shown in **Figure 1.11b**, which is likely to be formed in three-dimensional polar or ionic medium when the self-trapped carriers interact with the displaceable ions mainly via long-range (Fröhlich) interaction.[119] The 'large' in the term stands for the polaron size, meaning the moderate lattice deformation extending over several unit cells. The self-trapping timescale is extremely short (on the order of 100 fs) for large polaron, and therefore large polaron is sometimes expressed as an increase in the effective mass of the carrier.

Various investigations have been conducted in exploring the reason for polaron formation.[122-125] Is it related to the disorder and rotational degrees of freedom of organic cations or originating from macroscopic polarization induced by ion displacement? The predominant reason for polaron formation generally is the deformation of inorganic sublattice, with indirect contribution from organic cations.[116, 126] It is also suggested in some references, that the dipolar fluctuations due to anharmonicity of the halide displacement have a more significant impact on carrier mobility than due to organic cations.[127-128] The latter might participate indirectly.[129] However, the type of cation can affect the polaron formation time,[64, 130] for e.g., 0.3 ps for mixed-cation lead halide perovskite $MAPbBr_3$ and 0.7 ps for all-inorganic perovskite $CsPbBr_3$.[116] Large polaron is formed mainly due to the deformation of PbX_3^- sublattice, while the motions of organic cations coupled to the inorganic cage are responsible for the faster formation rate in hybrid perovskite compared to all-inorganic perovskite. Dynamic disorder (orientation) of molecules produces a random potential on inorganic sublattice, besides indirectly participating in polaron formation,[131] it can modulate electronic properties and suppress the electron-hole recombination since they are spatially localized at different locations.[123, 132-134] Theoretical and experimental results show that the charge carriers are stabilized and localized in the hybrid perovskite on the order of 0.1 ps,[135-137] with a polarization cloud spanning many unit cells.[135, 138]

In addition to the size of polaron and reasons for polaron formation, the lattice response under injection of a hot electron or hole is different.[123] This may be due to a different sensitivity of the valence band and conduction band in response to vibrations of inorganic sublattice.[116]

In the consideration of large polaron in perovskite, as self-trapped carriers with surrounding atoms, it is suggested by some researchers that the ability of self-trapping tends to be diminished with increasing carrier density, since they compete to displace the same atoms.[139-141] The phenomenon was labeled as 'polaron overlap', and more investigations are needed to clear its relation with hot phonon bottleneck effect.[142]

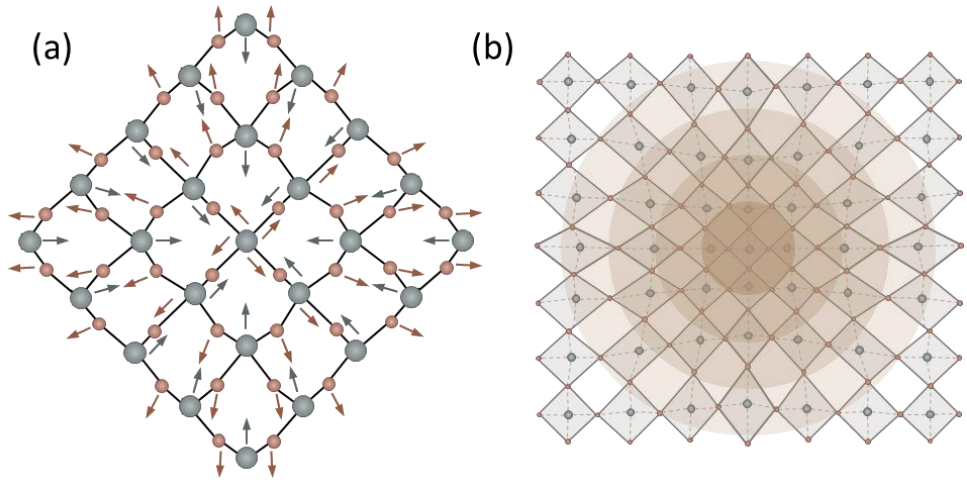

.

Figure 1.11 *Schametics of polaron. (a) Illustrations of polaron formation, include the charge carrier and the altered atomic motion induced by it, and (b) a schematic of large polaron in perovskite.*

2 Experimental Methods

Time-resolved spectroscopies enable the investigations of temporal changes inside the material. Alike using fast shutter cameras for capturing the motion of a horse in the 19th century, by applying ultrafast laser pulses and detectors with high temporal resolution, the generation and relaxation of transient species in ultrafast timescale can be recorded. This chapter mainly discusses time-resolved fluorescence spectroscopy, transient absorption spectroscopy, and time-resolved two-photon photoemission spectroscopy. Different kinds of ultrafast spectroscopies aim at collecting diverse information, more comprehensive information can be obtained through combination of techniques.

2.1 Time-Correlated Single Photon Counting

Time correlated single photon counting (TCSPC) setup is a useful tool for studying fluorescence decay in the time domain, with the time resolution typically in the range of picoseconds to nanoseconds. The detection range can be further extended to microseconds by employing an external trigger to synchronize the laser. After a pulse of light (excitation), the photons emitted from the fluorescent sample will be collected as a function of time. Based on the analysis of temporal evolution of the de-excitation behavior of the excited sample, important information, e.g. fluorescence lifetime, can be evaluated.

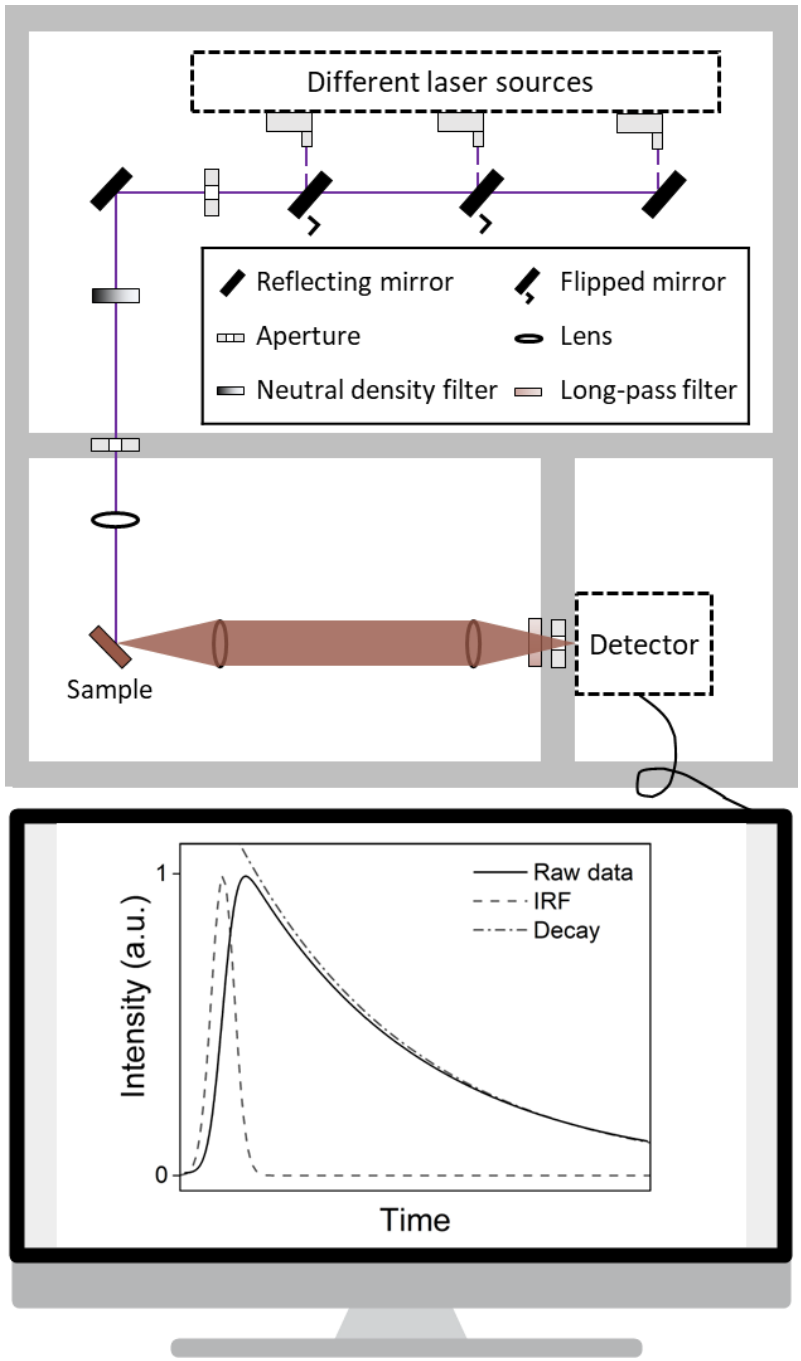

Figure 2.1 *Illustration of time-correlated single photon counting setup.*

The scheme of the TCSPC setup is shown in **Figure 2.1**. Several picosecond pulsed sources (laser diodes, LDH-series, PicoQuant) are used for excitation, with an adjustable repetition rate of up to 80 MHz and a pulse duration of 20 ps. The excitation pulse is directed onto the sample typically via a neutral density filter, for not only attenuating the laser pulse (preventing sample damage) but also suppressing false triggers from stray light on the detector. The single photon avalanche diode (SPAD, PicoQuant) is used as a detector with a timing resolution as short as 50 ps. The picosecond diode laser driver (Sepia II, PicoQuant) and TCSPC module & multichannel picosecond event timer (HydraHarp 400, PicoQuant) are used for controlling the laser and recording data. To characterize the overall timing resolution of the setup, the attenuated scattering of water is measured with the cutoff filter removed (generally long-pass filter) as the instrument response function (IRF) of setup, which contains contributions from the laser, detector, optics and electronics. The full width at half maximum (FWHM) of IRF is around 300 ps, when using a 375 nm laser source with a repetition rate set as 20 MHz. The observed decay profile is a convolution of the intrinsic decay with IRF. Therefore, the influence of IRF needs to be considered cautiously during measurements, especially when the fluorescence lifetime of the sample is close to the timing resolution. The light is attenuated so that only one photon can be received by the detector per excitation cycle to guarantee that the histogram of photon arrivals can represent the PL decay dynamic of the sample.

The principle of TCSPC, as shown in **Figure 2.2**, is detecting the single photon events (one emitted photon per excitation pulse) and their arrival time with respect to the excitation. The arrival time is determined based on signals from the excitation pulse (start time) and from the emission from the sample (stop time). Once an emitted photon is detected, the detector will stop collecting the rest of the photons. By employing the pulsed laser with a high repetition rate, the collection process is efficiently repeated many times to obtain a well-resolved histogram of photon distribution as a function of time. Choosing a high repetition rate can help minimize the pile-up effects in TCSPC measurements (emitted photons lost at a high photon count rate) but can also cause trouble when the sample has a fluorescence lifetime longer than (or equal to) the pulse period.

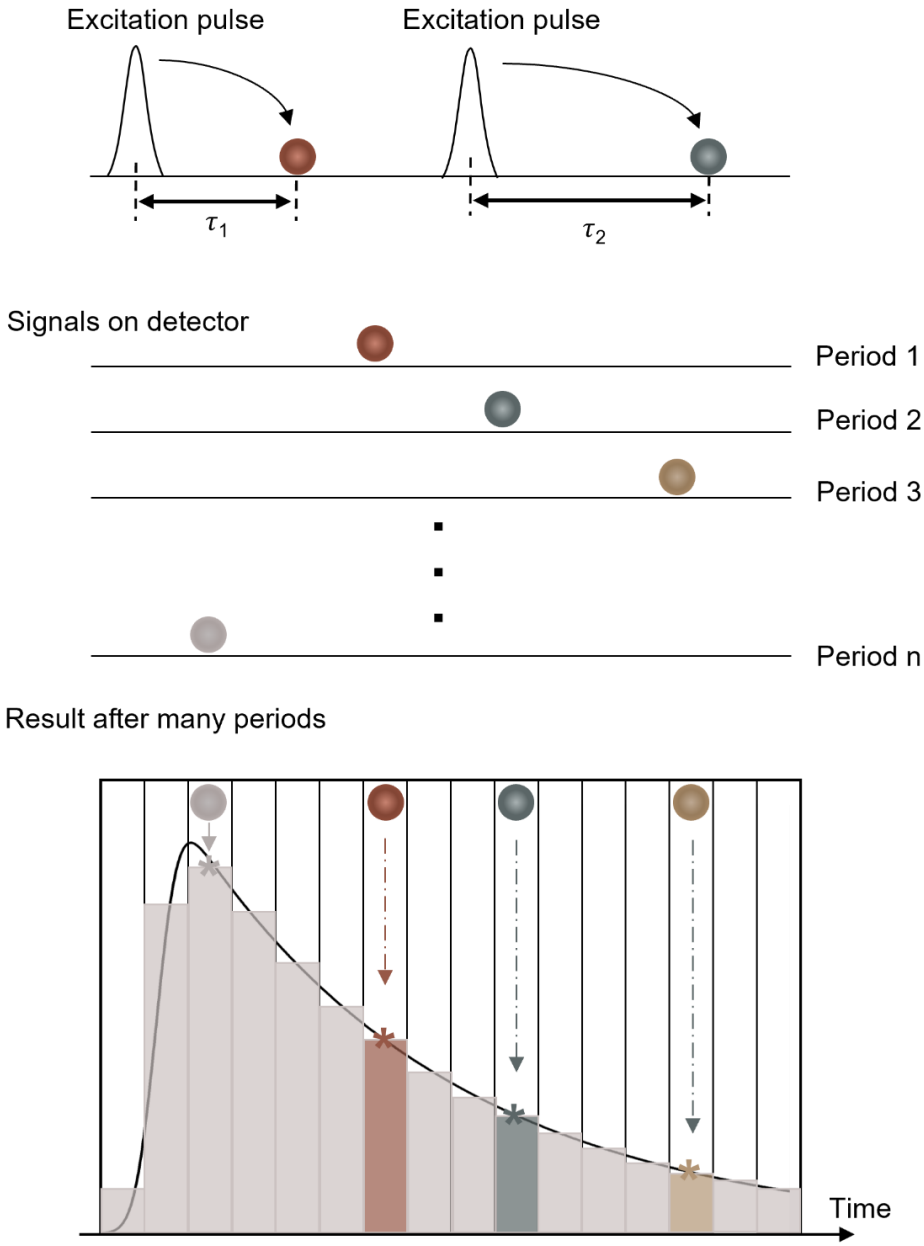

Figure 2.2 *The principle of time-correlated single photon counting.The balls with different colors represent photons detected at different detection periods.*

2.2 Transient Absorption Spectroscopy

Transient absorption spectroscopy (TA) is a powerful technique for investigating light-matter interaction in ultrafast timescales. The pump-probe configuration enables it to detect the change in material absorption as a function of wavelength and delay time, and the related spectrum and kinetics of transient species can be resolved after analysis. The TA spectrogram (ΔA) is calculated as the absorption spectrum of material under excitation (excited state) minus the absorption spectrum of material without excitation (ground state). Therefore, the information related to non-emissive states can also be accessed, unlike the case with time-resolved fluorescence spectroscopy.

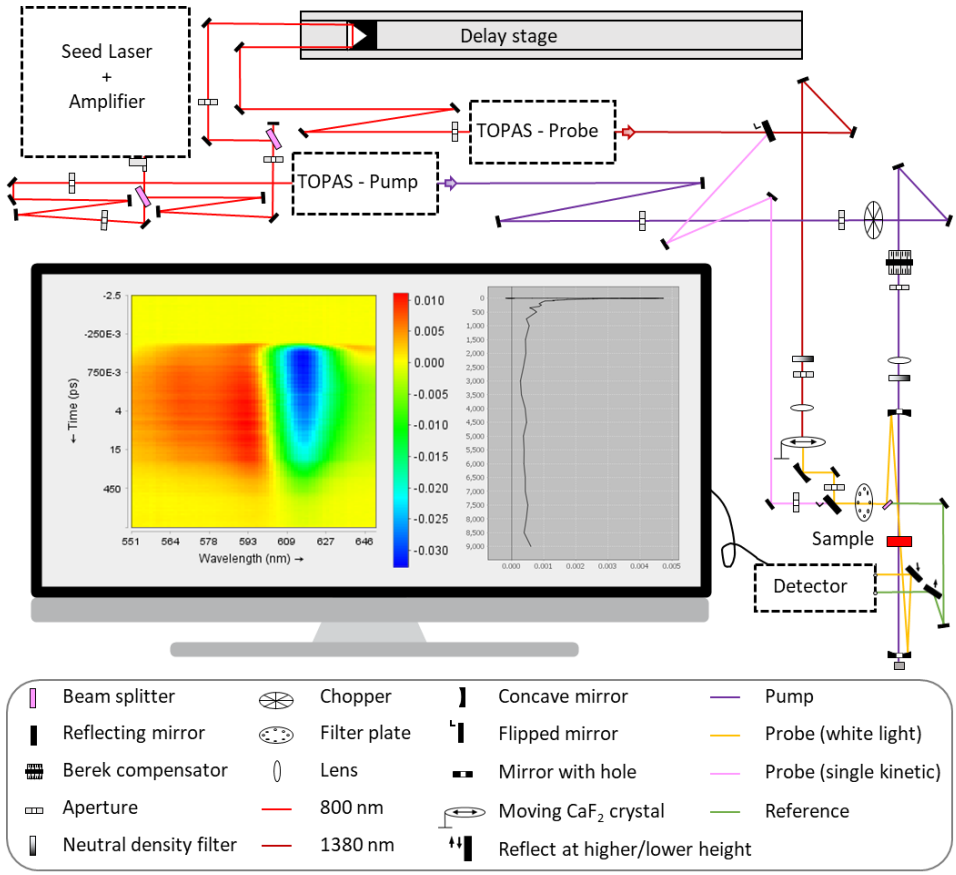

Figure 2.3 *Illustration of transient absorption spectroscopy setup.*

The scheme of TA spectroscopy is shown in **Figure 2.3**. The seed laser (femtosecond oscillator Mai Tai from Spectra Physics) is injected into the regenerative amplifier (Spitfire XP Pro, Spectra Physics) for producing a

fundamental beam with 800 nm wavelength, 1kHz repetition rate, 6 mJ/pulse, and 80 fs pulse duration. The fundamental beam is incident on the beam splitter for generating pump and probe beams. The single-wavelength pump beam can be obtained from the fundamental beam via second harmonic generation (400 nm) on a beta barium borate (BBO) crystal or via an optical parametric amplifier (TOPAS-C, Light Conversion). The probe beam can be single-wavelength (for single kinetic measurements) or broadband white light by sending the near-infrared beam (adjusted by TOPAS) through a CaF_2 crystal. The CaF_2 crystal is mounted on a computer-controlled motorized translation stage to prevent thermal damage. The switch between pump-on and pump-off status in TA measurement is achieved by chopper, and the variation in delay time is controlled by the delay stage (up to 9 ns). The Berek compensator is placed in the light path of the pump beam to set the polarization between the pump and probe beams to be the magic angle (54.7°). For single kinetic measurements, the photodiode is used as a detector. For spectral measurements, the prism and photodiode array is used in the detector.

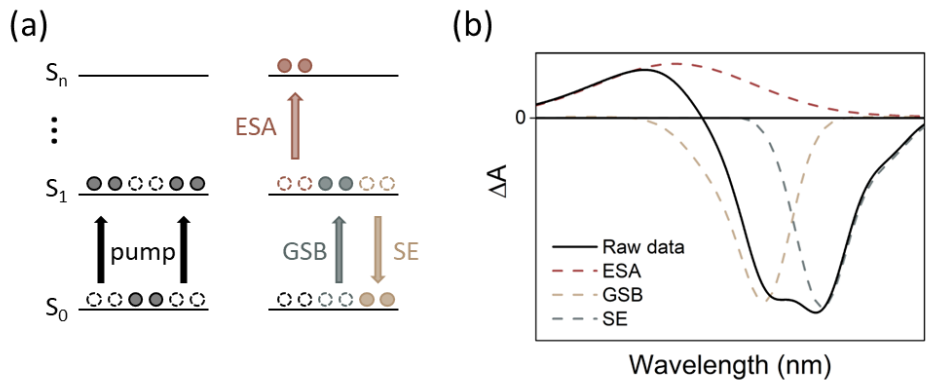

Figure 2.4 *Schematic of contributions in the transient absorption spectrum. Schematic of (a) transitions and (b) example spectra related to excited-state absorption (dash-dot line), ground-state bleach (dash line) and stimulated emission (dot line). The influence of the probe beam on the population of excited state S_1 is exaggerated for a clear illustration. The raw data (solid line) represents the sum of three contributions.*

Three main contributions to the TA spectrum are ground-state bleach (GSB), stimulated emission (SE), and excited-state absorption (ESA), as shown in **Figure 2.4**. The measured TA spectra are the superposition of all contributions. Due to photoexcitation, species are partially excited to excited state S_1, and the population of species at ground state S_0 is decreased compared to the pump-off status. Therefore, a negative signal (GSB) in the TA spectra appeared in the related wavelength region (ground state absorption). By absorbing the probe beam, the excited species at S_1 state can be further excited to a higher excited state S_n and a positive signal (ESA) appears due to the occurrence of absorption of the probe beam in a related wavelength window. Apart from absorption, the excited species at S_1 are not stable

and the probe beam might induce SE, resulting in the transition of excited species from excited state S_1 to ground state S_0. The photon generated from SE follows the direction of the probe beam and results in increased light intensity on the detector, corresponding to a negative signal in TA spectra (ΔA) in the related wavelength range (fluorescence spectrum).[143]

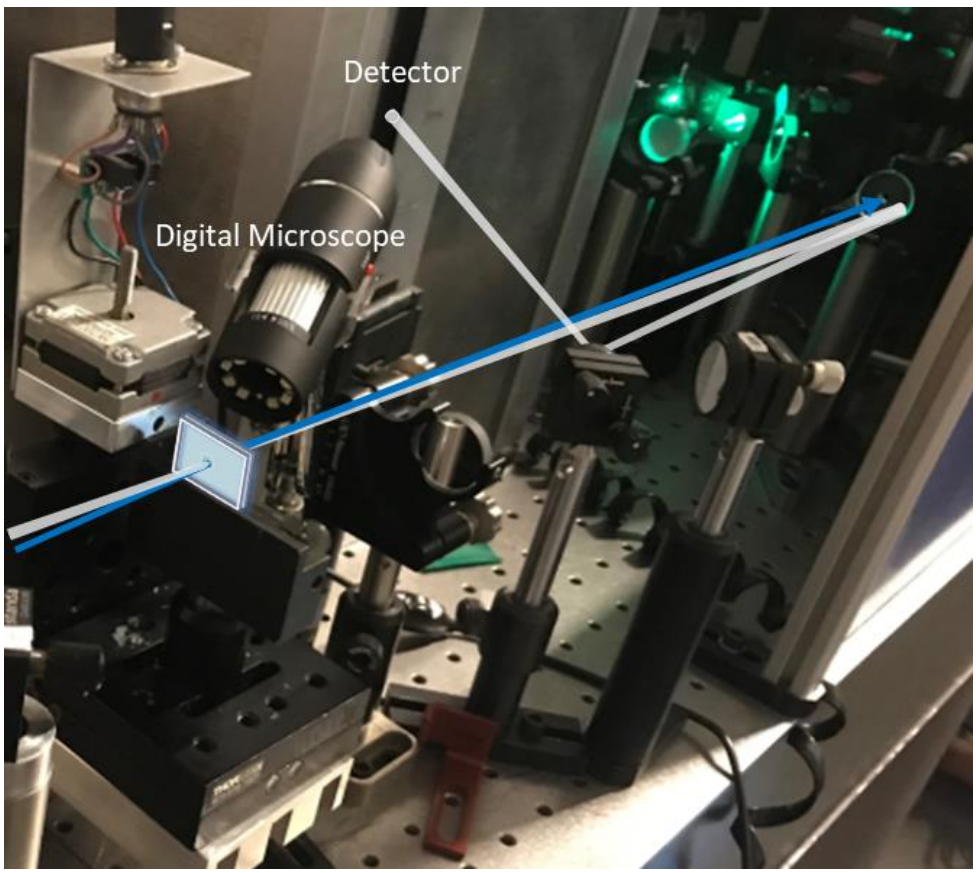

Figure 2.5 *Schematic of in-situ transient absorption measurements. The blue and white lines represent the pump and probe beams, respectively.*

A flake with a size of around a hundred micrometers can be located and in-situ measured with the assistance of a commercial digital microscope embedded in TA spectroscopy, as shown in **Figure 2.5**. The flake is selected under an optical microscope and the picture including the surroundings is taken to mark the location, as shown in **Figure 2.6a**. Then based on the pattern of surrounding bulky crystals and relative distances, the location of the target flake can be determined and the overlapping of beams on the sample can be confirmed, as shown in **Figure 2.6b** and **Figure 2.6c**.

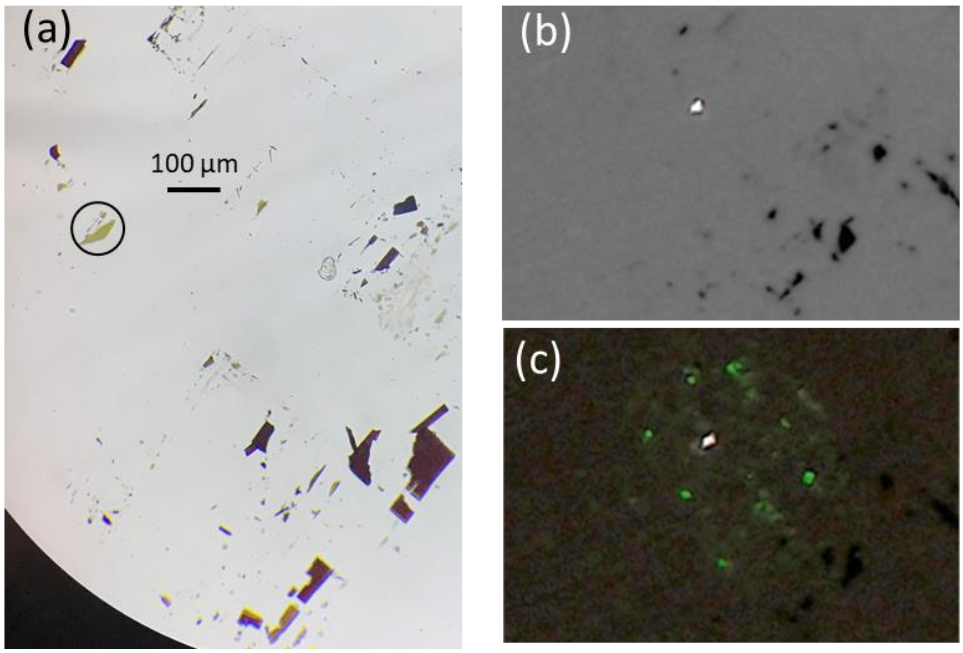

Figure 2.6 *Location of the target flake. (a) Optical microscope image of the flake and surroundings as marks. Digital microscope image of the flake (b) under probe beam and (c) under both probe and pump beams. In this figure, the pump is 560 nm and the probe is white light. The contrast of figures is adjusted for clearer observation.*

2.3 Time-Resolved Two-Photon Photoemission Spectroscopy

The time-resolved two-photon photoemission (tr-2PPE) spectrum can be obtained from (laser-based) time- and angle-resolved photoelectron spectroscopy (tr-ARPES) with the momentum distribution integrated. The configuration is also pump-probe, but unlike transient absorption, the probe used here has higher energy to excite electrons from the conduction band to the vacuum. The photo-emitted electrons with different kinetic energies are collected and analyzed in an electron analyzer under different time delays, and therefore the temporal evolution of the distribution of photoexcited electrons in the conduction band (by pump) can be directly visualized.

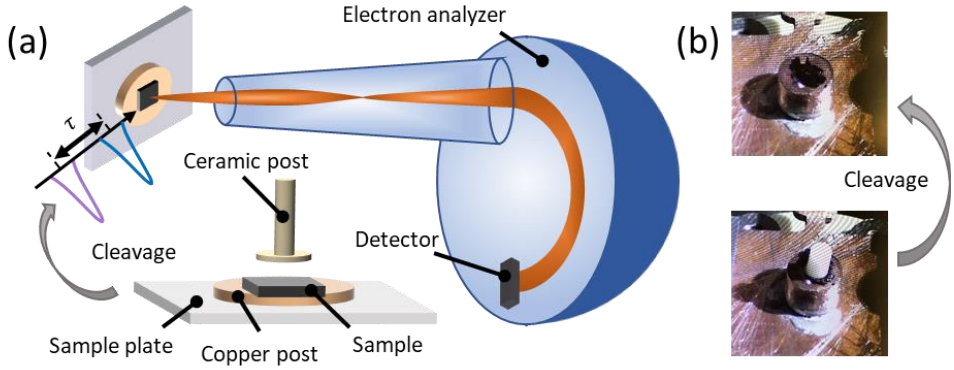

Figure 2.7 *Schematic of time-resolved two-photon photoemission spectroscopy. (a) Illustration of time-resolved two-photon photoemission setup. (b) Images of sample on sample holder before and after cleavage.*

The tr-2PPE setup is shown in **Figure 2.7a**. A Ti:Sapphire system (RegA, Coherent) is used to generate a fundamental beam with an energy of 1.55 eV (800 nm), a repetition rate of 250 kHz and an intensity of 6 μJ/pulse. A beam splitter is used in the fundamental light path for obtaining pump and probe beams. The fundamental beam is incident on a BBO crystal for generating a 3.1 eV (400 nm) pump beam via second harmonic generation. The probe beam is 4.65 eV or 6.2 eV via third and fourth harmonic generation respectively. The pump and probe beams are spatially overlapped on the sample. A hemispherical electron analyzer (Phoibos 150, Specs) is used for collecting and recording the temporal population of photo-emitted electrons as a function of kinetic energy and angle. Note that the distribution on electron emission angles is integrated for tr-2PPE spectroscopy. A delay stage is used to control the time delay between the pump and probe beams. The temporal resolution of the setup is around 100 fs and the energy resolution is around 50 meV. Due to the mean free path of photoelectrons, the setup has a high surface sensitivity as few nanometers where the unscattered photoelectrons come mostly from.

A clean and atomically flat surface is needed for measurements, and thus a cleavage is typically required, as shown in **Figure 2.7b**. Two sides of the crystal are glued on the copper post and ceramic post respectively with electrically conductive adhesives (e.g. silver epoxy). Then the whole sample is coated with graphite for avoiding the charging effect during measurements. After loading the sample holder into the preparation chamber (high vacuum environment), the ceramic post is knocked down by a wobble stick for obtaining a fresh and flat surface. This method is practically useful on a layered material since the Van der Waals force between the interlayers is weak. A commercial microscope (Bresser) is equipped to confirm the sample preparation, and the sample can be further transferred to the main chamber (ultra-high vacuum environment) for measurements.

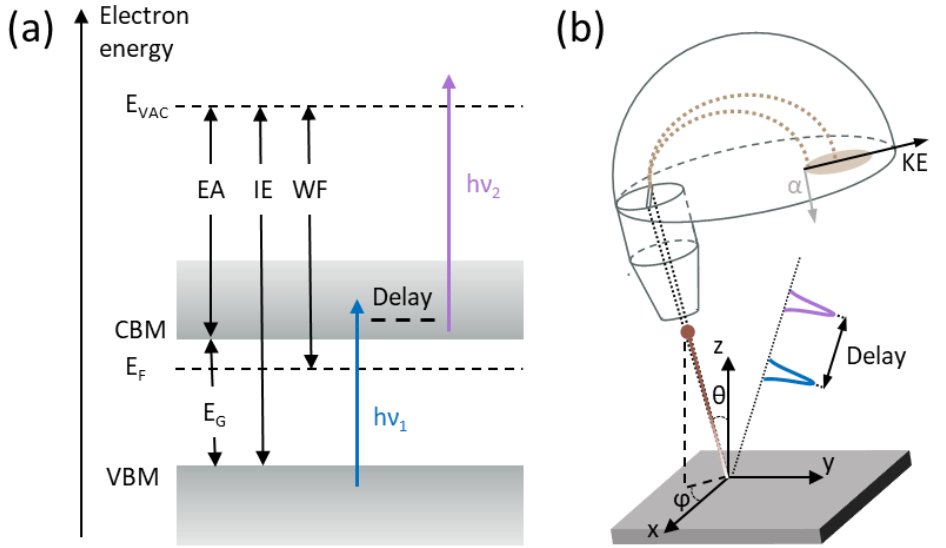

Figure 2.8 *Principle of time-resolved two-photon photoemission spectroscopy (tr-2PPE). (a) Energy diagram of a semiconductor and transitions due to pump and probe beams. (b) Experimental geometry for tr-2PPE where the angle-related distribution from time- and angle-resolved photoelectron spectrogram is integrated. Vacuum level E_{VAC}, conduction band minimum CBM, valence band maximum VBM, Fermi level E_F, electron affinity EA, energy gap E_G, ionization energy IE, work function WF, polar angle θ and azimuthal angle ϕ of photoemission direction, momentum α and kinetic energy KE are marked. The blue line represents the pump beam and the purple line represents the probe beam.*

Electrons at the material surface are naturally prevented to escape to the vacuum level (E_{VAC}), where an electron is 'few nanometers' outside the material surface.[144] According to the photoelectric effect, incident light with minimum frequency (energy) is required for electrons to start emitting from a metal surface. As shown in the energy diagram of a semiconductor (**Figure 2.8a**), the work function (WF = $E_{VAC} - E_F$) represents the minimum energy needed to remove an electron from the Fermi level (E_F) to the outside of surface. The local vacuum level, as well as the work function, is strongly dependent on the nature of surface. For example, surface conditions (contamination or surface reactions) can commonly induce changes on the order of 1 eV on work function, due to the formation of surface electric dipoles. Note, from another perspective, it emphasizes the surface sensitivity of photoemission spectroscopy.

When the sample is irradiated by one beam with photon energy exceeding the work function, the rest of the energy will contribute to the kinetic energy of photoelectron, apart from overcoming the atomic bonding. Due to energy conservation, the kinetic energy E_{kin} of photoelectron emitted from an energy level that is below Fermi level with binding energy E_B can be calculated as:

$$E_{kin} = h\nu - |E_B| - \phi_{sample}\,, \tag{2.1}$$

where ϕ_{sample} is the work function of sample and hν is the photon energy.[145]
While in the case of two-photon photoemission spectroscopy (our measurements), the pump beam cannot induce direct photoemission but excite an electron into an intermediate state (i.e. in the conduction band). After a certain delay, the excited electron is further pushed by the probe beam to a final state above the vacuum level. The calculation of the kinetic energy of photoelectrons can be modified as:

$$E_{kin} = E_{pump} + E_{probe} - |E_B| - \phi_{sample}\,, \qquad (2.2)$$

where the E_{pump} and E_{probe} represent the photon energy of pump and probe beams. Since the kinetic energy can reflect information relating to intermediate states, the temporal evolution of electrons in the conduction band can be evaluated by varying the delay time between pump and probe beams.

3 Results and Discussion

3.1 Electronic Structure and Trap States of Two-Dimensional Perovskite Single Crystal – Paper II

Photovoltaic devices based on metal halide perovskites have been widely investigated over the years due to their advantageous properties. However, the developments suffer from poor structural stability, especially when facing moisture. By inserting the hydrophobic long-chain organic cation between inorganic sublattice, the two-dimensional perovskites can be formed with the formula $(A')_2A_{n-1}B_nX_{3n+1}$, where A' is the organic spacer (e.g. n-butylamine (n-BA^+)), A is the cation inside the inorganic cage (e.g. methylammonium (MA^+), ethylammonium (EA^+), guanidinium (GA^+)), B is the metal cation (e.g. Pb^{2+}), X is the halogen (e.g. I^-) and *n* is the number of octahedral layers. The electronic properties can be adjusted by varying the thickness of the inorganic sublattice. The variable composition and natural multiple-quantum-well structure of two-dimensional (2D) perovskite have drawn significant attention in recent years.

Goldschmidt tolerance factor (τ) is widely used to predict the formation of stable perovskite structure, with a range generally between 0.8 and 1.0.[146] Thus, only a few cations with suitable sizes can be employed in lead halide perovskites, such as MA^+, FA^+ and Cs^+. However, the strict requirement of tolerance factor on 3D perovskites is relaxed in 2D perovskite, and A-site cations with larger sizes can be accommodated by the octahedral cage with greater structural distortions, such as EA^+ and GA^+.

This paper reports the influence of structural distortion on electronic properties and photo-physics by comparing $(n\text{-}BA)_2(MA)_2Pb_3I_{10}$ (BMAPI) and $(n\text{-}BA)_2(EA)_2Pb_3I_{10}$ (BEAPI) single crystals. The molecular compositions of the two target materials are similar, while the A-cation in BEAPI (effective radius r_{EA} = 274 pm) is larger than in BMAPI (effective radius r_{MA} = 217 pm). The stable formation of BEAPI (τ = 1.031) shows the relaxation of the tolerance factor threshold in 2D perovskite and compensation for strain accumulation (increased distortion of the inorganic octahedron) is attributed to separated flexible organic spacers.[147] Based on single-crystal X-ray diffraction (XRD) measurements and calculations in this

work, the magnitude of octahedral distortion in the inner layer and outer layers of BMAPI and BEAPI are compared in detail. Five essential parameters (average lead-halide bond distance <*D*>, distance distortion ζ, tilting distortion Δ, torsional distortion Θ and angle distortion ∑) are used for characterizing lattice distortion, whose values are overall greater for BEAPI than BMAPI. The long-chain spacers work as a 'buffer' to the rigid inorganic sublattice and compression on the organic layer is increased in BEAPI for accommodating larger EA cation in the cage. The compression is confirmed by the shortened layer distance in BEAPI, as shown in **Figure 3.1**. Noteworthy, the organic cations interact with the inorganic unit via N-H···I hydrogen bond, whose average lengths and NH_3 vibration frequency are similar in BMAPI and BEAPI, showing that interaction between the organic cation and inorganic units is unlikely to be the dominating reason for the difference in BMAPI and BEAPI.

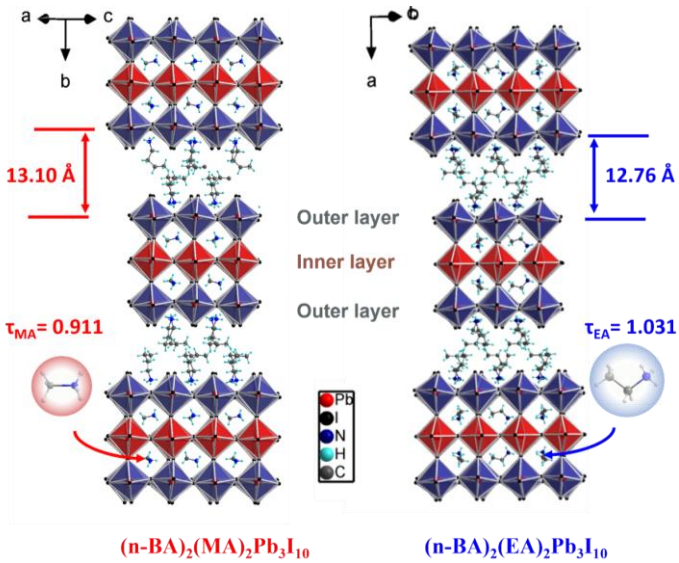

Figure 3.1 *Structure of (n-BA)$_2$(MA)$_2$Pb$_3$I$_{10}$ (BMAPI) and (n-BA)$_2$(EA)$_2$Pb$_3$I$_{10}$ (BEAPI) with marked tolerance factors and layer distances, respectively.*

The change in the lattice structure can affect the electronic properties, especially the electronic band-edges. The optical band gap E_g is determined by steady state absorption measurements and the exciton binding energy is evaluated from the temperature-dependent photoluminescence (PL) measurements. The position of the valence band maximum (VBM) with respect to the Fermi level is determined by X-ray photoelectron spectroscopy (XPS). The energy diagrams of BMAPI and BEAPI are presented in **Figure 3.2a**, showing a ~ 0.2 eV difference in band gap and VBM position, confirmed by the band structure calculated based on density functional

theory (DFT). In the XPS measurements of the core levels, the core-level binding energy of Pb 4*f* core levels in BEAPI is ~ 0.2 eV lower than BMAPI, as shown in **Figure 3.2b**. It suggests the electronic density around Pb atoms is more pronounced in BMAPI than in BEAPI due to the shortened Pb-I bond. In addition, the identical XPS spectra on I 3*d* core level indicate a similar chemical environment around I centers, as shown in **Figure 3.2c**. The electronic structure near the band edges in 2D perovskite is sensitive to the details of the octahedral unit structure, while the organic cation influences the states which are located deep in the valence band or conduction band.[148] The VBM consists of anti-bonding of Pb 6*s* and I 5*p* orbitals, and conduction band minimum (CBM) consists of anti-bonding of Pb 6*p* and I 5*p* orbitals. The existence of lone-pair $6s^2$ electrons and off-center Pb^{2+} distortion suggest the non-spherical electronic distribution around Pb^{2+} atom.[148-150] The shorter average Pb-I bond length in BMAPI than BEAPI suggests stronger interaction of the related orbitals possibly leading to more pronounced charge delocalization due to the hybridization between Pb 6*s* and I 5*p* orbitals. Thus, the energy difference between bonding and anti-bonding states (Pb 6s and I 5p) is enlarged and the energy position of VBM is higher in BMAPI than BEAPI, whilst the CBM is being less affected by the change in Pb-I bond length.

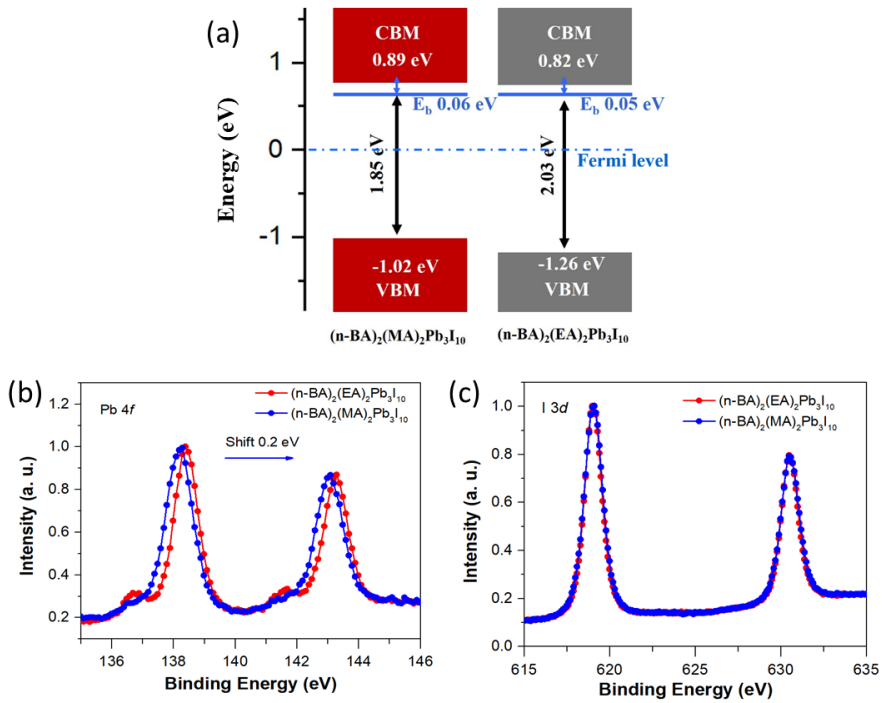

Figure 3.2 *(a) Band alignment of BMAPI and BEAPI. XPS core level emission spectra of (b) Pb 4f doublet and (c) I 3d doublet in BMAPI and BEAPI, respectively.*

As mentioned above, the constraint on the tolerance factor is relaxed in 2D perovskite. To study its impact on the photo-physics properties, we conduct time-resolved photoluminescence (TRPL) measurements on BMAPI and BEAPI. The kinetics can be fitted with three exponential components, including fast (t_1), medium (t_2) and slow (t_3) components. It is shown that the PL lifetime of BMAPI is significantly longer than that of BEAPI, as shown in **Figure 3.3a**. Based on the Saha-Langmuir equation taking into the exciton binding energy and excitation density of the system,[151] the majority of photogenerated species are free carriers, and thus the slow component (t_3) is assigned to intrinsic bimolecular recombination. The other two faster components are often assigned to nonradiative trap-mediated recombination due to various possible mechanisms.[152-153] To further investigate the trap properties, the PL lifetimes under different excitation intensities are measured to monitor the trap-filling effect, which occurs when the lifetime of trap is significantly longer than the time interval between laser pulses. Based on global fitting, the amplitudes (A_1, A_2 and A_3) of the three components at different excitation densities (N_c) are obtained, and the result suggests the existence of two types of traps, that one causes trap filling phenomenon (long lifetime) and the other is immune to trap filling effect (faster depopulation time).[153] The ratio of amplitudes (A_1 / A_2) can be used to determine the fraction of charge carriers being trapped by two different traps and equals the initial ratio of unfilled trap density (n_{uncT1} / n_{uncT2}). Thus, the ratio A_1 / (A_1 + A_2) as a function of excitation density N_c (**Figure 3.3b**) can be fitted to obtain total concentrations of trap 1 and trap 2 (N_{T1} and N_{T2}) and the ratio between trap population and depopulation rates (R_1).

The obtained timescales for each transition are marked in **Figure 3.3c**, and the total trap concentrations of trap 1 in BMAPI and BEAPI are ~ 2.18×10^{16} and ~3.76×10^{16} cm^{-3}, respectively. The higher trap concentration in BEAPI compared to BMAPI might be due to the stronger interfacial lattice distortion when containing the larger EA cation inside the octahedral cage. The faster trapping and detrapping rates in BEAPI also indicate that the traps might be much shallower than in BMAPI. The combination of the shallower traps and higher trap density can be the main reason for the shorter PL lifetime in BEAPI.

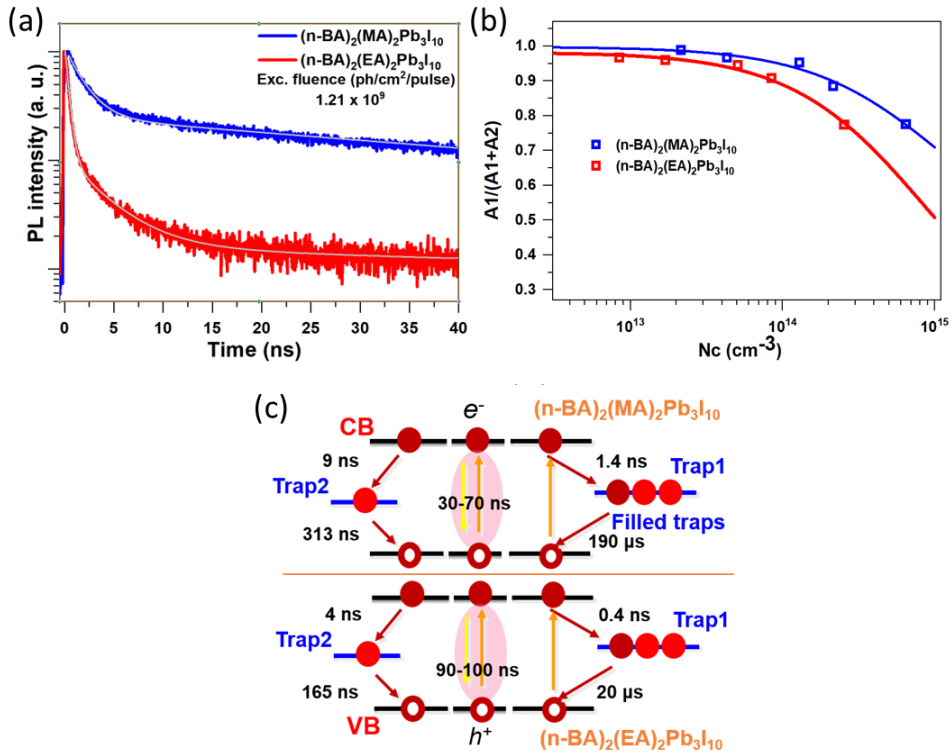

Figure 3.3 *(a) TRPL spectra of BMAPI and BEAPI crystals. (b) Amplitude ratio $A_1/(A_1+A_2)$ as a function of initial charge carrier density Nc for BMAPI and BEAPI, where amplitudes are extracted from multi-exponential fitting on PL decay profile. (c) Schematic of trap-mediated charge carrier recombination in BMAPI and BEAPI, respectively.*

3.2 Free Carriers and Self-trapped Excitons at Different Facets of Two-Dimensional Perovskite Single Crystal – Paper III

By comparing the photophysics of $(n\text{-}BA)_2(MA)_2Pb_3I_{10}$ and $(n\text{-}BA)_2(EA)_2Pb_3I_{10}$ single crystals, we conclude the influence of structural distortion on electronic properties. The stable formation of the latter crystal confirms the relaxed threshold of tolerance factor in 2D perovskite, with flexible spacers contributing to releasing the accumulated strain. In the following study, we further investigate the relationship between local structural distortion, i.e. bulk volume and edge area, on electronic properties.

2D perovskites have great potential in developing photoelectronic applications, such as laser, photodetectors and etc,[50] due to their remarkable electronic properties at room temperature. The properties different from the three-dimensional counterparts are enabled by the natural multiple-quantum-well structure of two-dimensional perovskite.[154] For future applications, the elementary photo excitations need to be understood, for example the origin of the observed broad sub-bandgap emission has been debated.[155-156] One possible scenario is that the low-energy edge states (LES) are observed at the edges of the 2D perovskite single-crystal flakes. Theoretical results suggest that the formation of LES is an evidence of interface strain release at different areas (bulk and edge) in 2D perovskite.[157-158] This means that the different degrees of distortion in bulk volume and edge area will lead to different electronic properties. In addition, in materials with soft lattice and strong electron-phonon interaction, self-trapped excitons (STE) can occur, whose fingerprint is a broad emission spectrum and large Stokes shift.[159-160] The strong electron-phonon coupling leads to elastic distortions in the surrounding lattice and the photogenerated carriers will be 'self-trapped'. The relationship among lattice distortion, STE and LES needs to be revealed by investigating local photogenerated species in bulk and edge areas.

As suggested by theoretical studies,[157] the interface strain in the bulk area is released towards the spacer and the strain accumulation along the direction of the layer is relaxed at the edge area, as shown in **Figure 3.4a**. Thus, the optical measurements are conducted on in-plane facets (IF) and facet perpendicular to the octahedral layer (PF) for investigating charge dynamics in bulk and edge areas, respectively. Since the spacer plays a significant role in strain relaxation, the formation of LES can be modulated by varying spacers. Therefore, in this study perovskite single crystal with similar molecular formula $((A')_2A_{n-1}B_nX_{3n+1}$ where A is MA^+, B is Pb^{2+}, X is Br^{2+} and $n = 2$) but different spacer such as iso-butylamine (iso-BA), n-butylamine (*n*-BA), and n-pentylamine (*n*-PA)) are employed and labeled as iso-BAPB, n-BAPB and n-PAPB, respectively. The structures of the three samples having different layer spacers are shown in **Figure 3.4b-d**. The powder-XRD and calculations indicate that the octahedron of perovskite lattice in *n*-PAPB is the most distorted and has the smallest internal lattice mismatch compared to other 2D perovskites. This observation suggests that the lattice distortion releases the accumulated strain inside the crystal and eases the mismatch in comparison to the lattice of 3D perovskite ($MAPbBr_3$).

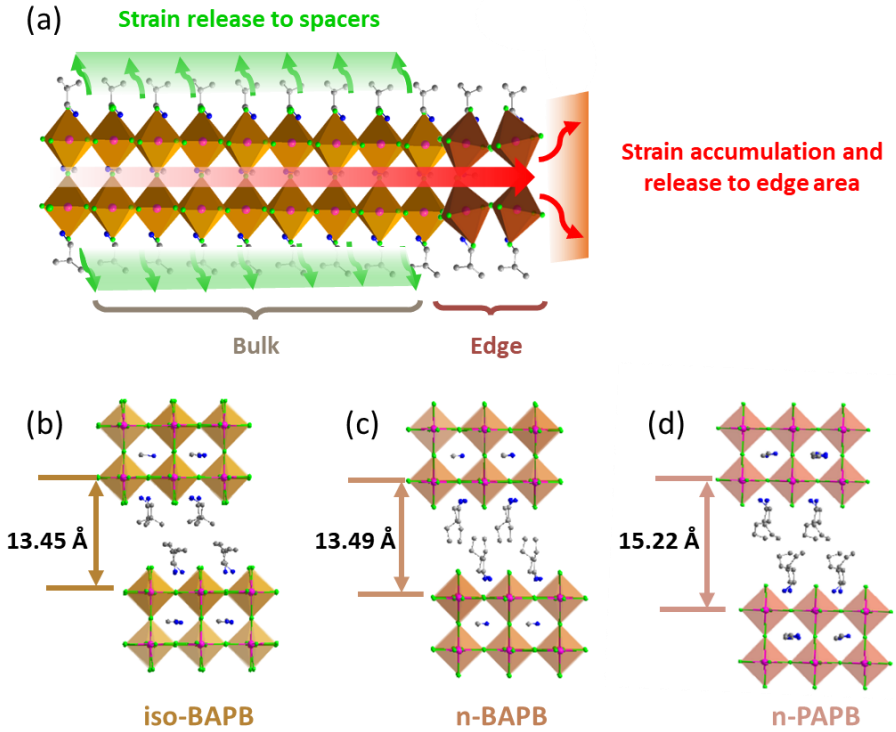

Figure 3.4 *Structure of 2D perovskites. (a) Illustration for strain release in 2D perovskite in bulk and edge areas with different release directions. (b-d) Lattice structures of iso-BAPB, n-BAPB and n-PAPB with different layer distances.*

The 2D perovskite single crystals are grown to be large enough for measuring PL signals from the surface of each targeted facet, as shown in **Figure 3.5a** and **Figure 3.5c**, for investigating the change in the electronic structure induced by local structural distortion. The difference in PL signals from the two facets are observed as different color emissions, as shown in **Figure 3.5b** and **Figure 3.5d**. A red shift of the emission of around 0.4 eV is observed on the PF facet of n-BAPB compared to the IF facet. The large energy shift implies that the octahedral distortion-induced modification on electronic structure around the band edge is not the only reason, which leads to the shift of the PL within 0.2 eV.[161] We propose that the formation of STE is contributing to the red-shifted emission, as the photogenerated carriers are quickly self-trapped into a more stable state compared to the mobile state. To clarify the processes, we performed the temperature-dependent PL measurements on single crystals, and the results suggest that the exciton dissociation and STE formation dominate in IF and PF, respectively. The high-energy PL corresponding to the band edge emission becomes more significant in PF at low temperatures, which can be attributed to the hindered transition from free exciton (FE) to STE, as shown in

Figure 3.5e. With the formation of STEs, the energy of exciton will decrease and the energy difference between before and after STE formation is called self-trapping energy E_{st}. To confirm our explanation of the temperature dependence, the time-resolved photoluminescence spectra are collected for studying the dynamics of photogenerated species, i.e. STEs which are usually responsible for the red-shifted emission.

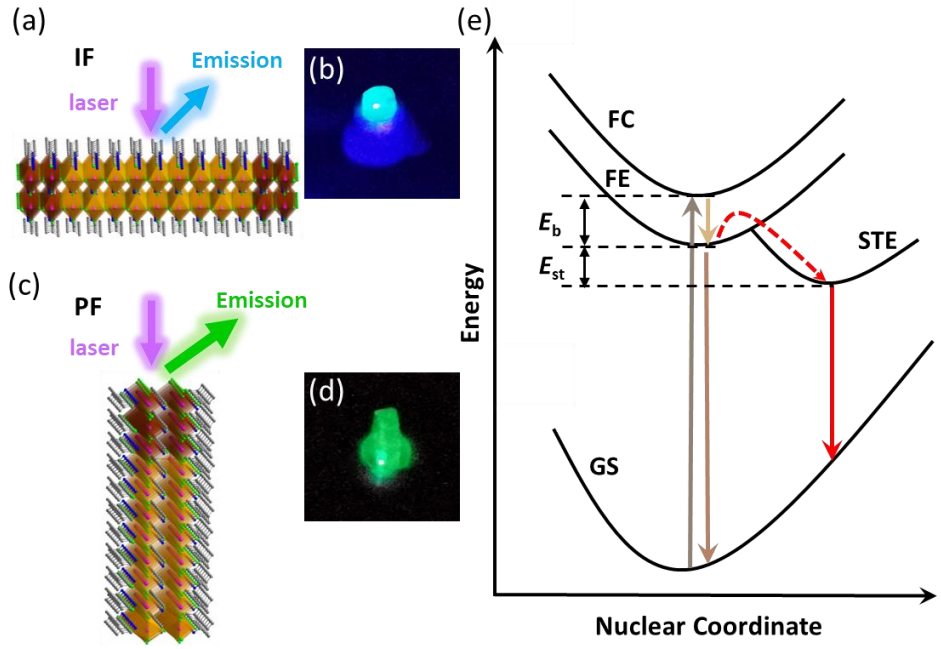

Figure 3.5 *Charge carrier dynamics at in-plane facet (IF) and facet perpendicular to octahedral layer (PF). Illustration of stead-state PL measurements on (a) IF facets and (c) PF facets, and picture of n-BAPB single crystal under laser excitation with (b) blue emission and (d) green emission. (e) Illustration of energy level structure of STE. Free exciton state FE, free carrier state FC, ground state GS, self-trapped exciton state, exciton binding energy E_b and self-trapping energy E_{st} are marked.*

At the IF of *n*-BAPB, the PL lifetime increases with excitation density, as shown in **Figure 3.6a**. The phenomenon can be attributed to the trap filling effect which is widely observed in perovskite single crystals,[151, 153] and the trap density is estimated to be 2.9×10^{16} cm^{-3}. The observation is evidence that the majority of the photogenerated species in IF are free carriers, which is further confirmed by modeling based on the Saha-Langmuir equation. On the contrary, the PL lifetime decreases with increasing excitation density in PF of *n*-BAPB as shown in **Figure 3.6b**, suggesting the existence of another recombination process. In the picture of

STE formation, the greater lattice distortion in PF leads to small polaron formation as self-trapping.[162] The distance between the traps obtained from the trap density is 32 nm. From this, we conclude that it is hard to capture the STE by the trap states at PF under low excitation density because of the relatively long mean distance between traps and the reduced mobility due to self-trapping. Thus, the dominating depopulation pathway of photoexcitations under low excitation fluence is the radiative recombination of STEs, as shown in **Figure 3.6c**. However, the motion of STEs is enhanced with increasing excitation density, illustrated in **Figure 3.6d**, confirmed by the decreased relative PL quantum yield (QY). This could be explained by the decreased stability of STEs[163] or the increased mobility of collective polaron behavior[164].

In conclusion, by investigating the PL dynamics at two different facets of the 2D perovskite single crystals with different spacing cations, we have obtained a better understanding of the relationship between the local structure and the pathways of photogenerated species.

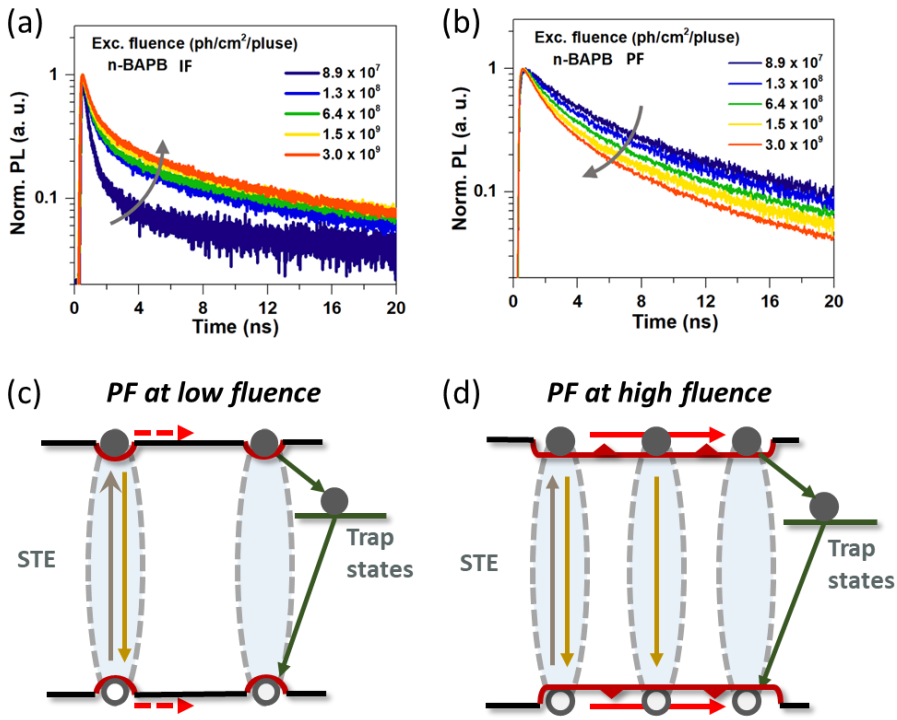

Figure 3.6 *Schematic of STE in 2D perovskite single crystal. Time-resolved photoluminescence measurements on (a) IF facet and (b) PF facet. Schematics of charge carrier recombination processes in PF under (c) low excitation density and (d) high excitation density.*

3.3 Local Electronic Properties of Two-Dimensional Perovskite Single Crystal – Paper V

In the above-discussed papers, the relationship between structural distortion and electronic properties is investigated by comparing photophysics in samples with different compositions or different facets of one single crystal. In the following study, we provide additional arguments by directly characterizing the electronic structure at different areas of samples by mapping the photoelectrons from Pb 5*d* and I 4*d* core levels.

The two-dimensional (2D) lead halide perovskites have drawn great attention due to their unique properties and natural quantum well structure with a formula as $(A')_2A_{n-1}B_nX_{3n+1}$, where A' is the organic spacer, A is the cation inside the octahedral cage, B is Pb^{2+}, X is the halogen and *n* is the number of octahedral layers.[165] The photo- and chemical stability of 2D perovskite is significantly improved compared to conventional three-dimensional perovskites.[48] In addition, it is found that the photophysical properties of 2D perovskite correlate with the local structure, e.g., low-energy edge states (LES) are observed at the edge area of single crystal flake, which possibly facilitates exciton dissociation into long-lived charge carriers and improves device performance.[155, 166] The formation of LES has been debated for years and the direct characterization of local electronic structure at the edge and in the bulk area of crystal flake is urgently needed.[157, 167-169]

In this paper, we conducted X-ray photoemission electron microscopy (XPEEM) measurements on exfoliated $(BA)_2(MA)_{n-1}Pb_nI_{3n+1}$ (n = 1, 2, 3) single crystal flakes. Based on the results, we can spatially resolve differences in elementary compositions and electronic structure at edge and bulk areas by mapping the Pb 5*d* and I 4*d* core levels. With varying the *n*-value of 2D perovskites, the relation between lattice distortion and edge states can be studied in detail.

The structure models of 2D perovskites are shown in **Figure 3.7 (a-c)** with sample images in **Figure 3.7 (d-e)**. The high quality of single crystals is confirmed by XRD measurements, and the bulky single crystal is exfoliated several times to flakes for removing potential surface contaminations before measurements. The fresh flakes are transferred on a silicon substrate and the surface of a flake is exfoliated again in the preparation chamber with high vacuum. To confirm that the long-range lattice order remains in the flakes, low-energy electron diffraction (LEED) measurements are performed on three samples and the results are consistent with the theoretical predictions on Pb-Pb distances.

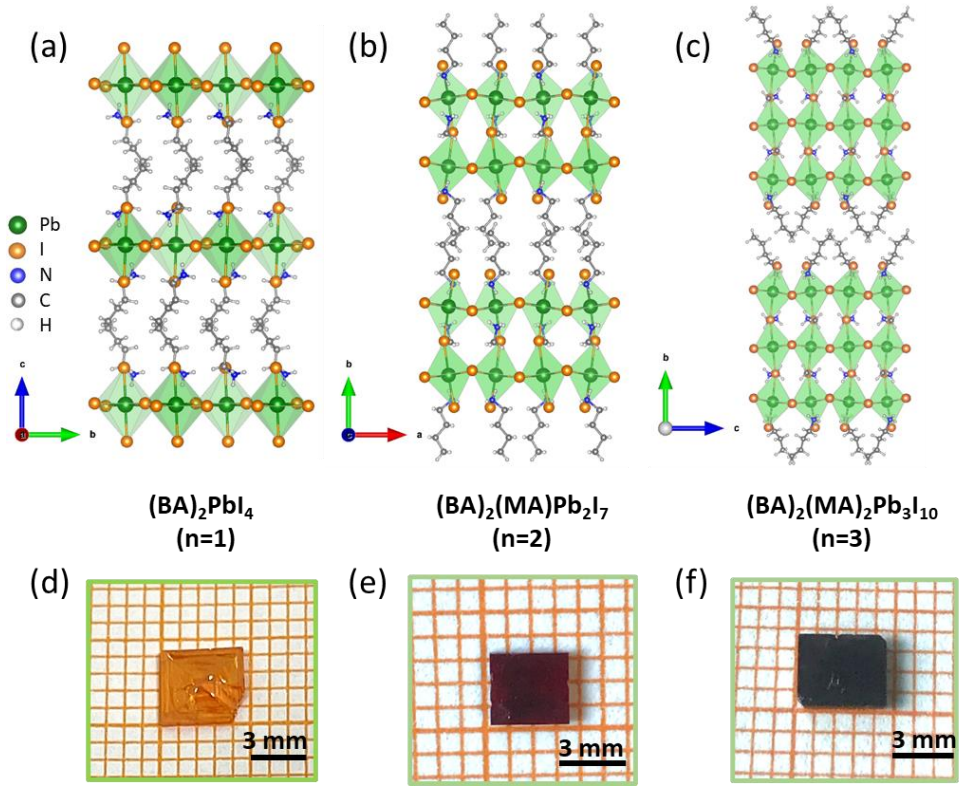

Figure 3.7 *Structures and images of 2D perovskite. (a-c) Schematic of 2D perovskite lattice with different n-value, and (d-f) images of corresponding single crystals.*

The XPEEM measurements on 2D perovskites focus on mapping the core electron emission at the edge and the bulk areas marked as two rectangular zones in **Figure 3.8 (a-c)**. The X-ray source used in XPEEM measurements has a photon energy of 80 eV and the energy resolution of the setup is around 0.2 eV. The results of Pb 5*d* and I 4*d* core level emission are presented in **Figure 3.8 (d-i)** for different 2D perovskites. The Pb 5*d* core level emission at the edge area is blue-shifted (to higher core-level binding energies) compared to bulk areas in all three samples by different amount, i.e. ~ 0.2 eV in $(BA)_2PbI_4$ (n = 1) and $(BA)_2(MA)Pb_2I_7$ (n = 2), and ~1.0 eV in $(BA)_2(MA)_2Pb_3I_{10}$ (n = 3). The shifts of I 4*d* core level emission are negligible (<< 0.2 eV) in all samples. To summarize, the Pb 5d core level emission is blue-shifted at the edge area compared to the bulk area, and the shift is more significant with thicker octahedral layers (n = 3), while the shift of I 4*d* core level emission is negligible and independent of n-value.

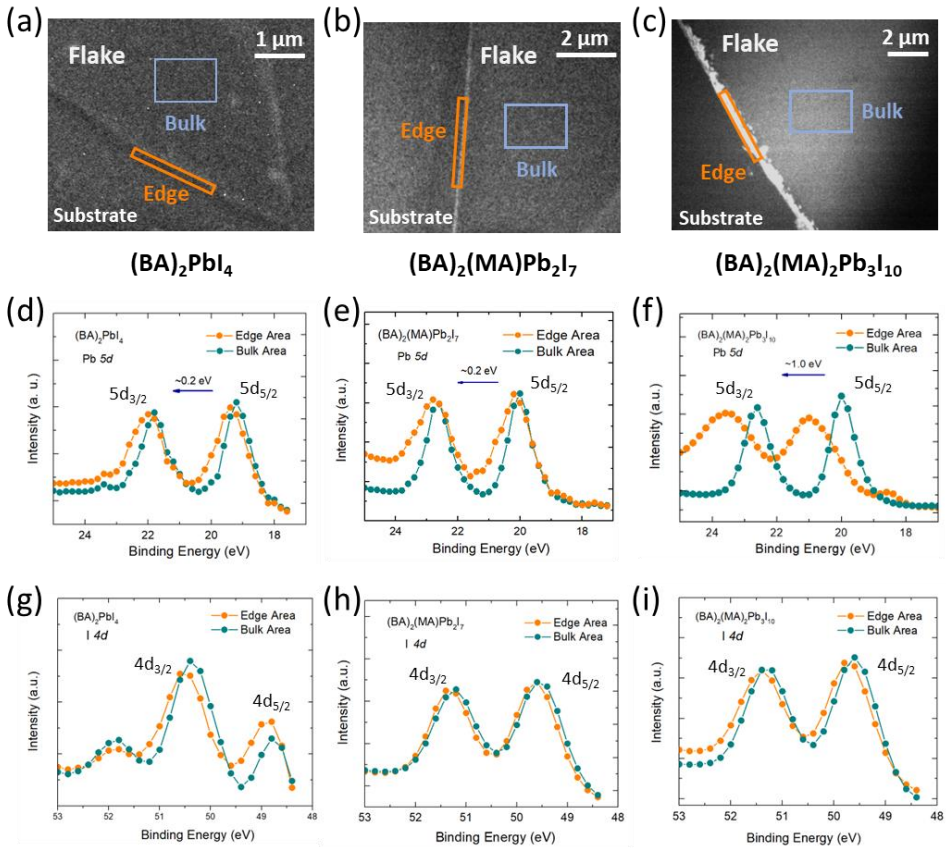

Figure 3.8 *X-ray photoemission electron microscopy (XPEEM) results on 2D perovskites with different n-value. (a-c) XPEEM mapping images of* $(BA)_2(MA)_{n-1}Pb_nI_{3n+1}$ *(n = 1, 2 and 3), corresponding (d-f) Pb 5d and (g-i) I 4d core level emission spectra at edge and bulk areas.*

As for the possible reason for the blue shifts in Pb 5*d* core level emission, the change of chemical composition at the edge state is first ruled out. Considering the Pb atom as an electron donor and the I atom as an electron acceptor via Pb-I bond, an opposite shift in I 4*d* core level emission (compare to Pb 5*d*) should be observed if the ratio between Pb and I is changed due to additional composition.

Since the lattice distortion difference in edge and bulk area has a significant impact on electronic properties, the lattice mismatch theory can be used to explain the asymmetric shifts in core-level emissions.[157] The lattice strain in the octahedral layer can be released in different directions, i.e. perpendicular or parallel to the plane. In the out-of-plane direction (perpendicular to the octahedral layer), the soft and flexible spacers participate in releasing strain. However, in the in-plane direction

(parallel to the octahedral layer), the lattice strain is accumulated at a long distance inside the octahedral layer and released at the edge area. The resulted local surface structural reconstruction at the edge area, as shown in **Figure 3.9a**. Therefore, the edge states are formed and are dependent on the *n*-value. In 2D perovskites with thin octahedral layers, i.e. n = 1 or 2, the accumulation of in-plane lattice strain can be significantly buffered by spacers and hinder the formation of the edge states. As a result, the core level emissions at the edge area and bulk area are more identical. In 2D perovskites with thick octahedral layers, i.e. n = 3 in our study, the surface structural reconstruction may lead to a larger overlap between outer electron orbitals of Pb and I atoms. The Coulomb attraction of the Pb nucleus on electrons at core levels is enhanced and results in higher core-level binding energy in core-level emissions at the edge area than at the bulk area, as shown in **Figure 3.9b**.

On the other hand, the identical I 4*d* core level emission at the edge and bulk areas might be attributed to the contribution of N-H···I hydrogen bonds. The reorganization of charge distribution within the Pb-I metavalent bond is balanced and thus the core level emission from the I atom is independent of *n*-value and local structure distortion.

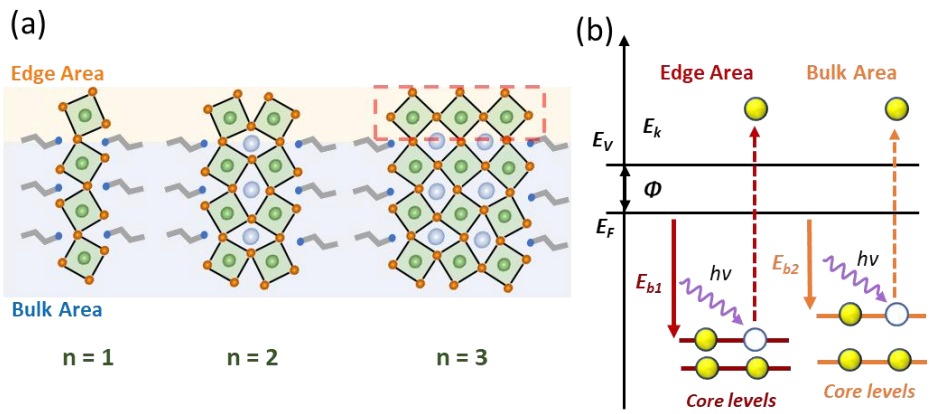

Figure 3.9 *Illustration of core level emission at edge and bulk area. (a) Schematic of local structure at edge and bulk areas for 2D perovskites with different n-value. (b) Energy diagram of electron emission from Pb core levels at edge and bulk areas, with related transitions marked. hv is the energy of excitation, E_k is the kinetic energy of generated electrons, ϕ is the work function, E_v is the vacuum level, E_F is Fermi level, E_{b1} and E_{b2} are the core-level binding energies of target Pb core levels at edge and bulk areas.*

3.4 Hot Carrier Cooling in Two-Dimensional Perovskite Single Crystal – Paper I

The previous studies focus on revealing the electronic properties of 2D perovskites with different compositions or at different areas of single crystal samples. In the following study, we target hot carrier (HC) relaxation processes in 2D perovskites and link the observation to the spatial sensitivity of cooling dynamics across the sample.

Metal halide perovskites have various outstanding properties which make them good candidates for solar cell applications.[18] 2D perovskite, which has a natural multiple-quantum-well structure, [49] improved stability[50, 154] and extended variable compositions compared to 3D perovskites,[58] has drawn interest widely as building blocks for solar cell applications.[170] For solar cells with power conversion efficiency exceeding the Shockley-Queisser limit, a promising concept is hot carrier solar cell (HCSC) with theoretical efficiency reaching 66%.[13] The essential idea of the concept lies in reducing heat loss during device operation, which is the most pronounced loss channel in solar cells. The excess energy released from hot photogenerated carriers is used to heat the "cold" carriers close to the band edge. If the carrier energies can stay high, which corresponds to elevated temperature, long enough for continuous extraction via electrodes significant efficiency improvement can be achieved. For this to work, materials whose photogenerated carriers cool down slowly would be needed.

3D perovskite has drawn increasing attention as a potential material candidate for HCSC applications, e.g. large phononic bandgap between optical and acoustic phonon branches.[89, 104] Klemens decay, the most efficient channel of phonon decay in polar semiconductors, [82] can be hindered if the Two-dimensional perovskite as a promising building block for solar devices, has unique properties that might potentially hinder the hot carrier relaxation and enable hot quasi-equilibrium states with long lifetime. For example, the propagation of acoustic phonons might be hindered due to the existence of soft and long-chain spacers and the hot phonon bottleneck effect may be enhanced due to the multiple-quantum-well (MQW) structure. [10, 171]

On the other hand, extensive researches have been conducted for investigating mechanisms of hot carrier relaxation based on ultrafast spectroscopy, such as transient absorption spectroscopy (TA) and time-resolved photoluminescence spectroscopy. However, standard analysis requires the selective fitting of the high energy tail part of the spectra, which might lead to errors when using different fitting ranges or equations.[172] A technique with which the population and energy

distribution of hot carriers can be directly observed is needed to make a universal comparison among different samples.

All in all, a comprehensive study of 2D perovskite with direct observation of hot carrier distribution, is needed. In this paper, the hot carrier relaxation process in exfoliated $(BA)_2(MA)_2Pb_3I_{10}$ single-crystal flakes is investigated by employing transient absorption (TA) spectroscopy and time-resolved two-photon photoemission (TR-2PPE) spectroscopy. Signals from the two techniques provide information about carrier dynamics in surface and bulk areas, which allow us to relate HC relaxation mechanisms to the material properties of 2D perovskite single crystal.

To prevent the influence of moisture and oxygen on sample properties, the single crystal is exfoliated into flakes (diameter around 100 μm and thickness around 100 nm) and capsuled between two quartz plates in the glove box. The TA spectra of 2D perovskite single crystal flake are shown in **Figure 3.10a**, where the sample is photoexcited at 3.1 eV (400 nm) and probed by a white light. Since the TA signal reflects the population of photogenerated carriers in excited states, the carrier temperature (system energy) can be extracted by fitting the high energy tail of ground-state bleaching with the Boltzmann distribution.

$$\frac{\Delta T}{T} = A_1 + A_2 \exp\left(-\frac{E - E_f}{k_B T_C}\right) \tag{3.1}$$

The method has been widely reported in literature. [88, 173] Since the effective masses of electron and hole are similar, the calculated carrier temperature T_c represents the average temperature of the system. The decay of carrier temperature over time after carrier thermalization (~ 0.3 ps) is shown in **Figure 3.10b** and fitted by the single exponential function. The HC lifetime is in the range of a few picoseconds, and the hot carrier relaxation is slowed down with increasing excitation density.

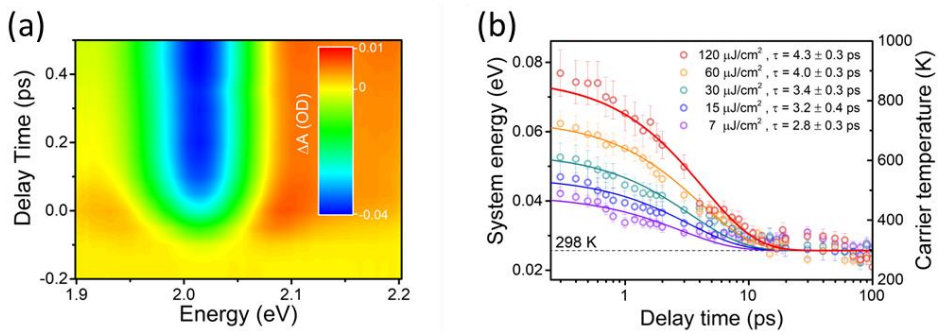

Figure 3.10 *Transient absorption measurements for investigating hot carrier relaxation rate. (a) TA spectrum of 2D perovskite single crystal flake, where the pump is 3.1 eV with the intensity of 30 μJ/cm^2. and the probe is white light. (b) Decay of hot carrier temperature as a function of time delay under different excitation densities.*

By pumping crystal with the same excitation (3.1 eV) but probing it with a middle ultraviolet probe beam, electrons in the conduction band can be further excited to vacuum and collected by the analyzer showing electron distribution along momentum and energy axis. The crystal is cleaved inside the preparation chamber with high vacuum to produce an atomically flat and clean surface, since the TR-2PPE measurements are highly surface-sensitive. The mean escape depth of photoelectrons is around 3 nm,[174] and thus the very surface layer plays a significant role in providing signals, as shown in **Figure 3.11a**. Compared to the case in TA measurements where the whole bulk volume (100 nm thickness) of flake is probed, the TR-2PPE only monitors the hot electron distribution at the surface layer. The spectrogram is presented in **Figure 3.11b** which clearly shows two cooling stages. The average excess energy $E_x(t)$, calculated by integrating the overall excess energy distribution.

$$E_x(t) = \frac{\int E[I(E,t) - I(E,-)]dE}{\int [I(E,t) - I(E,-)]dE} \tag{3.2}$$

The average excess energy can be used to represent the system energy at different time delays as shown in **Figure 3.11c**. Fitting the decay profile of average excess energy with bi-exponential function, two stages of electron relaxation. First a rapid cooling in sub-picosecond timescale takes place, followed by a slower component in few picosecond range.

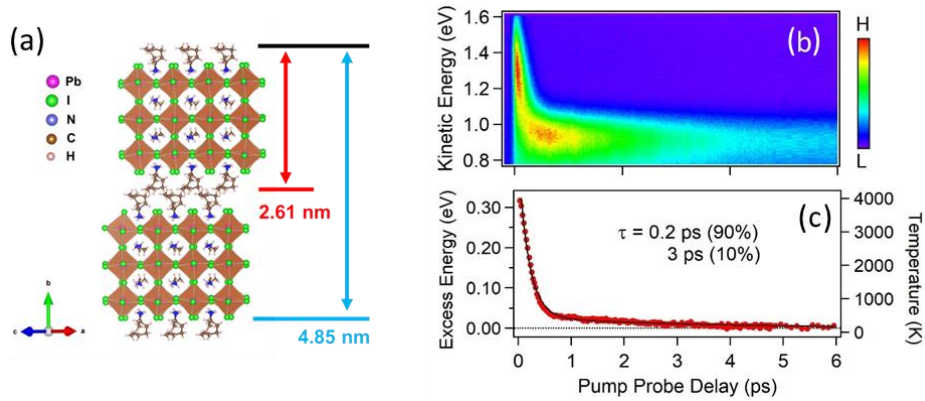

Figure 3.11 *Surface-sensitive time-resolved two-photon photoemission measurements for investigating hot carrier relaxation rate. (a) Schematic of the 2D perovskite structure. (b) TR-2PPE spectrogram of 2D perovskite single crystal flake, where the pump is 3.1 eV with excitation intensity of 100 μJ/cm² and probed is 4.65 eV. (c) Decay of average excess energy of the system as a function of time delay.*

The results from TA and TR-2PPE are summarized in **Figure 3.12a**, where the carrier temperature T_c and average excess energy $E_x(t)$ are converted into system energy for simplifying the comparison. Since the carrier temperature cannot be quantified before carrier thermalization, the initial system energy value from TR-2PPE is adopted as a starting point in TA analysis and the two time constants of HC relaxation are calculated to be ≤ 0.1 ps and 4.3 ps. Two main differences in TA and TR-2PPE results are a faster cooling rate in Stage I and a higher amplitude of Stage II in TA analysis.

The clear observation of two stages in HC relaxation can be attributed to the hot phonon bottleneck. As HCs warm up longitudinal optical (LO) phonons and reach an equilibrium with these phonons, the further cooling of HCs is slowed down and corresponds to the energy flow from the LO phonons to acoustic phonons. Stage I can be assigned to the carrier-LO phonon scattering and Stage II is related to the relaxation of LO phonons to acoustic phonons. The different HC relaxation rate in TA and TR-2PPE in Stage I has several possible reasons. One significant difference between these two techniques is that the signal in TR-2PPE dominantly comes from the surface layer, while the whole bulk volume is probed in the TA measurements. The faster relaxation rate in TA analysis suggests stronger carrier-LO phonon coupling strength or larger density of states of LO phonons in bulk volume. It is reported that the lattice distortions at the surface and in the bulk are different based on the scanning tunneling microscopy investigations,[175] and the carrier-phonon coupling strength can be enhanced due to the strain-accumulated area based on our

previous study[176]. Thus, the relaxed steric hindrance in the surface layer can lead to a weaker carrier-phonon coupling than in bulk volume. In addition, the soft and flexible spacer attached to the surface layer might result in reduced availability of the 'regular phonons' for HCs to couple to and leads to a reduced efficiency of HC relaxation at the surface at Stage I. Another possible reason is that the environmental temperatures in TA (room temperature) and tr-2PPE (135 K) measurements are different, which changes the thermal population of LO phonons and affects the cooling efficiency. However, the spacer modification can change vibrational frequencies,[177] therefore the effect of the environmental temperature on HC relaxation cannot be clearly evaluated due to the uncertain LO phonon energy.[178-179] A further difference between the two experiments is that only hot electrons are probed in tr-2PPE measurements, while both electrons and holes contribute to the signal in TA measurements. The slightly lighter effective mass of electrons than holes can lead to different Fröhlich coupling constant,[180] whilst as a minor influencing factor on HC cooling rate. As for the higher initial carrier temperature of the Stage II in TA analysis, we speculate that the LO phonon density of states is higher at the surface, thus can accommodate more energy and the hot phonon bottleneck effect appears at a lower temperature compared to the bulk area.

Our investigation provides information about spatial-sensitive HC relaxation dynamics in 2D perovskite single crystal by conducting two comprehensive spectroscopic measurements, which may benefit HCSC application when using 2D perovskites as building blocks. In addition, TR-2PPE shows its potential in investigating HC relaxation with direct visualization of relaxation stages.

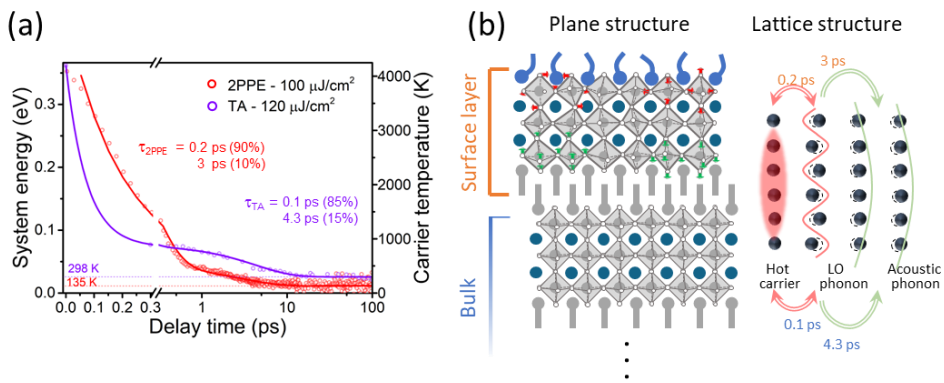

Figure 3.12 *Illustration of the different observed HC decay dynamics from TA and TR-2PPE measurements. (a) Decay dynamics of HC temperature extracted from analysis on TA and TR-2PPE measurements. (b) Schematic of hot carrier relaxation processes in surface and bulk areas.*

3.5 Hot Carrier Cooling in Mn-Doped Inorganic Perovskite Nanocrystals– Paper IV

The previous articles present the characterization of 2D perovskite single crystals, the relation between structure and electronic properties, and the relaxation dynamics of hot carriers in 2D perovskites. In the following study, we investigate the influence of transition metal doping on electronic and phononic properties in 3D perovskite nanocrystals and the resulting modification of hot carrier relaxation dynamics.

The concept of hot carrier solar cells (HCSCs) is established for producing solar cells with efficiency exceeding the Shockley-Queisser limit.[13] The photogenerated carrier with high excess energy relaxes via several processes until reaches equilibrium with the environment. To improve the power conversion efficiency of devices, the hot carriers need to be kept at quasi-equilibrium status for a sufficiently long time so that they can be extracted. Various mechanisms are proposed for slowing down hot carrier relaxation, e.g. hot phonon bottleneck,[88] polaron formation[64] and Auger heating[89]. The origin of mechanisms is highly dependent on material properties and experimental conditions. Investigating hot carrier relaxation in different materials is helpful for establishing general selection criteria of material candidates as HCSC absorbers. In addition, optimizing the HC extraction is required for recycling the released energy from the relaxation of HC towards band edge. One way to achieve the goal is to develop energy-selective contacts to limit the energy range of extracted HC and thus avoid the waste of HC excess energy. However, the perfect energy alignment between the absorber and electrodes is challenging. Another way is adjusting the material composition to alter HC relaxation dynamics and create a long-lived quasi-equilibrium status, while the HC excess energy can be used to reheat cold carriers. The generally involved processes in HC relaxation in polar materials are carrier-carrier scattering, carrier-LO phonon scattering and decay of LO phonon.[89] A material with enhanced carrier-LO phonon interaction and hindered LO phonon decay is desired, since the former interaction is contributing to establishing the mentioned quasi-equilibrium while the last process is dissociating such quasi-equilibrium.

Lead halide perovskite (LHP) is a promising material candidate for HCSC with various appreciated properties, such as efficient HC extraction, long HC lifetime and transportation distance.[37, 104, 181] Furthermore, transition metal doping is found to have a significant impact on the properties of LHP.[182-184] The doping results in long-lived triplet luminescence after charge or energy transfer from host to Mn^{2+}.[185-186] In addition, local structural distortion is induced due to the partial replacement of Pb^{2+} by Mn^{2+}, as shown in **Figure 3.13**, which has a different cation radius. X-

ray absorption (XAS) spectroscopy is used to confirm Mn^{2+} doping in perovskite lattice instead of presenting as Mn^{0} clusters on samples with different doping concentrations.

Since the HC relaxation processes are determined by the electronic structure and phononic structure of the material, it is expected that the Mn^{2+} doping can significantly modulate HC relaxation dynamics and help establish the preferred quasi-equilibrium. Thus, in this work, the HC relaxation dynamics in Mn-doped $CsPbI_3$ nanocrystals (NCs) are investigated in detail by employing transient absorption (TA) spectroscopy on samples with different doping concentrations.

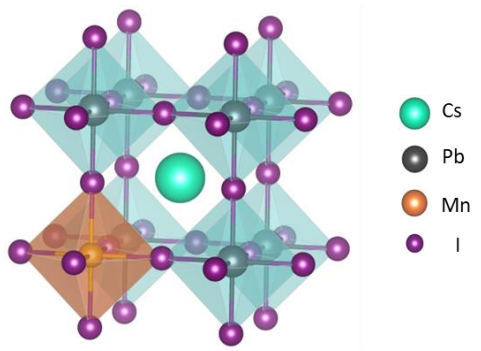

Figure 3.13 *Schematic of incorporation of Mn^{2+} ion in perovskite lattice.*

The transient absorption spectroscopy is used to characterize the HC relaxation dynamics in Mn-doped perovskite NCs under different excitation energies and intensities. After carrier-carrier scattering within 100 fs timescale, the HC redistributes and reaches Fermi-Dirac distribution with system energy being much higher than lattice temperature. The carrier temperature can be quantized by fitting the high energy tail of the beaching signal to the Boltzmann distribution. The analysis of HC cooling dynamics starts after a delay of 0.3 ps to ensure that HCs have redistributed their energies and reached the quasi-equilibrium status. Considering the simar effective masses of electrons and holes, the contribution from hot electrons and hot holes are assumed equal.

The HC relaxation dynamics of undoped and doped perovskite NCs under different excitation densities are presented as **Figure 3.14 (a-b)**. It is observed that HC relaxation is slowed down with increasing carrier densities in both samples. The kinetics can be well fitted with bi-exponential function, where the fast component is assigned to the HC relaxation via carrier-LO phonon coupling and the LO phonon decay is involved in explaining the slow component. The phenomenon is also observed under other excitation energies and can be explained by the enhanced hot

phonon bottleneck effect under high excitation intensity. The HC cooling dynamics of undoped and doped $CsPbI_3$ NCs under different excitation energies are shown as **Figure 3.14 (c-d)**, with fitted average HC lifetimes inserted inside figures. The 2.18 eV excitation is close to the energy of the bandgap and photogenerated HC has less excess energy compared to under 3.1 eV excitation. To have a clear observation of HC relaxation at different stages, the power loss rate as a function of carrier temperature is calculated as $P = d(1.5k_BT_c) / dt$. In summary, the HC relaxation in doped NCs is slower under 2.18 eV but faster under 3.1 eV excitation compared to undoped NCs.

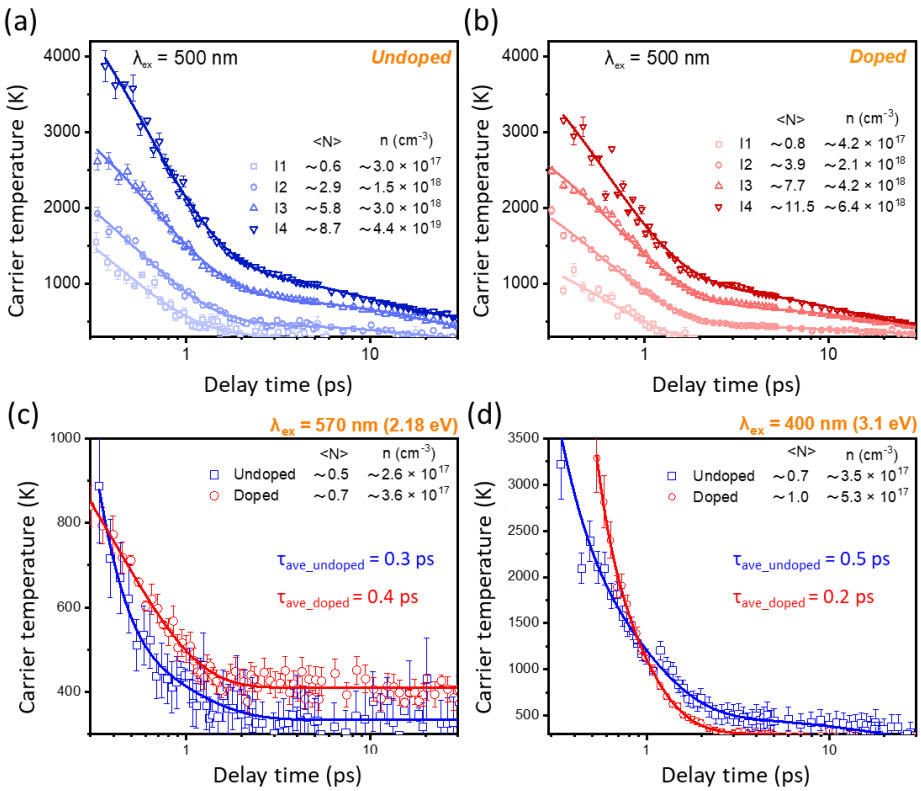

Figure 3.14 *TA results and analysis of carrier temperature in Mn-doped $CsPbI_3$ NCs. (a-b) Carrier temperature as a function of time delay under 500 nm (2.48 eV) excitation at different excitation intensities in undoped and doped perovskite NCs. (c-d) Carrier temperature decay profiles in undoped and doped perovskite NCs under 570 nm (2.18 eV) and 400 nm (3.1 eV) excitation.*

Two distinct slopes represent two HC relaxation stages, related to equilibrium between HC and LO phonons and equilibrium among HC, LO phonons and acoustic

phonons, respectively. The difference in relaxation rate in the two regions is highly dependent on material properties, i.e. electronic and phononic structure.

The electronic band structures of undoped and doped NCs are calculated using DFT, as shown in **Figure 3.15 (a-b)**. The effective masses of electrons and holes in doped NCs are greater than in undoped NCs due to the perturbation in the periodicity of Pb 6*p* orbital with Mn-doping. Due to the relation between Fröhlich coupling strength and effective masses, faster HC cooling is expected in doped NCs.[89] The strengthened carrier-LO phonon coupling is also confirmed by the temperature-dependent PL measurements. In addition, the calculation of density of states (DOS) in undoped and doped NCs shows that additional Mn orbitals are added into the original perovskite electronic structure (mainly Pb and I orbitals), which are marked in pink in the **Figure 3.15b**. As a result, when the sample is under high-energy excitation, more channels are possibly available for HC relaxation.

The projected phononic band structures of undoped and doped NCs are presented in **Figure 3.15 (c-d)**, with which we can evaluate the efficiency of LO phonons decay to acoustic phonons. The most efficient phonon decay channel is Klemens decay, where one LO phonon decays to two acoustic phonons with opposite wave vectors.[187] It can be significantly slowed down when the phononic bandgap between LO phonon and acoustic phonon is larger than the maximum energy of acoustic phonons, and results in a non-equilibrium population of LO phonons (hot phonon bottleneck). The phononic bandgap is enlarged in Mn-doped NCs due to the strain induced by Mn doping in local structure[188] and the requirement for hindering Klemens decay is fulfilled. Therefore, the LO phonon decays via other less efficient channels and potentially leads to a larger non-equilibrium population of LO phonons.

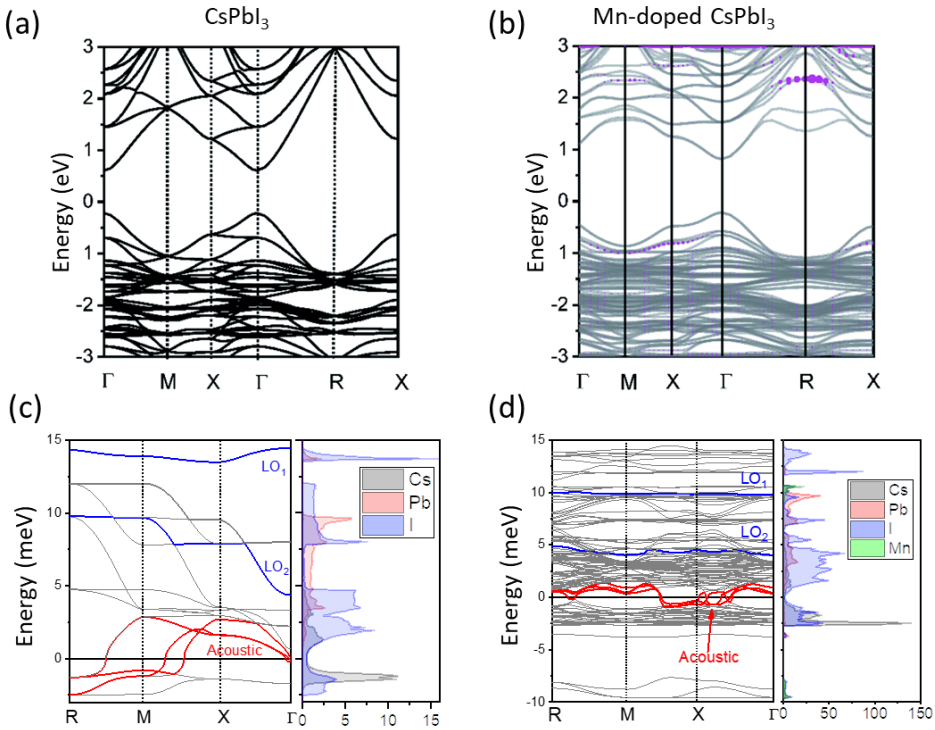

Figure 3.15 *Density functional theory (DFT) calculations on undoped and doped $CsPbI_3$ NCs. (a-b) Electronic band structures of undoped and doped perovskite NCs with corresponding (c-d) phonon energy as a function of phonon momentum and density of states.*

The influence of doping, carrier-LO phonon coupling and phonon decay on HC relaxation are summarized in **Figure 3.16 (a-b)**. Under 2.18 eV excitation (close to bandgap), the additional Mn orbitals have a minor impact on HC relaxation since they locate at higher excited states, as shown in **Figure 3.15b**. However, the increased phononic bandgap still plays a role in slowing down HC relaxation leading to a longer average HC lifetime in **Figure 3.14c**. Under high energy excitations, i.e. 2.48 eV and 3.1 eV, more factors need to be considered, as listed in **Figure 3.16b**. The faster relaxation rate in doped NCs is resulted from competition among the influence of additional Mn orbitals, enhanced carrier-LO phonon coupling and enlarged phononic bandgap. The output of competition is beneficial to establish the desired quasi-equilibrium state for HC extraction.

The influence of Mn doping on average HC lifetime is summarized in **Figure 3.16 (c-e)**. Under low energy excitation (2.18 eV), the HC relaxation is slowed down with increasing doping concentration as **Figure 3.16c**, with combined influence from the altered phononic structure and e-ph coupling. The change originates from

local lattice disordering around Mn atoms as confirmed by X-ray absorption near edge spectroscopy (XANES) characterization. Under high energy excitations, the average HC lifetime decreases with doping concentration under 2.48 eV excitation as **Figure 3.16d**, but first decreases and then increases with doping concentration under 3.1 eV as **Figure 3.16e**. As indicated by XANES measurements that the distortion of Mn-I bonds monotonously increases with doping concentration, the mixing (overlap) between orbitals of Mn and I are possibly altered, and the change significantly affects available states related to HC relaxation pathways. In addition, the dependence indicates the influence of addition pathways due to Mn orbitals dominates HC relaxation under low doping concentrations, while the enlargement in phononic bandgap dominates HC relaxation under high doping concentrations.

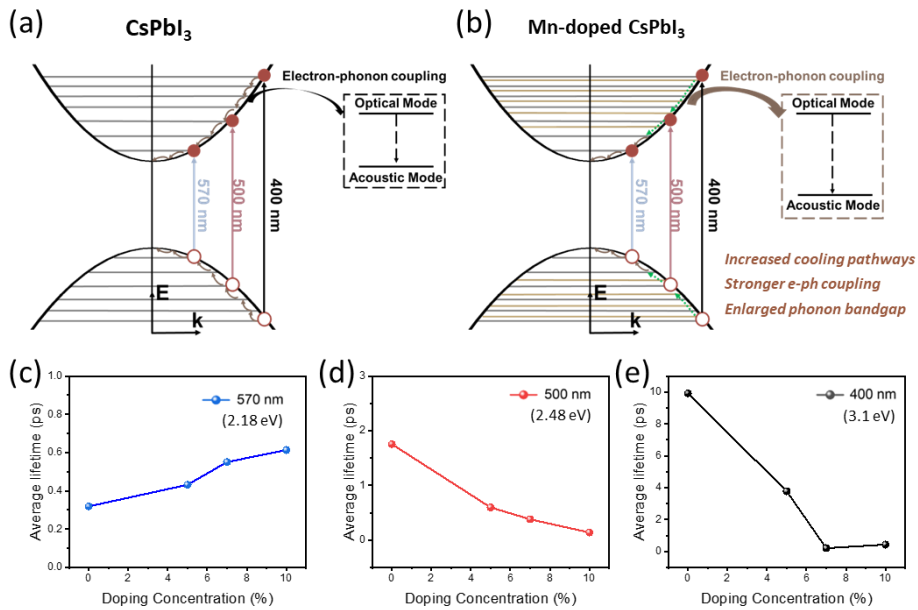

Figure 3.16 *Schematic of HC relaxation processes in undoped and doped $CsPbI_3$ NCs. (a-c) Average HC lifetime in Mn-doped $CsPbI_3$ perovskite NCs with different doping concentrations under 400 nm (3.1 eV), 500 nm (2.48 eV) or 570 nm (2.18 eV) excitation energies, respectively. (d-e) Illustration of HC relaxation in undoped and doped $CsPbI_3$ NCs with different excitation energies, where the organic lines represent the contribution of Mn orbitals in the electronic band structure.*

4 Conclusions

Paper I, II, III and V is a series of comprehensive investigations on the photophysics of two-dimensional (2D) perovskite single crystals, by carefully assessing the charge carrier dynamics and revealing the relation between structural distortion and electronic structure. Two key approaches we applied in the investigations: (1) comparing photophysics properties of 2D perovskite single crystals with different compositions and different facets of the crystal, and (2) applying various ultrafast spectroscopy techniques to provide information on hot carrier relaxation from different aspects.

The formula of lead halide two-dimensional perovskites can be presented as $(A')_2A_{n-1}B_nX_{3n+1}$, where A' is the long-chain organic spacer, A is the cation inside the octahedral cage, B is the Pb^{2+} cation, X is the halogen and *n* is the number of octahedral layers in one unit cell. The existence of spacers enables the ability to extend the selection range of molecular compositions in 2D perovskite compared to its 3D alternatives. In this thesis, different targeted samples are used with varying the A' spacer cation (Paper III), A-site cation (Paper II) and *n*-value (Paper V).

In Paper II, we characterize the lattice and electronic structure of $(n\text{-}BA)_2(MA)_2Pb_3I_{10}$ (BMAPI) and $(n\text{-}BA)_2(EA)_2Pb_3I_{10}$ (BEAPI) single crystals. Two samples have different degrees of lattice distortion and we confirm the relaxed threshold on tolerance factor in 2D perovskite, with accumulated strain in rigid octahedral layers being compensated by the flexible long-chain spacers. In addition, we find that BEAPI, which has greater lattice distortion, has a larger band gap and higher trap state density compared to BMAPI.

In Paper III, we further extend the investigation on the link between structure and photophysics in 2D perovskites by studying PL signals from different facets of bulky $(iso\text{-}BA)_2(MA)Pb_2Br_7$ (iso-BAPB), $(n\text{-}BA)_2(MA)Pb_2Br_7$ (n-BAPB), and $(n\text{-}PA)_2(MA)Pb_2Br_7$ (n-PAPB) single crystals. Based on structure characterization, we find that internal lattice mismatch varies in samples with different spacers, which provides evidence that the spacers contribute to releasing internal strain accumulation. In all samples, a red shift around 0.4 eV in PL spectra is observed on the facet perpendicular to the 2D layer (PF), in comparison to the in-plane facet (IF). We propose that the free carriers dominate the emission from IF and STE are the main emitters from the PF of 2D perovskite single crystals.

In Paper V, we directly characterize the electronic structure at different areas of samples with different *n*-value, with formula as $(BA)_2PbI_4$, $(BA)_2(MA)Pb_2I_7$ and $(BA)_2(MA)_2Pb_3I_{10}$. Based on X-ray photoemission electron microscopy measurements, photoelectrons emitted from Pb 5*d* and I 4*d* core levels are mapped at the edge and bulk areas of single crystals. The emissions from the Pb 5*d* core level at edge areas are blue-shifted compared to bulk areas in all samples, with the most significant ~ 1.0 eV shift observed in the $n = 3$ sample. However, no significant shift is observed in emission from I 4*d* core level at edge and bulk areas. We believe the asymmetric shifts in core level emission can be attributed to the different degrees of lattice distortion at edge and bulk areas, where the strain accumulated along the 2D layer is released at the edge area. In addition, the shift in Pb 5*d* core level emission from edge and bulk areas depends on the *n*-value of samples, and is because the in-plane lattice strain in samples with $n = 1$ and 2 can be efficiently buffered by spacers, which is not the case in the sample with $n = 3$.

In the above-mentioned papers, we focus on studying the relation between lattice structure and electronic structure, by comparing 2D perovskite with different compositions or detecting signals from different areas of the sample.

In Paper I, we explore the ultrafast charge carrier dynamics (hot carrier relaxation) in 2D perovskite using transient absorption (TA) spectroscopy and time-resolved two-photon photoemission (TR-2PPE) spectroscopy. The distribution of hot electrons can be directly mapped in TR-2PPE measurements, as well as its relaxation dynamics in the conduction band. The hot carrier decay kinetics obtained from the two techniques both have two cooling stages due to the hot phonon bottleneck effect, while a faster cooling rate in Stage I and a higher initial carrier temperature in Stage II are observed in TA analysis. Since the whole bulk area is probed in TA measurements while TR-2PPE signals mainly come from the outermost layer, we believe the spatial sensitivity of cooling dynamics across the 2D perovskite single crystal contributes to the different cooling rates in Stage I observed in two techniques.

2D perovskite has shown its potential in solar cell applications as a promising building block, and we perform a series of investigations on 2D perovskite single crystals to characterize its intrinsic properties and relation with lattice structure.

In Paper IV, we investigate the impact of transition metal doping on electronic and phononic properties in 3D perovskite nanocrystals and the resulted change in hot carrier relaxation kinetics between doped and undoped samples under different excitation intensities and energies. In Mn^{2+}-doped $CsPbI_3$ nanocrystals, the phononic gap between longitudinal optical (LO) – acoustic phonon is enlarged, the coupling strength of carrier-LO phonon interaction is enhanced and additional HC relaxation pathways are added via Mn orbitals within bands, compared to the undoped sample. The phenomenon is optimal for hot carrier solar cell application,

where a high-temperature thermal quasi-equilibrium is established for recycling the energy from the hot carrier relaxation to reheat the cold carriers.

References

(1) Snaith, H. J. Present status and future prospects of perovskite photovoltaics. *Nat. Mater.* **2018**, *17*, 372-376.

(2) Green, M. A.; Bremner, S. P. Energy conversion approaches and materials for high-efficiency photovoltaics. *Nat. Mater.* **2017**, *16*, 23-34.

(3) Green, M. A.; Ho-Baillie, A.; Snaith, H. J. The emergence of perovskite solar cells. *Nat. Photonics* **2014**, *8*, 506-514.

(4) Green, M. A. Third generation photovoltaics: solar cells for 2020 and beyond. *Physica E* **2002**, *14*(1-2), 65-70.

(5) Shockley, W.; Queisser, H. J. Detailed Balance Limit of Efficiency of p-n Junction Solar Cells. *J. Appl. Phys.* **1961**, *32*(3), 510-519.

(6) Rao, A.; Friend, R. H. Harnessing singlet exciton fission to break the Shockley–Queisser limit. *Nat. Rev. Mater.* **2017**, *2*, 17063.

(7) Semonin, O. E.; Luther, J. M.; Choi, S.; Chen, H. Y.; Gao, J.; Nozik, A. J.; Beard, M. C. Peak External Photocurrent Quantum Efficiency Exceeding 100% via MEG in a Quantum Dot Solar Cell. *Science* **2011**, *334*(6062), 1530-1533.

(8) Paul, K. K.; Kim, J.-H.; Lee, Y. H. Hot carrier photovoltaics in van der Waals heterostructures. *Nat. Rev. Phys.* **2021**, *3*, 178-192.

(9) Liu, C.; Lu, Y.; Shen, R.; Dai, Y.; Yu, X.; Liu, K.; Lin, S. Dynamics and physical process of hot carriers in optoelectronic devices. *Nano Energy* **2022**, *95*, 106977.

(10) Conibeer, G.; Shrestha, S.; Huang, S.; Patterson, R.; Xia, H.; Feng, Y.; Zhang, P.; Gupta, N.; Tayebjee, M.; Smyth, S.; Liao, Y.; Lin, S.; Wang, P.; Dai, X.; Chung, S. Hot carrier solar cell absorber prerequisites and candidate material systems. *Sol. Energy Mater. Sol. Cells* **2015**, *135*, 124-129.

(11) Hirst, L. C.; Lumb, M. P.; Hoheisel, R.; Bailey, C. G.; Philipps, S. P.; Bett, A. W.; Walters, R. J. Spectral sensitivity of hot carrier solar cells. *Sol. Energy Mater. Sol. Cells* **2014**, *120*, 610-615.

(12) Li, M.; Fu, J.; Xu, Q.; Sum, T. C. Slow Hot-Carrier Cooling in Halide Perovskites: Prospects for Hot-Carrier Solar Cells. *Adv. Mater.* **2019**, *31*(47), 1802486.

(13) Ross, R. T.; Nozik, A. J. Efficiency of hot -carrier solar energy converters. *J. Appl. Phys.* **1982**, *53*(5), 3813-3818.

(14) Chakhmouradian, A. R.; Woodward, P. M. Celebrating 175 years of perovskite research: a tribute to Roger H. Mitchell. *Phys. Chem. Miner.* **2014**, *41*(6), 387-391.

(15) Wells, H. L. Über die Cäsium- und Kalium-Bleihalogenide. *Z. Anorg. Chem.* **1893**, *3*(1), 195-210.

(16) Weber, D. $CH_3NH_3PbX_3$, ein Pb(II)-System mit kubischer Perowskitstruktur / $CH_3NH_3PbX_3$, a Pb(II)-System with Cubic Perovskite Structure. *Z. Naturforsch. B* **1978**, *33*(12), 1443-1445.

(17) Correa-Baena, J.-P.; Saliba, M.; Buonassisi, T.; Grätzel, M.; Abate, A.; Tress, W.; Hagfeldt, A. Promises and challenges of perovskite solar cells. *Science* **2017**, *358*(6364), 739-744.

(18) Snaith, H. J. Perovskites: The Emergence of a New Era for Low-Cost, High-Efficiency Solar Cells. *J. Phys. Chem. Lett.* **2013**, *4*(21), 3623-3630.

(19) Chen, J.; Xiang, H.; Wang, J.; Wang, R.; Li, Y.; Shan, Q.; Xu, X.; Dong, Y.; Wei, C.; Zeng, H. Perovskite White Light Emitting Diodes: Progress, Challenges, and Opportunities. *ACS Nano* **2021**, *15*(11), 17150−17174.

(20) Zhang, K.; Zhu, N.; Zhang, M.; Wang, L.; Xing, J. Opportunities and challenges in perovskite LED commercialization. *J. Mater. Chem. C* **2021**, *9*(11), 3795-3799.

(21) Ahmadi, M.; Wu, T.; Hu, B. A Review on Organic–Inorganic Halide Perovskite Photodetectors: Device Engineering and Fundamental Physics. *Adv. Mater.* **2017**, *29*(41), 1605242.

(22) Liu, X.-K.; Xu, W.; Bai, S.; Jin, Y.; Wang, J.; Friend, R. H.; Gao, F. Metal halide perovskites for light-emitting diodes. *Nat. Mater.* **2021**, *20*, 10-21.

(23) Razza, S.; Castro-Hermosa, S.; Di Carlo, A.; Brown, T. M. Research Update: Large-area deposition, coating, printing, and processing techniques for the upscaling of perovskite solar cell technology. *APL Mater.* **2016**, *4*(9), 091508.

(24) Goldschmidt, V. M. Die Gesetze der Krystallochemie. *Die Naturwissenschaften* **1926**, *14*(21), 477-485.

(25) Ji, D.; Feng, S.; Wang, L.; Wang, S.; Na, M.; Zhang, H.; Zhang, C.; Li, X. Regulatory tolerance and octahedral factors by using vacancy in $APbI_3$ perovskites. *Vacuum* **2019**, *164*, 186-193.

(26) Fu, Y.; Zhu, H.; Chen, J.; Hautzinger, M. P.; Zhu, X. Y.; Jin, S. Metal halide perovskite nanostructures for optoelectronic applications and the study of physical properties. *Nat. Rev. Mater.* **2019**, *4*, 169-188.

(27) Han, G.; Hadi, H. D.; Bruno, A.; Kulkarni, S. A.; Koh, T. M.; Wong, L. H.; Soci, C.; Mathews, N.; Zhang, S.; Mhaisalkar, S. G. Additive Selection Strategy for High Performance Perovskite Photovoltaics. *J. Phys. Chem. C* **2018**, *122*(25), 13884-13893.

(28) Kirschner, M. S.; Diroll, B. T.; Guo, P.; Harvey, S. M.; Helweh, W.; Flanders, N. C.; Brumberg, A.; Watkins, N. E.; Leonard, A. A.; Evans, A. M.; Wasielewski, M. R.; Dichtel, W. R.; Zhang, X.; Chen, L. X.; Schaller, R. D. Photoinduced, reversible phase transitions in all-inorganic perovskite nanocrystals. *Nat. Commun.* **2019**, *10*, 504.

(29) Jain, P.; Dalal, N. S.; Toby, B. H.; Kroto, H. W.; Cheetham, A. K. Order−Disorder Antiferroelectric Phase Transition in a Hybrid Inorganic−Organic Framework with the Perovskite Architecture. *J. Am. Chem. Soc.* **2008**, *130*(32), 10450-10451.

(30) Parrott, E. S.; Milot, R. L.; Stergiopoulos, T.; Snaith, H. J.; Johnston, M. B.; Herz, L. M. Effect of Structural Phase Transition on Charge-Carrier Lifetimes and Defects in $CH_3NH_3SnI_3$ Perovskite. *J. Phys. Chem. Lett.* **2016**, *7*(7), 1321-1326.

(31) Quarti, C.; Mosconi, E.; Ball, J. M.; D'Innocenzo, V.; Tao, C.; Pathak, S.; Snaith, H. J.; Petrozza, A.; De Angelis, F. Structural and optical properties of methylammonium lead iodide across the tetragonal to cubic phase transition: implications for perovskite solar cells. *Energy Environ. Sci.* **2016**, *9*(1), 155-163.

(32) Poglitsch, A.; Weber, D. Dynamic disorder in methylammoniumtrihalogenoplumbates (II) observed by millimeter - wave spectroscopy. *J. Chem. Phys.* **1987**, *87*(11), 6373-6378.

(33) Wehrenfennig, C.; Liu, M.; Snaith, H. J.; Johnston, M. B.; Herz, L. M. Homogeneous Emission Line Broadening in the Organo Lead Halide Perovskite $CH_3NH_3PbI_{3-x}Cl_x$. *J. Phys. Chem. Lett.* **2014**, *5*(8), 1300-1306.

(34) Shi, D.; Adinolfi, V.; Comin, R.; Yuan, M.; Alarousu, E.; Buin, A.; Chen, Y.; Hoogland, S.; Rothenberger, A.; Katsiev, K.; Losovyj, Y.; Zhang, X.; Dowben, P. A.; Mohammed, O. F.; Sargent, E. H.; Bakr, O. M. Low trap-state density and long carrier diffusion in organolead trihalide perovskite single crystals. *Science* **2015**, *347*(6221), 519-522.

(35) Chen, Y.; Yi, H. T.; Wu, X.; Haroldson, R.; Gartstein, Y. N.; Rodionov, Y. I.; Tikhonov, K. S.; Zakhidov, A.; Zhu, X. Y.; Podzorov, V. Extended carrier lifetimes and diffusion in hybrid perovskites revealed by Hall effect and photoconductivity measurements. *Nat. Commun.* **2016**, *7*, 12253.

(36) Stranks, S. D.; Eperon, G. E.; Grancini, G.; Menelaou, C.; Alcocer, M. J. P.; Leijtens, T.; Herz, L. M.; Petrozza, A.; Snaith, H. J. Electron-Hole Diffusion Lengths Exceeding 1 Micrometer in an Organometal Trihalide Perovskite Absorber. *Science* **2013**, *342*(6156), 341-344.

(37) Guo, Z.; Wan, Y.; Yang, M.; Snaider, J.; Zhu, K.; Huang, L. Long-range hot-carrier transport in hybrid perovskites visualized by ultrafast microscopy. *Science* **2017**, *356*(6333), 59–62.

(38) Xing, G.; Mathews, N.; Sun, S.; Lim, S. S.; Lam, Y. M.; Gratzel, M.; Mhaisalkar, S.; Sum, T. C. Long-Range Balanced Electron- and Hole-Transport Lengths in Organic-Inorganic $CH_3NH_3PbI_3$. *Science* **2013**, *342*(6156), 344-347.

(39) Steirer, K. X.; Schulz, P.; Teeter, G.; Stevanovic, V.; Yang, M.; Zhu, K.; Berry, J. J. Defect Tolerance in Methylammonium Lead Triiodide Perovskite. *ACS Energy Lett.* **2016**, *1*(2), 360-366.

(40) Dirin, D. N.; Protesescu, L.; Trummer, D.; Kochetygov, I. V.; Yakunin, S.; Krumeich, F.; Stadie, N. P.; Kovalenko, M. V. Harnessing Defect-Tolerance at the Nanoscale: Highly Luminescent Lead Halide Perovskite Nanocrystals in Mesoporous Silica Matrixes. *Nano Lett.* **2016**, *16*(9), 5866-5874.

(41) Brandt, R. E.; Poindexter, J. R.; Gorai, P.; Kurchin, R. C.; Hoye, R. L. Z.; Nienhaus, L.; Wilson, M. W. B.; Polizzotti, J. A.; Sereika, R.; Žaltauskas, R.; Lee, L. C.; Macmanus-Driscoll, J. L.; Bawendi, M.; Stevanović, V.; Buonassisi, T. Searching for "Defect-Tolerant" Photovoltaic Materials: Combined Theoretical and Experimental Screening. *Chem. Mater.* **2017**, *29*(11), 4667-4674.

(42) Yin, W.-J.; Yang, J.-H.; Kang, J.; Yan, Y.; Wei, S.-H. Halide perovskite materials for solar cells: a theoretical review. *J. Mater. Chem. A* **2015**, *3*(17), 8926-8942.

(43) Elumalai, N.; Mahmud, M.; Wang, D.; Uddin, A. Perovskite Solar Cells: Progress and Advancements. *Energies* **2016**, *9*(11), 861.

(44) Wang, D.; Wright, M.; Elumalai, N. K.; Uddin, A. Stability of perovskite solar cells. *Sol. Energy Mater. Sol. Cells* **2016**, *147*, 255-275.

(45) Saliba, M.; Matsui, T.; Seo, J.-Y.; Domanski, K.; Correa-Baena, J.-P.; Nazeeruddin, M. K.; Zakeeruddin, S. M.; Tress, W.; Abate, A.; Hagfeldt, A.; Grätzel, M. Cesium-containing triple cation perovskite solar cells: improved stability, reproducibility and high efficiency. *Energy Environ. Sci.* **2016**, *9*(6), 1989-1997.

(46) Bai, Y.; Dong, Q.; Shao, Y.; Deng, Y.; Wang, Q.; Shen, L.; Wang, D.; Wei, W.; Huang, J. Enhancing stability and efficiency of perovskite solar cells with crosslinkable silane-functionalized and doped fullerene. *Nat. Commun.* **2016**, *7*, 12806.

(47) Jiang, Y.; Qiu, L.; Juarez-Perez, E. J.; Ono, L. K.; Hu, Z.; Liu, Z.; Wu, Z.; Meng, L.; Wang, Q.; Qi, Y. Reduction of lead leakage from damaged lead halide perovskite solar modules using self-healing polymer-based encapsulation. *Nat. Energy* **2019**, *4*, 585-593.

(48) Tsai, H.; Nie, W.; Blancon, J. C.; Stoumpos, C. C.; Asadpour, R.; Harutyunyan, B.; Neukirch, A. J.; Verduzco, R.; Crochet, J. J.; Tretiak, S.; Pedesseau, L.; Even, J.; Alam, M. A.; Gupta, G.; Lou, J.; Ajayan, P. M.; Bedzyk, M. J.; Kanatzidis, M. G. High-efficiency two-dimensional Ruddlesden-Popper perovskite solar cells. *Nature* **2016**, *536*, 312-316.

(49) Even, J.; Pedesseau, L.; Katan, C. Understanding Quantum Confinement of Charge Carriers in Layered 2D Hybrid Perovskites. *ChemPhysChem* **2014**, *15*(17), 3733-3741.

(50) Pedesseau, L.; Sapori, D.; Traore, B.; Robles, R.; Fang, H.-H.; Loi, M. A.; Tsai, H.; Nie, W.; Blancon, J.-C.; Neukirch, A.; Tretiak, S.; Mohite, A. D.; Katan, C.; Even, J.; Kepenekian, M. Advances and Promises of Layered Halide Hybrid Perovskite Semiconductors. *ACS Nano* **2016**, *10*(11), 9776-9786.

(51) Stoumpos, C. C.; Cao, D. H.; Clark, D. J.; Young, J.; Rondinelli, J. M.; Jang, J. I.; Hupp, J. T.; Kanatzidis, M. G. Ruddlesden–Popper Hybrid Lead Iodide Perovskite 2D Homologous Semiconductors. *Chem. Mater.* **2016**, *28*(8), 2852-2867.

(52) Li, X.; Ke, W.; Traoré, B.; Guo, P.; Hadar, I.; Kepenekian, M.; Even, J.; Katan, C.; Stoumpos, C. C.; Schaller, R. D.; Kanatzidis, M. G. Two-Dimensional Dion–Jacobson Hybrid Lead Iodide Perovskites with Aromatic Diammonium Cations. *J. Am. Chem. Soc.* **2019**, *141*(32), 12880-12890.

(53) Ghosh, D.; Acharya, D.; Pedesseau, L.; Katan, C.; Even, J.; Tretiak, S.; Neukirch, A. J. Charge carrier dynamics in two-dimensional hybrid perovskites: Dion–Jacobson vs. Ruddlesden–Popper phases. *J. Mater. Chem. A* **2020**, *8*(42), 22009-22022.

(54) Smith, I. C.; Hoke, E. T.; Solis-Ibarra, D.; McGehee, M. D.; Karunadasa, H. I. A Layered Hybrid Perovskite Solar-Cell Absorber with Enhanced Moisture Stability. *Angew. Chem. Int. Ed.* **2014**, *53*(42), 11232-11235.

(55) Shao, M.; Bie, T.; Yang, L.; Gao, Y.; Jin, X.; He, F.; Zheng, N.; Yu, Y.; Zhang, X. Over 21% Efficiency Stable 2D Perovskite Solar Cells. *Adv. Mater.* **2022**, *34*(1), 2107211.

(56) Zhang, F.; Lu, H.; Tong, J.; Berry, J. J.; Beard, M. C.; Zhu, K. Advances in two-dimensional organic–inorganic hybrid perovskites. *Energy Environ. Sci.* **2020**, *13*(4), 1154-1186.

(57) Yuan, M.; Quan, L. N.; Comin, R.; Walters, G.; Sabatini, R.; Voznyy, O.; Hoogland, S.; Zhao, Y.; Beauregard, E. M.; Kanjanaboos, P.; Lu, Z.; Kim, D. H.; Sargent, E. H. Perovskite energy funnels for efficient light-emitting diodes. *Nat. Nanotechnol.* **2016**, *11*, 872-877.

(58) Liang, M.; Lin, W.; Lan, Z.; Meng, J.; Zhao, Q.; Zou, X.; Castelli, I. E.; Pullerits, T.; Canton, S. E.; Zheng, K. Electronic Structure and Trap States of Two-Dimensional Ruddlesden–Popper Perovskites with the Relaxed Goldschmidt Tolerance Factor. *ACS Appl. Electron. Mater.* **2020**, *2*(5), 1402-1412.

(59) König, D.; Casalenuovo, K.; Takeda, Y.; Conibeer, G.; Guillemoles, J. F.; Patterson, R.; Huang, L. M.; Green, M. A. Hot carrier solar cells: Principles, materials and design. *Physica E* **2010**, *42*(10), 2862-2866.

(60) Williams, F.; Nozik, A. J. Solid-state perspectives of the photoelectrochemistry of semiconductor-electrolyte junctions. *Nature* **1984**, *312*, 21-27.

(61) Nozik, A. J. Photoelectrochemical cells. *Philos. Trans. R. Soc. London. Ser. A* **1980**, *295*(1414), 453-470.

(62) Landsberg, P. T.; Nussbaumer, H.; Willeke, G. Band-band impact ionization and solar cell efficiency. *J. Appl. Phys.* **1993**, *74*(2), 1451-1452.

(63) Kolodinski, S.; Werner, J. H.; Wittchen, T.; Queisser, H. J. Quantum efficiencies exceeding unity due to impact ionization in silicon solar cells. *Appl. Phys. Lett.* **1993**, *63*(17), 2405-2407.

(64) Zhu, H.; Miyata, K.; Fu, Y.; Wang, J.; Joshi, P. P.; Niesner, D.; Williams, K. W.; Jin, S.; Zhu, X.-Y. Screening in crystalline liquids protects energetic carriers in hybrid perovskites. *Science* **2016**, *353*(6306), 1409-1413.

(65) Niesner, D.; Zhu, H.; Miyata, K.; Joshi, P. P.; Evans, T. J.; Kudisch, B. J.; Trinh, M. T.; Marks, M.; Zhu, X. Y. Persistent Energetic Electrons in Methylammonium Lead Iodide Perovskite Thin Films. *J. Am. Chem. Soc.* **2016**, *138*(48), 15717-15726.

(66) Nozik, A. J. Spectroscopy and hot electron relaxation dynamics In semiconductor quantum wells and quantum dots. *Annu. Rev. Phys. Chem.* **2001**, *52*, 193-231.

(67) Elkins, M. H.; Pensack, R.; Proppe, A. H.; Voznyy, O.; Quan, L. N.; Kelley, S. O.; Sargent, E. H.; Scholes, G. D. Biexciton Resonances Reveal Exciton Localization in Stacked Perovskite Quantum Wells. *J. Phys. Chem. Lett.* **2017**, *8*(16), 3895-3901.

(68) March, S. A.; Riley, D. B.; Clegg, C.; Webber, D.; Liu, X.; Dobrowolska, M.; Furdyna, J. K.; Hill, I. G.; Hall, K. C. Four-Wave Mixing in Perovskite Photovoltaic Materials Reveals Long Dephasing Times and Weaker Many-Body Interactions than GaAs. *ACS Photonics* **2017**, *4*(6), 1515-1521.

(69) Richter, J. M.; Branchi, F.; Valduga de Almeida Camargo, F.; Zhao, B.; Friend, R. H.; Cerullo, G.; Deschler, F. Ultrafast carrier thermalization in lead iodide perovskite probed with two-dimensional electronic spectroscopy. *Nat. Commun.* **2017**, *8*, 376.

(70) Lin, Q.; Armin, A.; Nagiri, R. C. R.; Burn, P. L.; Meredith, P. Electro-optics of perovskite solar cells. *Nat. Photonics* **2015**, *9*, 106-112.

(71) Hirasawa, M.; Ishihara, T.; Goto, T.; Uchida, K.; Miura, N. Magnetoabsorption of the lowest exciton in perovskite-type compound (CH_3NH_3)PbI_3. *Physica B* **1994**, *201*, 427-430.

(72) Sinba, S. K. Phonons in semiconductors. *CRC crit. rev. solid state mater. sci.* **1973**, *3*(3), 273-334.

(73) Zhang, X. B.; Taliercio, T.; Kolliakos, S.; Lefebvre, P. Influence of electron-phonon interaction on the optical properties of III nitride semiconductors. *J. Phys. Condens. Matter* **2001**, *13*, 7053.

(74) Zheng, F.; Wang, L.-W. Large polaron formation and its effect on electron transport in hybrid perovskites. *Energy Environ. Sci.* **2019**, *12*(4), 1219-1230.

(75) Iaru, C. M.; Brodu, A.; Van Hoof, N. J. J.; Ter Huurne, S. E. T.; Buhot, J.; Montanarella, F.; Buhbut, S.; Christianen, P. C. M.; Vanmaekelbergh, D.; De Mello Donega, C.; Rivas, J. G.; Koenraad, P. M.; Silov, A. Y. Fröhlich interaction dominated by a single phonon mode in $CsPbBr_3$. *Nat. Commun.* **2021**, *12*, 5844.

(76) Klemens, P. G. Anharmonic Decay of Optical Phonons. *Phys. Rev.* **1966**, *148*(2), 845-848.

(77) Ridley, B. K. Electron scattering by confined LO polar phonons in a quantum well. *Phys. Rev. B* **1989**, *39*(8), 5282-5286.

(78) Pérez-Osorio, M. A.; Milot, R. L.; Filip, M. R.; Patel, J. B.; Herz, L. M.; Johnston, M. B.; Giustino, F. Vibrational Properties of the Organic–Inorganic Halide Perovskite $CH_3NH_3PbI_3$from Theory and Experiment: Factor Group Analysis, First-Principles Calculations, and Low-Temperature Infrared Spectra. *J. Phys. Chem. C* **2015**, *119*(46), 25703-25718.

(79) Vallée, F.; Bogani, F. Coherent time-resolved investigation of LO-phonon dynamics in GaAs. *Phys. Rev. B* **1991**, *43*(14), 12049-12052.

(80) Barman, S.; Srivastava, G. P. Long-wavelength nonequilibrium optical phonon dynamics in cubic and hexagonal semiconductors. *Phys. Rev. B* **2004**, *69*(23), 235208.

(81) Ecsedy, D. J.; Klemens, P. G. Thermal resistivity of die ectric crystals due to four-phonon processes and optical modes. *Phys. Rev. B* **1977**, *15*(12), 5957-5962.

(82) Srivastava, G. P. Origin of the hot phonon effect in group-III nitrides. *Phys. Rev. B* **2008**, *77*(15), 155205.

(83) Wang, R.; Zobeiri, H.; Xie, Y.; Wang, X.; Zhang, X.; Yue, Y. Distinguishing Optical and Acoustic Phonon Temperatures and Their Energy Coupling Factor under Photon Excitation in nm 2D Materials. *Adv. Sci.* **2020**, *7*(13), 2000097.

(84) Yang, C. H.; Carlson-Swindle, J. M.; Lyon, S. A.; Worlock, J. M. Hot-Electron Relaxation in GaAs Quantum Wells. *Phys. Rev. Lett.* **1985**, *55*(21), 2359-2361.

(85) Yang, J.; Wen, X.; Xia, H.; Sheng, R.; Ma, Q.; Kim, J.; Tapping, P.; Harada, T.; Kee, T. W.; Huang, F.; Cheng, Y. B.; Green, M.; Ho-Baillie, A.; Huang, S.; Shrestha, S.; Patterson, R.; Conibeer, G. Acoustic-optical phonon up-conversion and hot-phonon bottleneck in lead-halide perovskites. *Nat. Commun.* **2017**, *8*, 14120.

(86) Wright, A. D.; Verdi, C.; Milot, R. L.; Eperon, G. E.; Perez-Osorio, M. A.; Snaith, H. J.; Giustino, F.; Johnston, M. B.; Herz, L. M. Electron-phonon coupling in hybrid lead halide perovskites. *Nat. Commun.* **2016**, *7*, 11755.

(87) Kawai, H.; Giorgi, G.; Marini, A.; Yamashita, K. The mechanism of slow hot-hole cooling in lead-iodide perovskite: first-principles calculation on carrier lifetime from electron-phonon interaction. *Nano Lett.* **2015**, *15*(5), 3103-3108.

(88) Yang, Y.; Ostrowski, D. P.; France, R. M.; Zhu, K.; van de Lagemaat, J.; Luther, J. M.; Beard, M. C. Observation of a hot-phonon bottleneck in lead-iodide perovskites. *Nat. Photonics* **2015**, *10*, 53-59.

(89) Fu, J.; Xu, Q.; Han, G.; Wu, B.; Huan, C. H. A.; Leek, M. L.; Sum, T. C. Hot carrier cooling mechanisms in halide perovskites. *Nat. Commun.* **2017**, *8*, 1300.

(90) van Hest, J.; Blab, G. A.; Gerritsen, H. C.; de Mello Donega, C.; Meijerink, A. The Role of a Phonon Bottleneck in Relaxation Processes for Ln-Doped $NaYF_4$ Nanocrystals. *J. Phys. Chem. C* **2018**, *122*(7), 3985-3993.

(91) Efros, A. L.; Rosen, M. The Electronic Structure of Semiconductor Nanocrystals. *Annu. Rev. Mater. Sci.* **2000**, *30*, 475-521.

(92) Inoshita, T.; Sakaki, H. Electron-phonon interaction and the so-called phonon bottleneck effect in semiconductor quantum dots. *Physica B* **1996**, *227*(1-4), 373-377.

(93) Schaller, R. D.; Pietryga, J. M.; Goupalov, S. V.; Petruska, M. A.; Ivanov, S. A.; Klimov, V. I. Breaking the Phonon Bottleneck in Semiconductor Nanocrystals via Multiphonon Emission Induced by Intrinsic Nonadiabatic Interactions. *Phys. Rev. Lett.* **2005**, *95*(19), 196401.

(94) Cooney, R. R.; Sewall, S. L.; Dias, E. A.; Sagar, D. M.; Anderson, K. E. H.; Kambhampati, P. Unified picture of electron and hole relaxation pathways in semiconductor quantum dots. *Phys. Rev. B* **2007**, *75*(24), 245311.

(95) Wang, L.; Chen, Z.; Liang, G.; Li, Y.; Lai, R.; Ding, T.; Wu, K. Observation of a phonon bottleneck in copper-doped colloidal quantum dots. *Nat. Commun.* **2019**, *10*, 4532.

(96) Efros, A. L.; Kharchenko, V. A.; Rosen, M. Breaking the phonon bottleneck in nanometer quantum dots: Role of Auger-like processes. *Solid State Commun.* **1995**, *93*(4), 281-284.

(97) Guyot-Sionnest, P.; Shim, M.; Matranga, C.; Hines, M. Intraband relaxation in CdSe quantum dots. *Phys. Rev. B* **1999**, *60*(4), R2181-R2184.

(98) Sercel, P. C. Multiphonon-assisted tunneling through deep levels: A rapid energy-relaxation mechanism in nonideal quantum-dot heterostructures. *Phys. Rev. B* **1995**, *51*(20), 14532-14541.

(99) Inoshita, T.; Sakaki, H. Density of states and phonon-induced relaxation of electrons in semiconductor quantum dots. *Phys. Rev. B* **1997**, *56*(8), R4355-R4358.

(100) Inoshita, T.; Sakaki, H. Electron relaxation in a quantum dot: Significance of multiphonon processes. *Phys. Rev. B* **1992**, *46*(11), 7260-7263.

(101) Prezhdo, O. V. Multiple excitons and the electron–phonon bottleneck in semiconductor quantum dots: An ab initio perspective. *Chem. Phys. Lett.* **2008**, *460*(1-3), 1-9.

(102) Prabhu, S. S.; Vengurlekar, A. S.; Roy, S. K.; Shah, J. Nonequilibrium dynamics of hot carriers and hot phonons in CdSe and GaAs. *Phys. Rev. B* **1995**, *51*(20), 14233-14246.

(103) Chatzakis, I.; Yan, H.; Song, D.; Berciaud, S.; Heinz, T. F. Temperature dependence of the anharmonic decay of optical phonons in carbon nanotubes and graphite. *Phys. Rev. B* **2011**, *83*(20), 205411.

(104) Li, M.; Bhaumik, S.; Goh, T. W.; Kumar, M. S.; Yantara, N.; Gratzel, M.; Mhaisalkar, S.; Mathews, N.; Sum, T. C. Slow cooling and highly efficient extraction of hot carriers in colloidal perovskite nanocrystals. *Nat. Commun.* **2017**, *8*, 14350.

(105) Klimov, V.; Haring Bolivar, P.; Kurz, H. Hot-phonon effects in femtosecond luminescence spectra of electron-hole plasmas in CdS. *Phys. Rev. B* **1995**, *52*(7), 4728-4731.

(106) Bockelmann, U.; Bastard, G. Phonon scattering and energy relaxation in two-, one-, and zero-dimensional electron gases. *Phys. Rev. B* **1990**, *42*(14), 8947-8951.

(107) Clady, R.; Tayebjee, M. J. Y.; Aliberti, P.; König, D.; Ekins-Daukes, N. J.; Conibeer, G. J.; Schmidt, T. W.; Green, M. A. Interplay between the hot phonon effect and intervalley scattering on the cooling rate of hot carriers in GaAs and InP. *Prog. Photovolt.* **2012**, *20*(1), 82-92.

(108) Monahan, D. M.; Guo, L.; Lin, J.; Dou, L.; Yang, P.; Fleming, G. R. Room-Temperature Coherent Optical Phonon in 2D Electronic Spectra of $CH_3NH_3PbI_3$ Perovskite as a Possible Cooling Bottleneck. *J. Phys. Chem. Lett.* **2017**, *8*(14), 3211-3215.

(109) Esmaielpour, H.; Whiteside, V. R.; Piyathilaka, H. P.; Vijeyaragunathan, S.; Wang, B.; Adcock-Smith, E.; Roberts, K. P.; Mishima, T. D.; Santos, M. B.; Bristow, A. D.; Sellers, I. R. Enhanced hot electron lifetimes in quantum wells with inhibited phonon coupling. *Sci. Rep.* **2018**, *8*, 12473.

(110) Rosenwaks, Y.; Hanna, M. C.; Levi, D. H.; Szmyd, D. M.; Ahrenkiel, R. K.; Nozik, A. J. Hot-carrier cooling in GaAs: Quantum wells versus bulk. *Phys. Rev. B* **1993**, *48*(19), 14675-14678.

(111) Sondhauss, P.; Larsson, J.; Harbst, M.; Naylor, G. A.; Plech, A.; Scheidt, K.; Synnergren, O.; Wulff, M.; Wark, J. S. Picosecond X-Ray Studies of Coherent Folded Acoustic Phonons in a Multiple Quantum Well. *Phys. Rev. Lett.* **2005**, *94*(12), 125509.

(112) Özgür, Ü.; Lee, C.-W.; Everitt, H. O. Control of Coherent Acoustic Phonons. *Opt. Photonics News* **2001**, *12*(12), 66.

(113) Achermann, M.; Bartko, A. P.; Hollingsworth, J. A.; Klimov, V. I. The effect of Auger heating on intraband carrier relaxation in semiconductor quantum rods. *Nat. Phys.* **2006**, *2*, 557-561.

(114) Klimov, V. I.; McBranch, D. W. Femtosecond 1P-to-1S Electron Relaxation in Strongly Confined Semiconductor Nanocrystals. *Phys. Rev. Lett.* **1998**, *80*(18), 4028–4031.

(115) Anusca, I.; Balčiūnas, S.; Gemeiner, P.; Svirskas, Š.; Sanlialp, M.; Lackner, G.; Fettkenhauer, C.; Belovickis, J.; Samulionis, V.; Ivanov, M.; Dkhil, B.; Banys, J.; Shvartsman, V. V.; Lupascu, D. C. Dielectric Response: Answer to Many Questions in the Methylammonium Lead Halide Solar Cell Absorbers. *Adv. Energy Mater.* **2017**, *7*(19), 1700600.

(116) Miyata, K.; Meggiolaro, D.; Trinh, M. T.; Joshi, P. P.; Mosconi, E.; Jones, S. C.; De Angelis, F.; Zhu, X. Y. Large polarons in lead halide perovskites. *Sci. Adv.* **2017**, *3*(8), e1701217.

(117) Landau, L. D. The Movement of Electrons in the Crystal Lattice. *Phys. Z. Sowjetunion* **1933**, *3*, 644-645.

(118) Franchini, C.; Reticcioli, M.; Setvin, M.; Diebold, U. Polarons in materials. *Nat. Rev. Mater.* **2021**, *6*, 560-586.

(119) Emin, D., *Polarons*. Cambridge University Press: 2012.

(120) Zhu, X. Y.; Podzorov, V. Charge Carriers in Hybrid Organic-Inorganic Lead Halide Perovskites Might Be Protected as Large Polarons. *J. Phys. Chem. Lett.* **2015**, *6*(23), 4758-4761.

(121) Brivio, F.; Walker, A. B.; Walsh, A. Structural and electronic properties of hybrid perovskites for high-efficiency thin-film photovoltaics from first-principles. *APL Mater.* **2013**, *1*(4), 042111.

(122) Even, J.; Carignano, M.; Katan, C. Molecular disorder and translation/rotation coupling in the plastic crystal phase of hybrid perovskites. *Nanoscale* **2016**, *8*(12), 6222-6236.

(123) Ma, J.; Wang, L.-W. Nanoscale Charge Localization Induced by Random Orientations of Organic Molecules in Hybrid Perovskite $CH_3NH_3PbI_3$. *Nano Lett.* **2015**, *15*(1), 248-253.

(124) Berdiyorov, G. R.; Kachmar, A.; El-Mellouhi, F.; Carignano, M. A.; El-Amine Madjet, M. Role of Cations on the Electronic Transport and Optical Properties of Lead-Iodide Perovskites. *J. Phys. Chem. C* **2016**, *120*(30), 16259-16270.

(125) Zhu, H.; Trinh, M. T.; Wang, J.; Fu, Y.; Joshi, P. P.; Miyata, K.; Jin, S.; Zhu, X. Y. Organic Cations Might Not Be Essential to the Remarkable Properties of Band Edge Carriers in Lead Halide Perovskites. *Adv. Mater.* **2017**, *29*(1), 1603072.

(126) Cinquanta, E.; Meggiolaro, D.; Motti, S. G.; Gandini, M.; Alcocer, M. J. P.; Akkerman, Q. A.; Vozzi, C.; Manna, L.; De Angelis, F.; Petrozza, A.; Stagira, S. Ultrafast THz Probe of Photoinduced Polarons in Lead-Halide Perovskites. *Phys. Rev. Lett.* **2019**, *122*(16), 166601.

(127) Marronnier, A.; Lee, H.; Geffroy, B.; Even, J.; Bonnassieux, Y.; Roma, G. Structural Instabilities Related to Highly Anharmonic Phonons in Halide Perovskites. *J. Phys. Chem. Lett.* **2017**, *8*(12), 2659-2665.

(128) Katan, C.; Mohite, A. D.; Even, J. Entropy in halide perovskites. *Nat. Mater.* **2018**, *17*, 377-379.

(129) Létoublon, A.; Paofai, S.; Rufflé, B.; Bourges, P.; Hehlen, B.; Michel, T.; Ecolivet, C.; Durand, O.; Cordier, S.; Katan, C.; Even, J. Elastic Constants, Optical Phonons, and Molecular Relaxations in the High Temperature Plastic Phase of the $CH_3NH_3PbBr_3$ Hybrid Perovskite. *J. Phys. Chem. Lett.* **2016**, *7*(19), 3776-3784.

(130) Quarti, C.; Grancini, G.; Mosconi, E.; Bruno, P.; Ball, J. M.; Lee, M. M.; Snaith, H. J.; Petrozza, A.; Angelis, F. D. The Raman Spectrum of the $CH_3NH_3PbI_3$ Hybrid Perovskite: Interplay of Theory and Experiment. *J. Phys. Chem. Lett.* **2014**, *5*(2), 279-284.

(131) Munson, K. T.; Kennehan, E. R.; Doucette, G. S.; Asbury, J. B. Dynamic Disorder Dominates Delocalization, Transport, and Recombination in Halide Perovskites. *Chem* **2018**, *4*(12), 2826-2843.

(132) Kang, J.; Wang, L.-W. Dynamic Disorder and Potential Fluctuation in Two-Dimensional Perovskite. *J. Phys. Chem. Lett.* **2017**, *8*(16), 3875-3880.

(133) Ambrosio, F.; Wiktor, J.; De Angelis, F.; Pasquarello, A. Origin of low electron–hole recombination rate in metal halide perovskites. *Energy Environ. Sci.* **2018**, *11*(1), 101-105.

(134) Ma, J.; Wang, L.-W. The Nature of Electron Mobility in Hybrid Perovskite $CH_3NH_3PbI_3$. *Nano Lett.* **2017**, *17*(6), 3646-3654.

(135) Quarti, C.; Mosconi, E.; De Angelis, F. Structural and electronic properties of organo-halide hybrid perovskites from ab initio molecular dynamics. *Phys. Chem. Chem. Phys.* **2015**, *17*(14), 9394-9409.

(136) Carignano, M. A.; Kachmar, A.; Hutter, J. Thermal Effects on $CH_3NH_3PbI_3$ Perovskite from Ab Initio Molecular Dynamics Simulations. *J. Phys. Chem. C* **2015**, *119*(17), 8991-8997.

(137) Bakulin, A. A.; Selig, O.; Bakker, H. J.; Rezus, Y. L.; Muller, C.; Glaser, T.; Lovrincic, R.; Sun, Z.; Chen, Z.; Walsh, A.; Frost, J. M.; Jansen, T. L. Real-Time Observation of Organic Cation Reorientation in Methylammonium Lead Iodide Perovskites. *J. Phys. Chem. Lett.* **2015**, *6*(18), 3663-3669.

(138) Walsh, A. Principles of Chemical Bonding and Band Gap Engineering in Hybrid Organic–Inorganic Halide Perovskites. *J. Phys. Chem. C* **2015**, *119*(11), 5755-5760.

(139) Frost, J. M.; Whalley, L. D.; Walsh, A. Slow Cooling of Hot Polarons in Halide Perovskite Solar Cells. *ACS Energy Lett.* **2017**, *2*(12), 2647-2652.

(140) Price, M. B.; Butkus, J.; Jellicoe, T. C.; Sadhanala, A.; Briane, A.; Halpert, J. E.; Broch, K.; Hodgkiss, J. M.; Friend, R. H.; Deschler, F. Hot-carrier cooling and photoinduced refractive index changes in organic-inorganic lead halide perovskites. *Nat. Commun.* **2015**, *6*, 8420.

(141) Chen, K.; Barker, A. J.; Morgan, F. L.; Halpert, J. E.; Hodgkiss, J. M. Effect of Carrier Thermalization Dynamics on Light Emission and Amplification in Organometal Halide Perovskites. *J. Phys. Chem. Lett.* **2015**, *6*(1), 153-158.

(142) Chan, C. C. S.; Fan, K.; Wang, H.; Huang, Z.; Novko, D.; Yan, K.; Xu, J.; Choy, W. C. H.; Lončarić, I.; Wong, K. S. Uncovering the Electron‐Phonon Interplay and Dynamical Energy‐Dissipation Mechanisms of Hot Carriers in Hybrid Lead Halide Perovskites. *Adv. Energy Mater.* **2021**, *11*(9), 2003071.

(143) Berera, R.; Van Grondelle, R.; Kennis, J. T. M. Ultrafast transient absorption spectroscopy: principles and application to photosynthetic systems. *Photosynth. Res.* **2009**, *101*, 105-118.

(144) Kahn, A. Fermi level, work function and vacuum level. *Mater. Horiz.* **2016**, *3*, 7-10.

(145) Helander, M. G.; Greiner, M. T.; Wang, Z. B.; Lu, Z. H. Pitfalls in measuring work function using photoelectron spectroscopy. *Appl. Surf. Sci.* **2010**, *256*(8), 2602-2605.

(146) Li, Z.; Yang, M.; Park, J.-S.; Wei, S.-H.; Berry, J. J.; Zhu, K. Stabilizing Perovskite Structures by Tuning Tolerance Factor: Formation of Formamidinium and Cesium Lead Iodide Solid-State Alloys. *Chem. Mater.* **2016**, *28*(1), 284-292.

(147) Fu, Y.; Hautzinger, M. P.; Luo, Z.; Wang, F.; Pan, D.; Aristov, M. M.; Guzei, I. A.; Pan, A.; Zhu, X.; Jin, S. Incorporating Large A Cations into Lead Iodide Perovskite Cages: Relaxed Goldschmidt Tolerance Factor and Impact on Exciton–Phonon Interaction. *ACS Cent. Sci.* **2019**, *5*(8), 1377-1386.

(148) Zhu, Q.; Zheng, K.; Abdellah, M.; Generalov, A.; Haase, D.; Carlson, S.; Niu, Y.; Heimdal, J.; Engdahl, A.; Messing, M. E.; Pullerits, T.; Canton, S. E. Correlating structure and electronic band-edge properties in organolead halide perovskites nanoparticles. *Phys. Chem. Chem. Phys.* **2016**, *18*(22), 14933-14940.

(149) Payne, D. J.; Egdell, R. G.; Walsh, A.; Watson, G. W.; Guo, J.; Glans, P. A.; Learmonth, T.; Smith, K. E. Electronic Origins of Structural Distortions in Post-Transition Metal Oxides: Experimental and Theoretical Evidence for a Revision of the Lone Pair Model. *Phys. Rev. Lett.* **2006**, *96*(15), 157403.

(150) Waghmare, U. V.; Spaldin, N. A.; Kandpal, H. C.; Seshadri, R. First-principles indicators of metallicity and cation off-centricity in the IV-VI rocksalt chalcogenides of divalent Ge, Sn, and Pb. *Phys. Rev. B* **2003**, *67*(12), 125111.

(151) Stranks, S. D.; Burlakov, V. M.; Leijtens, T.; Ball, J. M.; Goriely, A.; Snaith, H. J. Recombination Kinetics in Organic-Inorganic Perovskites: Excitons, Free Charge, and Subgap States. *Phys. Rev. Appl.* **2014**, *2*(3), 034007.

(152) Zheng, K.; Žídek, K.; Abdellah, M.; Chen, J.; Chábera, P.; Zhang, W.; Al-Marri, M. J.; Pullerits, T. High Excitation Intensity Opens a New Trapping Channel in Organic–Inorganic Hybrid Perovskite Nanoparticles. *ACS Energy Lett.* **2016**, *1*(6), 1154-1161.

(153) Zheng, K.; Žídek, K.; Abdellah, M.; Messing, M. E.; Al-Marri, M. J.; Pullerits, T. Trap States and Their Dynamics in Organometal Halide Perovskite Nanoparticles and Bulk Crystals. *J. Phys. Chem. C* **2016**, *120*(5), 3077-3084.

(154) Chen, Y.; Sun, Y.; Peng, J.; Tang, J.; Zheng, K.; Liang, Z. 2D Ruddlesden-Popper Perovskites for Optoelectronics. *Adv. Mater.* **2018**, *30*(2), 1703487.

(155) Blancon, J. C.; Tsai, H.; Nie, W.; Stoumpos, C. C.; Pedesseau, L.; Katan, C.; Kepenekian, M.; Soe, C. M.; Appavoo, K.; Sfeir, M. Y.; Tretiak, S.; Ajayan, P. M.; Kanatzidis, M. G.; Even, J.; Crochet, J. J.; Mohite, A. D. Extremely efficient internal exciton dissociation through edge states in layered 2D perovskites. *Science* **2017**, *355*(6331), 1288-1292.

(156) Kahmann, S.; Tekelenburg, E. K.; Duim, H.; Kamminga, M. E.; Loi, M. A. Extrinsic nature of the broad photoluminescence in lead iodide-based Ruddlesden–Popper perovskites. *Nat. Commun.* **2020**, *11*, 2344.

(157) Kepenekian, M.; Traore, B.; Blancon, J. C.; Pedesseau, L.; Tsai, H.; Nie, W.; Stoumpos, C. C.; Kanatzidis, M. G.; Even, J.; Mohite, A. D.; Tretiak, S.; Katan, C. Concept of Lattice Mismatch and Emergence of Surface States in Two-dimensional Hybrid Perovskite Quantum Wells. *Nano Lett.* **2018**, *18*(9), 5603–5609.

(158) Wang, K.; Wu, C.; Jiang, Y.; Yang, D.; Wang, K.; Priya, S. Distinct conducting layer edge states intwo-dimensional (2D) halide perovskite. *Sci. Adv.* **2019**, *5*(7), eaau3241.

(159) Li, S.; Luo, J.; Liu, J.; Tang, J. Self-Trapped Excitons in All-Inorganic Halide Perovskites: Fundamentals, Status, and Potential Applications. *J. Phys. Chem. Lett.* **2019**, *10*(8), 1999-2007.

(160) Blancon, J. C.; Stier, A. V.; Tsai, H.; Nie, W.; Stoumpos, C. C.; Traore, B.; Pedesseau, L.; Kepenekian, M.; Katsutani, F.; Noe, G. T.; Kono, J.; Tretiak, S.; Crooker, S. A.; Katan, C.; Kanatzidis, M. G.; Crochet, J. J.; Even, J.; Mohite, A. D. Scaling law for excitons in 2D perovskite quantum wells. *Nat. Commun.* **2018**, *9*, 2254.

(161) Jaffe, A.; Lin, Y.; Beavers, C. M.; Voss, J.; Mao, W. L.; Karunadasa, H. I. High-Pressure Single-Crystal Structures of 3D Lead-Halide Hybrid Perovskites and Pressure Effects on their Electronic and Optical Properties. *ACS Cent. Sci.* **2016**, *2*(4), 201-209.

(162) Silva, G. G.; Da Cunha, W. F.; De Sousa Junior, R. T.; Almeida Fonseca, A. L.; Ribeiro Júnior, L. A.; E Silva, G. M. Influence of quasi-particle density over polaron mobility in armchair graphene nanoribbons. *Phys. Chem. Chem. Phys.* **2018**, *20*(24), 16712-16718.

(163) Seitz, M.; Magdaleno, A. J.; Alcazar-Cano, N.; Melendez, M.; Lubbers, T. J.; Walraven, S. W.; Pakdel, S.; Prada, E.; Delgado-Buscalioni, R.; Prins, F. Exciton diffusion in two-dimensional metal-halide perovskites. *Nat. Commun.* **2020**, *11*, 2035.

(164) Coehoorn, R.; Zhang, L.; Bobbert, P. A.; Van Eersel, H. Effect of polaron diffusion on exciton-polaron quenching in disordered organic semiconductors. *Phys. Rev. B* **2017**, *95*(13), 134202.

(165) Mao, L.; Stoumpos, C. C.; Kanatzidis, M. G. Two-Dimensional Hybrid Halide Perovskites: Principles and Promises. *J. Am. Chem. Soc.* **2019**, *141*(3), 1171-1190.

(166) Zhang, Z.; Fang, W.-H.; Long, R.; Prezhdo, O. V. Exciton Dissociation and Suppressed Charge Recombination at 2D Perovskite Edges: Key Roles of Unsaturated Halide Bonds and Thermal Disorder. *J. Am. Chem. Soc.* **2019**, *141*(39), 15557-15566.

(167) Bao, J.; Hadjiev, V. G. Origin of Luminescent Centers and Edge States in Low-Dimensional Lead Halide Perovskites: Controversies, Challenges and Instructive Approaches. *Nano-Micro Lett.* **2019**, *11*, 26.

(168) Shi, E.; Deng, S.; Yuan, B.; Gao, Y.; Akriti; Yuan, L.; Davis, C. S.; Zemlyanov, D.; Yu, Y.; Huang, L.; Dou, L. Extrinsic and Dynamic Edge States of Two-Dimensional Lead Halide Perovskites. *ACS Nano* **2019**, *13*(2), 1635-1644.

(169) Zhao, C.; Tian, W.; Sun, Q.; Yin, Z.; Leng, J.; Wang, S.; Liu, J.; Wu, K.; Jin, S. Trap-Enabled Long-Distance Carrier Transport in Perovskite Quantum Wells. *J. Am. Chem. Soc.* **2020**, *142*(35), 15091-15097.

(170) Cao, D. H.; Stoumpos, C. C.; Farha, O. K.; Hupp, J. T.; Kanatzidis, M. G. 2D Homologous Perovskites as Light-Absorbing Materials for Solar Cell Applications. *J. Am. Chem. Soc.* **2015**, *137*(24), 7843-7850.

(171) Guo, P.; Stoumpos, C. C.; Mao, L.; Sadasivam, S.; Ketterson, J. B.; Darancet, P.; Kanatzidis, M. G.; Schaller, R. D. Cross-plane coherent acoustic phonons in two-dimensional organic-inorganic hybrid perovskites. *Nat. Commun.* **2018**, *9*, 2019.

(172) Lim, J. W. M.; Giovanni, D.; Righetto, M.; Feng, M.; Mhaisalkar, S. G.; Mathews, N.; Sum, T. C. Hot Carriers in Halide Perovskites: How Hot Truly? *J. Phys. Chem. Lett.* **2020**, *11*(7), 2743-2750.

(173) Chen, J.; Messing, M. E.; Zheng, K.; Pullerits, T. Cation-Dependent Hot Carrier Cooling in Halide Perovskite Nanocrystals. *J. Am. Chem. Soc.* **2019**, *141*(8), 3532-3540.

(174) Seah, M. P.; Dench, W. A. Quantitative electron spectroscopy of surfaces: A standard data base for electron inelastic mean free paths in solids. *Surf. Interface Anal.* **1979**, *1*(1), 2-11.

(175) Shao, Y.; Gao, W.; Yan, H.; Li, R.; Abdelwahab, I.; Chi, X.; Rogée, L.; Zhuang, L.; Fu, W.; Lau, S. P.; Yu, S. F.; Cai, Y.; Loh, K. P.; Leng, K. Unlocking surface octahedral tilt in two-dimensional Ruddlesden-Popper perovskites. *Nat. Commun.* **2022**, *13*, 138.

(176) Liang, M.; Lin, W.; Zhao, Q.; Zou, X.; Lan, Z.; Meng, J.; Shi, Q.; Castelli, I. E.; Canton, S. E.; Pullerits, T.; Zheng, K. Free Carriers versus Self-Trapped Excitons at Different Facets of Ruddlesden–Popper Two-Dimensional Lead Halide Perovskite Single Crystals. *J. Phys. Chem. Lett.* **2021**, *12*(20), 4965-4971.

(177) Duan, H. G.; Tiwari, V.; Jha, A.; Berdiyorov, G. R.; Akimov, A.; Vendrell, O.; Nayak, P. K.; Snaith, H. J.; Thorwart, M.; Li, Z.; Madjet, M. E.; Miller, R. J. D. Photoinduced Vibrations Drive Ultrafast Structural Distortion in Lead Halide Perovskite. *J. Am. Chem. Soc.* **2020**, *142*(39), 16569-16578.

(178) Zhang, Z.; Fang, W. H.; Tokina, M. V.; Long, R.; Prezhdo, O. V. Rapid Decoherence Suppresses Charge Recombination in Multi-Layer 2D Halide Perovskites: Time-Domain Ab Initio Analysis. *Nano Lett.* **2018**, *18*(4), 2459-2466.

(179) Zhang, Y.; Wang, R.; Li, Y.; Wang, Z.; Hu, S.; Yan, X.; Zhai, Y.; Zhang, C.; Sheng, C. Optical Properties of Two-Dimensional Perovskite Films of $(C_6H_5C_2H_4NH_3)_2[PbI_4]$ and $(C_6H_5C_2H_4NH_3)_2$ $(CH_3NH_3)_2[Pb_3I_{10}]$. *J. Phys. Chem. Lett.* **2019**, *10*(1), 13-19.

(180) Sarma, S. D.; Jain, J. K.; Jalabert, R. Many-body theory of energy relaxation in an excited-electron gas via optical-phonon emission. *Phys. Rev. B* **1990**, *41*(6), 3561-3571.

(181) Fang, H.-H.; Adjokatse, S.; Shao, S.; Even, J.; Loi, M. A. Long-lived hot-carrier light emission and large blue shift in formamidinium tin triiodide perovskites. *Nat. Commun.* **2018**, *9*, 243.

(182) Zhou, Y.; Chen, J.; Bakr, O. M.; Sun, H.-T. Metal-Doped Lead Halide Perovskites: Synthesis, Properties, and Optoelectronic Applications. *Chem. Mater.* **2018**, *30*(19), 6589-6613.

(183) Liu, W.; Lin, Q.; Li, H.; Wu, K.; Robel, I.; Pietryga, J. M.; Klimov, V. I. Mn^{2+}-Doped Lead Halide Perovskite Nanocrystals with Dual-Color Emission Controlled by Halide Content. *J. Am. Chem. Soc.* **2016**, *138*(45), 14954-14961.

(184) Akkerman, Q. A.; Meggiolaro, D.; Dang, Z.; De Angelis, F.; Manna, L. Fluorescent Alloy $CsPb_xMn_{1-x}I_3$ Perovskite Nanocrystals with High Structural and Optical Stability. *ACS Energy Lett.* **2017**, *2*(9), 2183-2186.

(185) Guria, A. K.; Dutta, S. K.; Adhikari, S. D.; Pradhan, N. Doping Mn^{2+} in Lead Halide Perovskite Nanocrystals: Successes and Challenges. *ACS Energy Lett.* **2017**, *2*(5), 1014-1021.

(186) Ji, S.; Yuan, X.; Cao, S.; Ji, W.; Zhang, H.; Wang, Y.; Li, H.; Zhao, J.; Zou, B. Near-Unity Red Mn^{2+} Photoluminescence Quantum Yield of Doped $CsPbCl_3$ Nanocrystals with Cd Incorporation. *J. Phys. Chem. Lett.* **2020**, *11*(6), 2142-2149.

(187) Kahmann, S.; Loi, M. A. Hot carrier solar cells and the potential of perovskites for breaking the Shockley–Queisser limit. *J. Mater. Chem. C* **2019**, *7*(9), 2471-2486.

(188) Shafique, A.; Shin, Y.-H. Strain engineering of phonon thermal transport properties in monolayer 2H-$MoTe_2$. *Phys. Chem. Chem. Phys.* **2017**, *19*(47), 32072-32078.

Printed by Media-Tryck, Lund 2022 NORDIC SWAN ECOLABEL 3041 0903

Faculty of Science
Department of Chemistry
Division of Chemical Physics

ISBN 978-91-7422-916-5